A Search for the Process $b \longrightarrow s + \gamma$

by

T. Lesiak

A Search for the Process $b \to s + \gamma$

Tadeusz Lesiak

Institute of Nuclear Physics

Cracow

Ubi amatur, non laboratur
Et si laboratur, labor amatur

Summ. Theol.
St. Thomas from Akwina

To my wife

Abstract

We have searched for the rare flavour changing neutral current decay $b \to s\gamma$ in the multi-hadron data sample taken at the $\Upsilon(4S)$ resonance with the help of the Crystal Ball detector at the e^+e^- storage ring DORIS II. The non-observation of any monochromatic photon line in the inclusive photon spectrum resulted in the estimation of the following upper limit of the branching fraction for the process under investigation

$$BR(b \to s\gamma) < 4.1 \times 10^{-3}$$

(at 90% confidence level), as well as for some of the related exclusive decays:

$$
\begin{array}{lcl}
BR(B \to K^*(892)\gamma) & < & 1.8 \times 10^{-3} \\
BR(B \to K_1(1400)\gamma) & < & 1.3 \times 10^{-3} \\
BR(B \to K_2(1770)\gamma) & < & 0.9 \times 10^{-3} \\
BR(B \to K_4^*(2075)\gamma) & < & 0.9 \times 10^{-3}.
\end{array}
$$

The decays $B \to KJ/\psi$ and $B \to K^*J/\psi$ have also been searched for. No enhancement was found in the spectrum of the missing mass with respect to the electron pair in the final state coming from the decay $J/\psi \to e^+e^-$. The following upper limits have been determined:

$$
\begin{array}{lcl}
BR(B \to KJ/\psi) & < & 0.6 \times 10^{-2} \\
BR(B \to K^*(892)J/\psi) & < & 0.8 \times 10^{-2} \\
BR(B \to K_1(1400)J/\psi) & < & 1.5 \times 10^{-2} \\
BR(B \to K_3^*(1780)J/\psi) & < & 1.9 \times 10^{-2}.
\end{array}
$$

In order to test predictions of the Standard Model versions together with higher order QCD corrections or to get evidence for new physics beyond it a substantial improvement of the constraint for the branching fraction for the decay $b \to s\gamma$ (up to one order of magnitude) is necessary.

1

Streszczenie

Poszukiwano rzadkiego procesu prądu neutralnego ze zmianą dziwności $b \rightarrow s\gamma$ przy pomocy detektora Crystal Ball pracującego na elektronowo-pozytonowym akceleratorze wiązek przeciwbieżnych DORIS II w próbce danych zawierającej wielohadronowe przypadki zebrane w maksimum rezonansu $\Upsilon(4S)$. Nie zaobserwowano żadnej monochromatycznej linii fotonowej dla zmierzonego inkluzywnego widma fotonów. Wyznaczono górną granicę na częstość rozpadu dla procesu:

$$BR(b \rightarrow s\gamma) < 4.1 \times 10^{-3}$$

(przy poziomie ufności 90%) jak również dla niektórych odpowiadających mu rozpadów ekskluzywnych:

$BR(B \rightarrow K^*(892)\gamma)$	$<$	1.8×10^{-3}
$BR(B \rightarrow K_1(1400)\gamma)$	$<$	1.3×10^{-3}
$BR(B \rightarrow K_2(1770)\gamma)$	$<$	0.9×10^{-3}
$BR(B \rightarrow K_4^*(2075)\gamma)$	$<$	$0.9 \times 10^{-3}.$

Poszukiwano również rozpadów $B \rightarrow KJ/\psi$ i $B \rightarrow K^*J/\psi$. Nie wykryto żadnego maksimum w badanym widmie masy brakującej względem pary elektronowej w stanie końcowym pochodzącej z rozpadu $J/\psi \rightarrow e^+e^-$. W rezultacie zmierzono górne granice na następujące częstości rozpadów:

$BR(B \rightarrow KJ/\psi)$	$<$	0.6×10^{-2}
$BR(B \rightarrow K^*(892)J/\psi)$	$<$	0.8×10^{-2}
$BR(B \rightarrow K_1(1400)J/\psi)$	$<$	1.5×10^{-2}
$BR(B \rightarrow K_3^*(1780)J/\psi)$	$<$	$1.9 \times 10^{-2}.$

Do sprawdzenia przewidywań Modelu Standardowego wraz z poprawkami wyższych rzędów pochodzącymi od oddziaływań silnych oraz do zbadania słuszności teorii stanowiących jego rozszerzenie konieczne jest znaczne (przynajmniej o rząd wielkości) obniżenie górnej granicy stosunku rozgałęzienia dla procesu $b \rightarrow s\gamma$.

Contents

1. Introduction

High energy physics investigates the fundamental structure of matter. The basic question is what are the ultimate building blocks of matter and what forces act between them. At the present state of knowledge, elementary particles and their interactions are described by the theory called the Standard Model. The estimation of upper limits of branching fractions of some rare processes like the flavour changing neutral current $b \to s\gamma$ expected in this model with a branching fraction of about 10^{-4} would offer the possibility of testing the estimates for the free parameters of the Standard Model. Alternatively it could indicate the presence of new particles predicted by the extensions of the Standard Model. We mean here theories with left-right symmetry [1], with two Higgs boson doublets [2] or so-called supersymmetric theories [3].

The author has performed the analysis of multi-hadron events at the $\Upsilon(4S)$ resonance collected in 1985–1986 with the Crystal Ball detector working at the e^+e^- storage ring DORIS II. It was aimed at the search for the process $b \to s\gamma$. As a result the upper limit on the branching fraction of the decay $b \to s\gamma$ and for exclusive decays $B \to K^*\gamma$, $B \to KJ/\psi$ and $B \to K^*J/\psi$ have been determined.

This thesis was prepared in 1988–1991 in the Deutsches Elektronen Synchroton in Hamburg (Germany) and in the Cracow Institute of Nuclear Physics (Poland). The thesis is organized as follows:

In Chapter 2 we describe the present state of theoretical knowledge concerning the flavour changing neutral current $b \to s\gamma$ and the decays $B \to KJ/\psi$ and $B \to K^*J/\psi$.

Chapter 3 is devoted to the description of the experimental setup i.e. to the e^+e^- storage ring DORIS II and to the calorimetric detector Crystal Ball.

The topic of the Chapter 4 is the data processing. We describe the data sample, the reconstruction procedure which transforms signals from the detector into energies and directions of detected particles. We also explain the selection criteria applied to choose multi-hadron events.

In Chapter 5 we discuss the selection of high energy photons and electron pairs from the J/ψ decay in order to search for the $b \to s\gamma$ process and the exclusive decays $B \to K^*\gamma$, $B \to KJ/\psi$ and $B \to K^*J/\psi$. Then the method of the efficiency calculation, the fitting procedure and the resulting upper limits for the relevant branching fractions are presented.

Chapter 6 contains the conclusions and comparison with the results of other experiments.

Topics discussed in the appendices include: measurement of luminosity and of energies of particles, identification of photons and electrons and description of the Monte Carlo techniques applied in the experiment.

A publication based on these results have been submitted to publication [4].

2.   Basic concepts

Matter is built from fermions (leptons and quarks), i.e. particles with spin 1/2 which are listed in Table 2.1. At the present state of knowledge we treat all of them as 'elementary', i.e. without any internal structure. They are grouped in three families called generations, however the origin of this structure is not yet clear.

Four kinds of interactions between particles are known: strong, electromagnetic, weak and gravitational. The last one has significant strength only in case of interaction of macroscopic bodies and will not be discussed here. The remaining interactions between fermions are mediated by vector bosons.

Quarks can take part in the strong, electromagnetic and weak interaction, charged leptons participate in the electromagnetic and weak interaction while neutral leptons (the neutrinos) interact only weakly. Each lepton carries its lepton generation quantum number. Each quark appears in three different states labelled by the colour quantum number.

Quarks have not been observed as free particles. The observable states (hadrons) are built as colour neutral bound states of three quarks (baryons) or of quark and antiquark (mesons) with integral charge.

2.1   Physics of the b quark

Among the large variety of particles observed in experiment we describe briefly some properties of mesons containing the b quark, namely the Υ and B states. This is because we search for radiative transition between the quarks b and s. This transition might be observed at the hadronic level as some rare decays of the B meson (built from a heavy b quark and a light antiquark $\bar{u}$ or $\bar{d}$) e.g., $B \to K^*\gamma$. In our study B mesons are produced in pairs in the decay of the $\Upsilon(4S)$ resonance created via electron-positron annihilation. Υ mesons formed as $b\bar{b}$ pairs belong to a family of resonances similar to positronium. The hadronic cross-section in the energy region of Υ states measured by the CLEO [5] collaboration at the CESR e^+e^- storage ring at Cornell is shown in Fig. 2.1. As it is seen there, the $\Upsilon(4S)$ resonance is much wider than the lower mass states $\Upsilon(1S)$, $\Upsilon(2S)$ and $\Upsilon(3S)$. This is because the lower states can decay into hadrons only via emission of three gluons (bosons mediating strong interactions). These

Table 2.1: Fundamental fermions and their electric charges.

Type	Generation			Electric
	1	2	3	charge
Leptons	ν_e	ν_μ	ν_τ	0
	e	μ	τ	-1
Quarks	u	c	t?	2/3
	d	s	b	-1/3

6

Hadronic cross section in nb
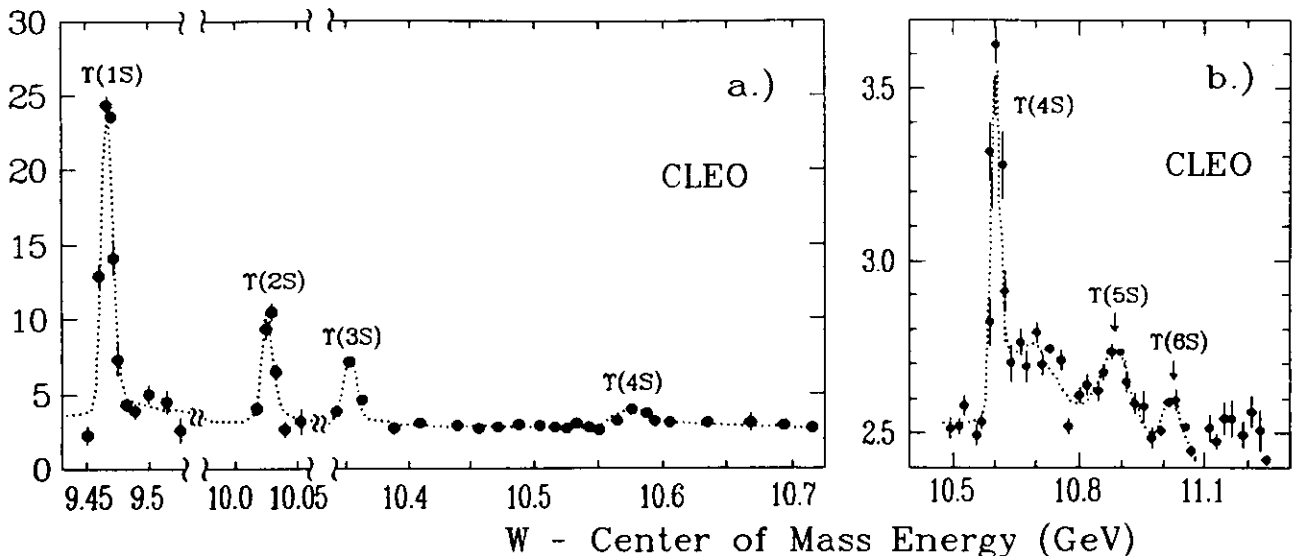
Figure 2.1: Hadronic cross-section in the energy region of the Υ family (measured by the CLEO collaboration at CESR [5]). Watch the scale difference between a) and b).

processes are suppressed by the OZI–rule [6] introduced by S. Okubo, G. Zweig and J. Izuka. The mass of the $\Upsilon(4S)$ is over two times as large as the mass of the B meson. Therefore the $\Upsilon(4S)$ can easily decay into hadrons via $B\bar{B}$ pairs.

The B meson decays are well described by the spectator model as weak decays of a free b quark (see Ref. [7]). This picture results e.g. in the prediction of the equal lifetimes for $B^{\pm}$ and B° mesons, which was recently confirmed experimentally by the ARGUS and CLEO collaborations [8]. Averaging the results of both experiments one obtains $\tau_{B^+}/\tau_{B^{\circ}} = 1.03 \pm 0.19$. The extensions of this model take into account binding effects of the b quark inside the B meson coming from strong interaction between quarks. The contribution from strong interaction is usually factorized into two parts: short-distance one (from emission of hard gluons with large square of the momentum transfer Q^2) and long-distance one (from soft gluon emission and final state interactions). The short-distance part is just a correction to the effective hamiltonian of the weak interaction. The long-distance contribution is taken into account in the model dependent wave functions of the initial and final state in this decay (see Ref. [9]).

2.2 Flavour changing neutral current $b \to s\gamma$

By Flavour Changing Neutral Currents (FCNC) we understand weak decays in which the initial quark transforms into another quark with the same charge. FCNC's have played an important role in the formulation of the Standard Model (SM). It was due to their non-observation in the kaon decay that the GIM mechanism [10] was introduced by S. Glashow, J. Iliopoulos and L. Maiani. This mechanism leads to the cancellation of contributions of the same order in the coupling constant and to the prediction of the fourth (charmed) quark. It also shed some light on the understanding of the $\Delta I = 1/2$ selection rule (see Ref. [11]) and of the CP violation effects (see Ref. [12]) especially in the $K \to \pi\pi$ decays. FCNC have also allowed to constrain and sometimes to rule out certain extensions of the Standard Model. The $b \to s$ FCNC transition is believed to be even more interesting as a source of information about the
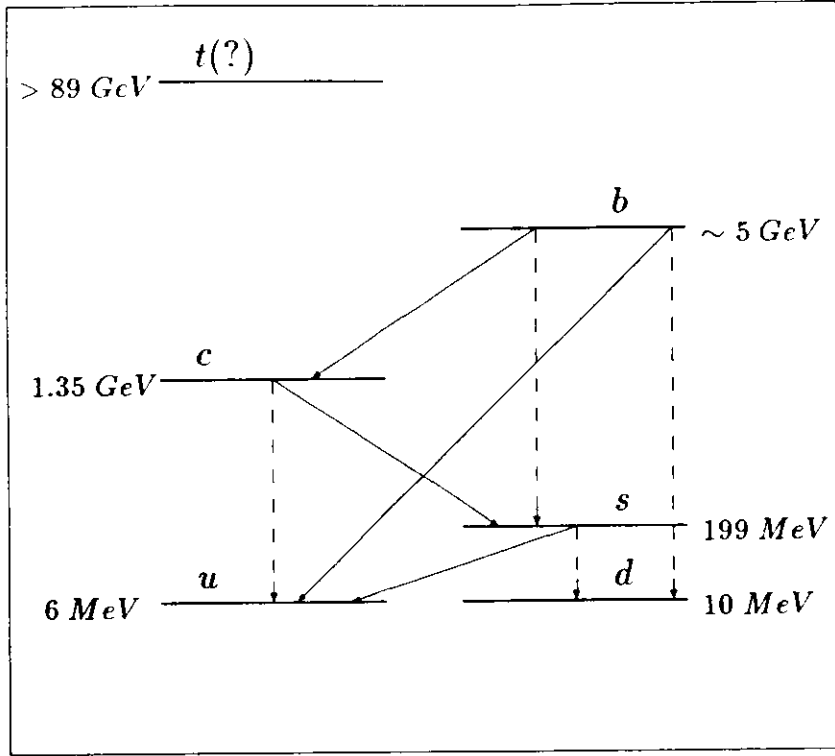
Figure 2.2: FCNC (dashed lines) and the charged current transitions (solid lines).

Standard Model constraints and about extensions. Now we will present some arguments that the decay $b \to s\gamma$ is probably the most promising FCNC starting from reminding the quark mixing.

In the Standard Model the quark mass eigenstates (denoted as q) are not the same as the weak interaction eigenstates q'. The matrix coupling two sets of eigenstates in the six quark case is known as the Kobayashi-Maskawa (K-M) mixing matrix V_{KM} [13]. By convention it is only the $-1/3$ charge quarks (d, s and b) which are mixed:

$$
\begin{pmatrix} d' \\ s' \\ b' \end{pmatrix} = \begin{pmatrix} V_{ud} & V_{us} & V_{ub} \\ V_{cd} & V_{cs} & V_{cb} \\ V_{td} & V_{ts} & V_{tb} \end{pmatrix} \begin{pmatrix} d \\ s \\ b \end{pmatrix}.
$$

The K-M matrix is unitary and depends on four parameters. There exist several parametrizations of this matrix. Using the Wolfenstein parametrization [14] one obtains:

$$
V_{KM} = \begin{pmatrix} 1 - \frac{\lambda^2}{2} & \lambda & A\lambda^3 \rho e^{i\phi} \\ -\lambda & 1 - \frac{\lambda^2}{2} & A\lambda^2 \\ A\lambda^3(1 - \rho e^{-i\phi}) & -A\lambda^2 & 1 \end{pmatrix} \cong \begin{pmatrix} 1 & \lambda & 0.1\lambda^2 \\ -\lambda & 1 & \lambda^2 \\ 0.1\lambda^2 & -\lambda^2 & 1 \end{pmatrix}
$$

Here $\lambda = 0.221 \pm 0.002$ and $A = 1.05 \pm 0.17$. The ρ and ϕ parameters are not yet well determined ($0.3 < \rho < 0.9$ and $\frac{2}{3}\pi < \phi < \pi$). In our rough approximation we used the recent CLEO and ARGUS results [15] namely that $|V_{ub}/V_{cb}| = 0.1^{+0.036}_{-0.016} < \lambda$ (i.e. $|V_{ub}| = |V_{td}| = 0.1\lambda^2 < \lambda^3$). In Fig. 2.2 we present the quark spectrum with FCNC transitions denoted as dashed lines and the charged current transitions as solid lines (constituent quark masses are also given from Ref. [16]).

Branching fraction
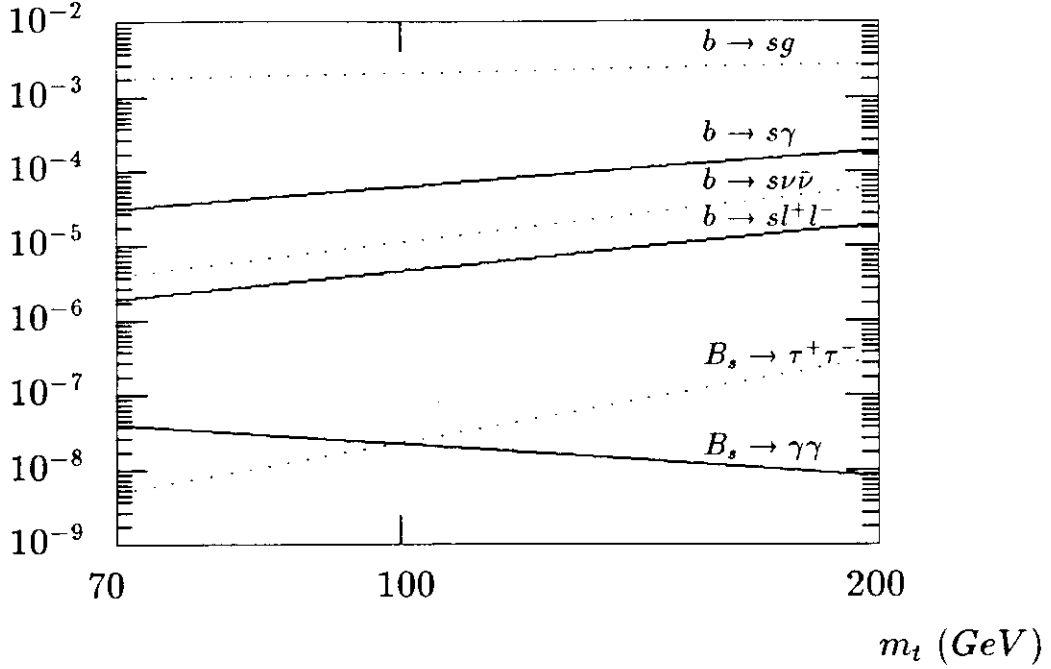
Figure 2.3: The Standard Model predictions (without taking into account QCD radiative corrections) for branching fractions on processes $b \to s(g, \gamma, \nu\bar{\nu}, l^+l^-)$ and on $B_s^0 \to (\gamma\gamma, \tau^+\tau^-)$ as a function of the top quark mass m_t (from Ref. [17]).

The FCNC decays of s and b are expected to be stronger than those of the c quark since in case of the charged current transitions between quarks q_1 and q_2, its amplitude is proportional to the K–M matrix element $V_{q_1 q_2}$ while the FCNC transitions are proportional to the product $V_{q_1 q_3} V_{q_2 q_3}^*$, where q_3 is the lowest mass quark heavier than q_1. Comparing the amplitudes of the respective transitions we obtain:

$$(s \to u) \propto \quad | V_{us} | \quad \cong \lambda$$
$$(s \to d) \propto \quad | V_{cs} V_{cd}^* | \quad \cong \lambda \tag{2.1}$$

$$(c \to s) \propto \quad | V_{cs} | \quad \cong 1$$
$$(c \to u) \propto \quad | V_{cb} V_{ub}^* | \quad \cong 0.1\lambda^4 \tag{2.2}$$

$$(b \to c) \propto \quad | V_{cb} | \quad \cong \lambda^2$$
$$(b \to s) \propto \quad | V_{tb} V_{ts}^* | \quad \cong \lambda^2 \tag{2.3}$$

$$(b \to u) \propto \quad | V_{ub} | \quad \cong 0.1\lambda^2$$
$$(b \to d) \propto \quad | V_{tb} V_{td}^* | \quad \cong 0.1\lambda^2 \tag{2.4}$$

so the FCNC decays of the b and s quarks (i.e. $s \to d$, $b \to s$ and $b \to d$) may be of the same strength as charged current decays ($s \to u$, $b \to c$ and $b \to u$), while the $c \to u$ decay is expected to be very weak. The decays of the b quark are favoured with respect to those of the s quark

9
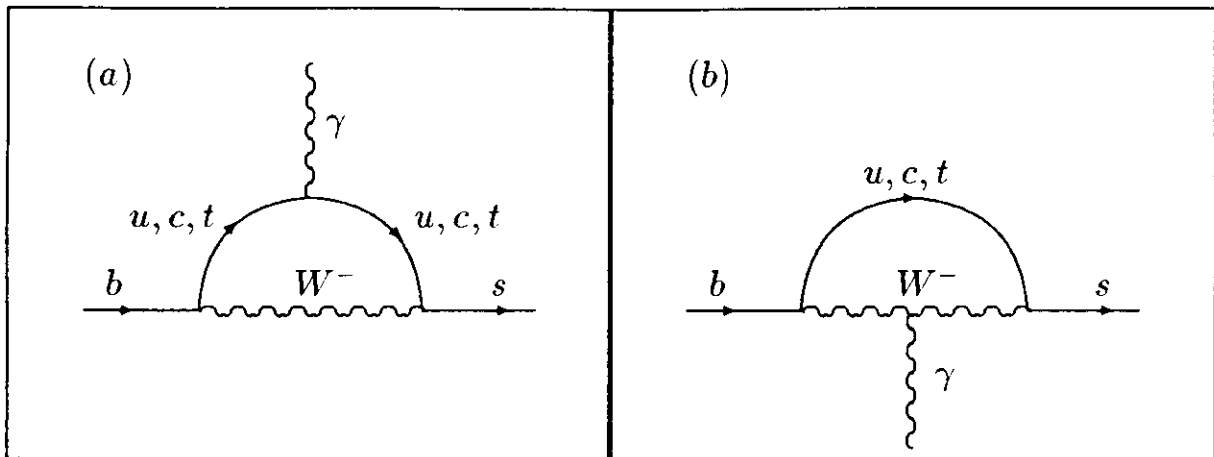
Figure 2.4: Penguin diagrams for the $b \to s\gamma$ transition in the Standard Model.

since it is expected [18] that the long-distance effects vanish at the decay of the heavy quark b. This was confirmed e.g. by the CLEO collaboration [19]. Their measurement of the upper limits for the representative group of the rare exclusive B meson decays via penguin diagrams excluded the presence of any significant enhancements of these processes by the long-distance interactions. On the other side it was shown by K. Gaillard, X.Q. Li and S. Rudaz [20] that the experimental knowledge about the decays of hyperons (the $s \to d$ transition) like e.g. on the ratio $\frac{\Gamma(\Xi^- \to \Sigma^- \gamma)}{\Gamma(\Sigma^+ \to p\gamma)}$ (see Ref. [21]) cannot be explained without taking into account a substantial contribution from non-perturbative long-distance interactions. In addition we expect that the ratio of the $b \to d$ to the $b \to s$ is proportional to $| V_{tb}V_{td}^* | / | V_{tb}V_{ts}^* |= \frac{0.1\lambda^2}{\lambda^2} \cong 0.1$, so the transition $b \to d$ is much weaker than the FCNC $b \to s$. Hereafter we concentrate on the decay $b \to sX$ where X denotes a flavourless (in particular charmless) system of particles. The following transitions have been studied theoretically [17]:

$$b \to sg \tag{2.5}$$

$$b \to s\gamma \tag{2.6}$$

$$b \to s\nu\bar{\nu} \tag{2.7}$$

$$b \to sl^+l^- \tag{2.8}$$

$$b\bar{s} \to \gamma\gamma \tag{2.9}$$

$$b\bar{s} \to \tau^+\tau^-. \tag{2.10}$$

They have been considered in the Standard Model and its extensions like left-right symmetric theories [1], models with two Higgs doublets [2] and also in supersymmetric (SUSY) schemes [3]. Now we will discuss some predictions of these models. We restrict themselves only to the transition $b \to s\gamma$ which has relatively high rate (Fig. 2.3) and clean signature of a high-energy monochromatic photon line. This is the transition we are going to search experimentally for.

2.2.1 The $b \to s\gamma$ transition in the Standard Model

In the Standard Model the decay $b \to s\gamma$ can occur only at the one-loop level via the so-called penguin diagrams (e.g., see Fig. 2.4 and Refs. [22] and [23]). Computing the amplitude
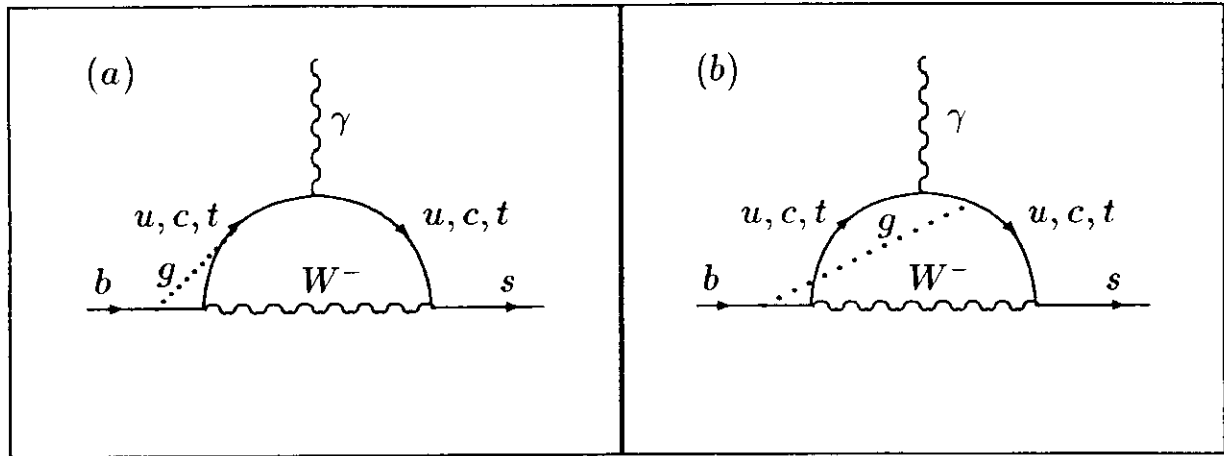
Figure 2.5: Diagrams of the first order QCD radiative corrections for the process $b \to s\gamma$.
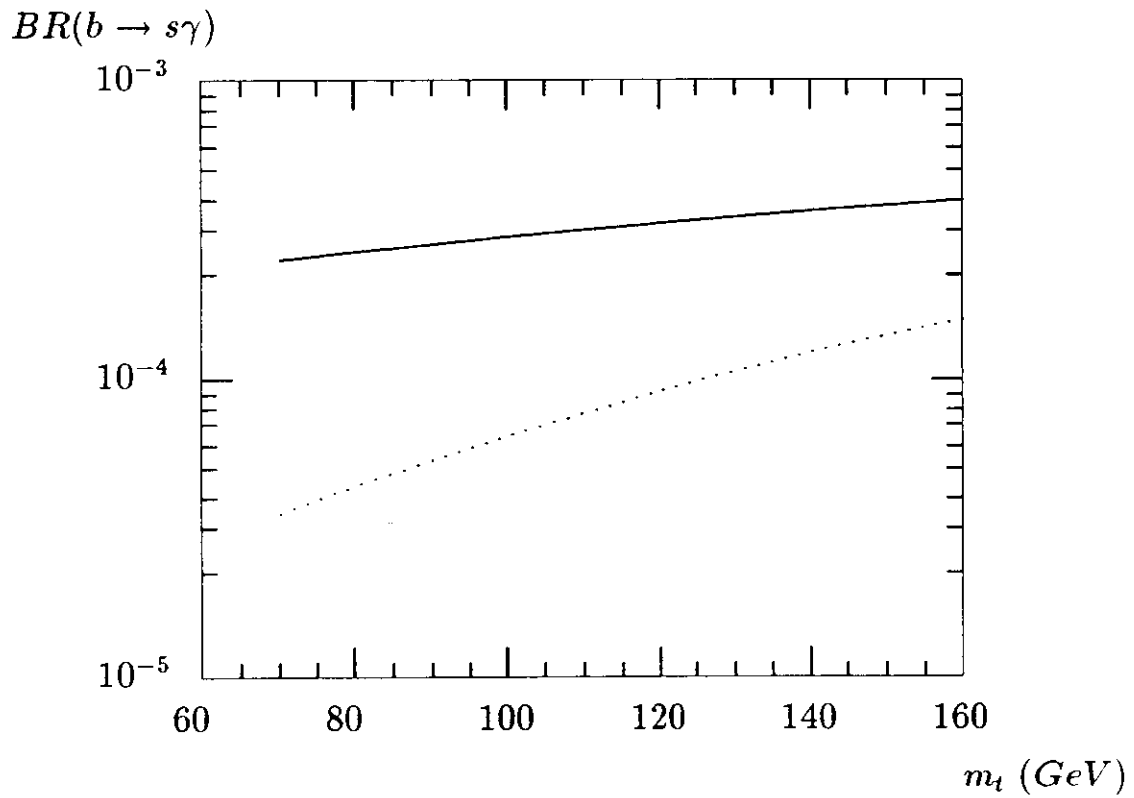
Figure 2.6: The Standard Model prediction for the $b \to s\gamma$ branching fraction (from [24]) with (solid line) and without (dashed line) QCD corrections as a function of the top quark mass m_t.

for diagrams from Fig. 2.4 yields the formula (from Ref. [24]):

$$A(b \to s\gamma)_{SM} = A_0 \, F(x_t) \, O_\gamma, \qquad (2.11)$$

where $A_0 = \sqrt{2}G_F V_{ts}^* V_{tb}$ (G_F is Fermi constant), $O_\gamma = (e/16\pi^2)m_b \bar{s}_L \sigma^{\mu\nu} b_R F_{\mu\nu}$ ($F_{\mu\nu}$ is the operator of the electromagnetic field strength, $\sigma_{\mu\nu} = (i/2)(\gamma_\mu\gamma_\nu - \gamma_\nu\gamma_\mu)$ and γ_μ are Dirac matrices), $x_t = m_t^2/m_W^2$ and the function $F(x_t)$ was determined by I. Inami and C.S. Lim [23]. For the one-loop amplitude the GIM mechanism manifests itself in the cancellation of large $\log(m_t^2/m_c^2)$ terms.

Calculation of the QCD radiative corrections to the process $b \to s\gamma$ when gluons are exchanged between internal and external fermion lines was performed in the leading-logarithm approximation by several authors ([25]-[28]). Some diagrams of the first order in the coupling constant of strong interaction α_s are shown in Fig. 2.5. Other diagrams are similar but with the gluon attached to the final s quark instead to the initial b quark. The amplitude is of the form

$$A(b \to s\gamma)_{SM+QCD\ corr.} = \eta^{-16/23} A_0 \left\{ F(x_t) + X \left[\frac{3}{10}(\eta^{10/23} - 1) + \frac{3}{28}(\eta^{28/23} - 1) \right] \right\} O_\gamma, \qquad (2.12)$$

where $\eta = \alpha_s(m_b)/\alpha_s(m_W)$ and $X = (4/3)[3Q_u - (4/9)Q_d]$ (Q_u and Q_d are the electric charges of the up and down quarks, respectively). In this formula the mass of the top quark is not present explicitly as the calculation was performed under the assumption that $m_t = m_W$. We expect however that this prediction is valid with an accuracy of 10% for $m_W/2 < m_t < 2m_W$, because of the weak energy dependence of the strong coupling constant in this range [24]. It was also shown (in Refs. [25, 26]) that the summation of leading logarithmic terms is already well approximated by the term $\propto \alpha_s$ giving $(\alpha_s/\pi)\log\frac{m_t}{m_b}$. For any value of m_t from the range $m_W/2 < m_t < 2m_W$ this logarithmic term is about one order of magnitude bigger than the factor $F(x_t)$. As a result radiative corrections (Fig. 2.5) yield an enhancement by a factor of 6 at $m_t = 100$ GeV and only of 3 at $m_t = 160$ GeV (see Fig. 2.6). Let us remind that the present estimates for the top quark mass are $m_t = (135^{+27+7}_{-31-8})$ GeV [29] where the second error reflects the uncertainty in the charm quark mass. Thus the QCD radiative corrections raise $BR(b \to s\gamma)$ to about 3×10^{-4}.

Using the linear approximation we parametrize the dependence of this prediction for the branching fraction for the process $b \to s\gamma$ on the top quark mass m_t (shown in Fig. 2.5) by the formula:

$$BR(b \to s\gamma) = (1 + 0.019 \cdot m_t/GeV) \times 10^{-4}. \qquad (2.13)$$

This estimate is valid also for the process $B \to \gamma X_s$, where X_s represents the full set of the strange final states (after the hadronization). It is expected that the X_s states are dominated by the K^* resonances (listed in table 2.2). Let us note that the decay $B \to K\gamma$ is forbidden because of the momentum conservation (the K has spin zero and the massless photon cannot occur in the state with helicity zero). The calculation of the branching fractions for some simple two-body exclusive final states requires a model describing the confinement of quarks inside a meson. The model dependence results in the large theoretical uncertainty of the estimates for $\Gamma(B \to K^*(892)\gamma)/\Gamma(b \to s\gamma)$. Various calculations give results ranging from 4.5-7% ([30, 31]) up to 40% [32].

The observation of the process $B \to K^*(892)\gamma$ and decays yielding higher mass K^* resonances or the precise measurement of the upper limits on their branching fraction would result in a better estimation of $BR(b \to s\gamma)$. It was calculated by T. Altomari [31] that

$$\Gamma(B \to X_s^{'}\gamma)/\Gamma(b \to s\gamma) = 37\%, \qquad (2.14)$$

12

Table 2.2: Masses and spin-parities of K^* mesons.

Meson	J^P	Meson	J^P
$K^*(892)$	1^-	$K_2^*(1430)$	2^+
$K_1(1270)$	1^+	$K^*(1680)$	1^-
$K_1(1400)$	1^+	$K_2(1770)$	2^-
$K^*(1370)$	1^-	$K_3^*(1780)$	3^-
$K_0^*(1430)$	0^+	$K_4^*(2045)$	4^+
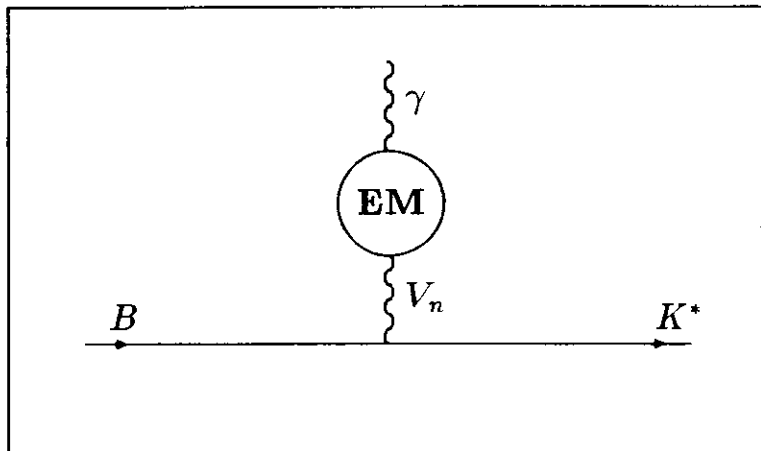
Figure 2.7: Diagram presenting contribution from long-distance interaction to the process $B \to K^*\gamma$. The intermediate state V_n denotes here any vector meson.

where X_s denotes K^* resonances with mass higher than the mass of the $K^*(892)$ and lower than the mass of the $D^*(2010)$. Therefore higher mass K^* states may give a large contribution to the $b \to s\gamma$ exclusive states.

So far we have considered only short-distance contributions to the process $b \to s\gamma$. The dominating diagram of the long-distance processes is shown in Fig. 2.7. Here the transition $B \to VK^*$, where V denotes the vector bosons ρ, ω, ϕ, J/ψ, ψ', ψ'' etc. is followed by an electromagnetic transition $V \to \gamma$. In Ref. [33] it was calculated that the branching fraction for all long-distance contributions to $B \to K^*\gamma$ is approximately 10^{-6} i.e. two orders of magnitude lower than the branching fraction arising from one-loop electro-weak process. So the decay $B \to K^*\gamma$ is dominated by short-distance effects. One should mention that at the quark level the transition $b \to sJ/\psi$, $J/\psi \to \gamma$ is forbidden as the $J/\psi \to \gamma$ transition is not allowed for a real photon.

2.2.2 The $b \to s\gamma$ transition in the extensions of the Standard Model

We discuss here the theoretical predictions for the process $b \to s\gamma$ in the extensions of the Standard Model. First we present the results of the left-right symmetric version of the Standard Model, then of theories with two Higgs doublets. In the next section we will present predictions
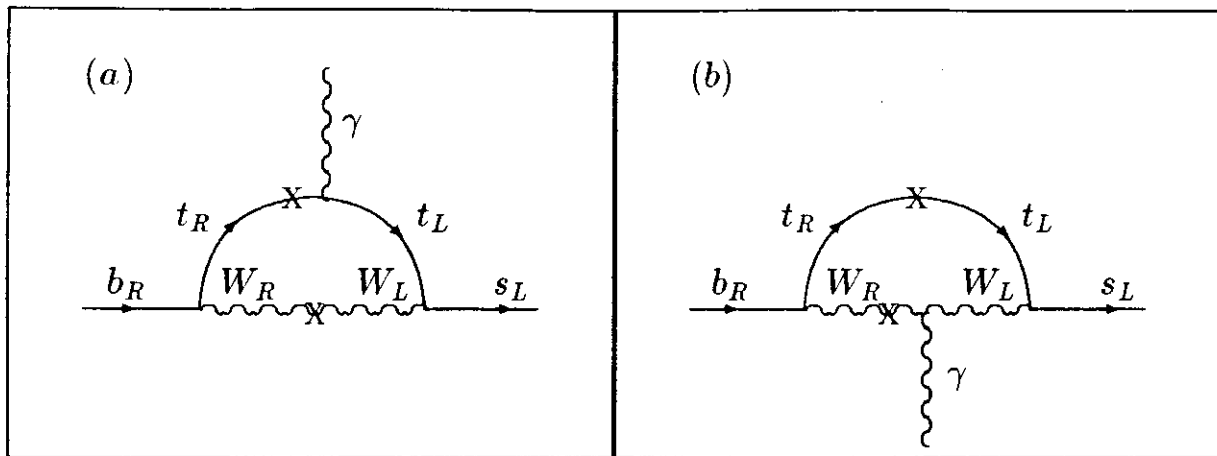
Figure 2.8: Diagrams for the $b \rightarrow s\gamma$ transition in the left-right symmetric extensions of the Standard Model. X denotes here the transition between left- and right-symmetric particles.

resulting from supersymmetric (SUSY) models. We omit here models with a fourth generation as they have been excluded by the LEP results [34].

In the Standard Model the discrete symmetries like charge conjugation and parity are broken explicitly, i.e. the Lagrangian does not conserve these symmetries while the gauge symmetry $SU(2) \times U(1)$ is broken spontaneously. In the left-right symmetric extensions of the Standard Model both kinds of symmetries are broken spontaneously and discrete symmetries are conserved in the Lagrangian, which is invariant under an $SU(2)_L \times SU(2)_R \times U(1)$ gauge transformations. In this case we have two kinds of charged currents mediated by $W_L^\pm$ and $W_R^\pm$ with the mixing between them described by the parameter ξ and we must deal with two quark mixing matrices in the left- and right-handed sectors of the model. The simplest choice is to assume that both these matrices are equal to the K-M matrix (so called 'manifest' left-right symmetry).

The experimental non-observation of the W_R mediated charged currents [1] is usually taken care of by increasing the W_R mass and by suppressing the mixing between left and right sectors. The present bound on the W_R mass is $m(W_R) > 1.6 \; TeV$ [35] while the direct bound on ξ derived from B meson decays is $\xi < 0.06$. An indirect analysis based on non-leptonic K decays yields a stronger bound of $\xi < 0.004$ [36]. Assuming the stronger bound and the 'manifest' left-right symmetry, it was shown in Ref. [1] that $BR(b \rightarrow s\gamma)$ is slightly higher than that in the Standard Model (without the QCD radiative corrections) and it rises slowly with the mass of the top quark reaching 1.5×10^{-4} for $m_t = 120 \; GeV$. This result depends however quite strongly on the values of $m(W_R)$, ξ and the K-M matrix parameters in the right-handed sector. E.g. for a looser bound of $\xi < 0.06$ the above branching fraction could be significantly bigger. On the other hand the experimental knowledge about radiative FCNC transition $b \rightarrow s$ can be used to impose constraints on the parameters of the left-right symmetric models.

Turning to the Standard Model extensions with two Higgs doublets [2] one should stress that the most reliable estimates exist for models where one Higgs doublet couples only to the $Q = 2/3$ quarks while the other couples only to the $Q = -1/3$ quarks. The crucial parameter here is the ratio of the vacuum expectation values of the two Higgs doublets, $r_H = v_2/v_1$, where v_1, v_2 corresponds the Higgs fields couplings the up and down quarks, respectively. The extension of the Higgs sector from one doublet to two (or more) results in the existence of charged Higgs bosons. The possibility of their presence in the one-loop diagram (Fig. 2.9)
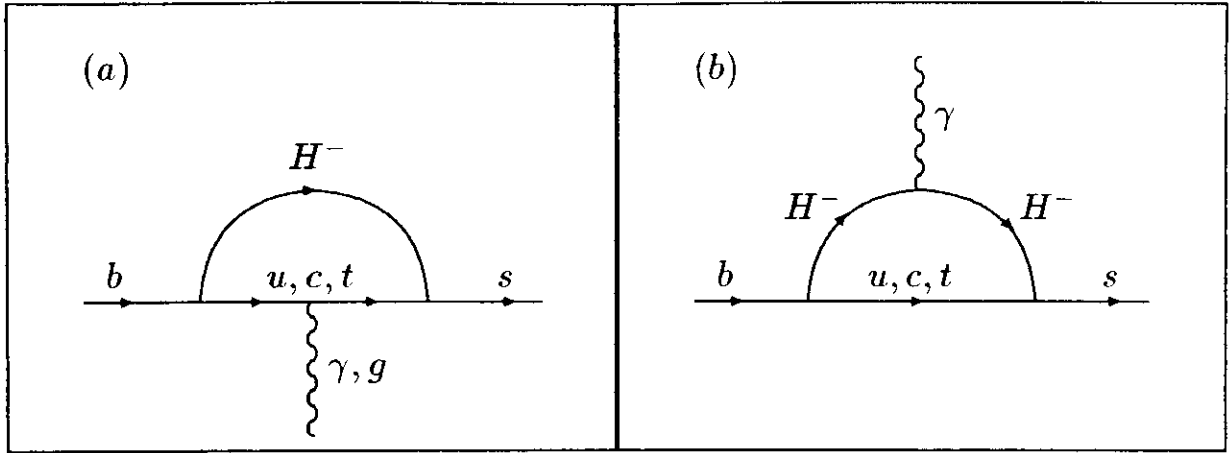
Figure 2.9: $b \to s\gamma$ transition in the Standard Model extensions with two Higgs doublets.

yields a substantial enhancement (up to one order of magnitude) of the rate for $b \to s\gamma$ in wide mass range of the top quark and charged Higgs. The largest enhancement occurs when $m_H < m_t$. It was also shown in Ref. [2] that there are quite large QCD radiative corrections for the diagrams from Fig. 2.9. In fact one can expect here $BR(b \to s\gamma)$ to be as high as 10^{-3}.

2.2.3 The $b \to s\gamma$ transition in supersymmetric theories

The crucial point of discussing rare B decays in SUSY [3] is the presence of an entirely new source of FCNC. It was shown that the vertices $\tilde{g} - \tilde{q} - q$, where $\tilde{g}$ denotes gluino and $\tilde{q}$ the squark, i.e. scalar partner of the quark q, can yield a flavour change. This is impossible for the vertices $g - q - \bar{q}$. The most important contribution to $b \to s\gamma$ comes here from the penguin diagram with gluinos and down squarks (Fig. 2.10) being exchanged.

In the $N = 1$ (N counts the number of supersymmetry generators) local SUSY model it was shown [3] that the knowledge of an upper limit of the branching fraction for the decays $b \to s\gamma$ and $b \to sg$ constraints (see Fig. 2.11) the masses of the gluino $\tilde{g}$ and the lightest squark with charge -1/3 (this quark is usually called $\tilde{b}$ although it is not a SUSY partner of the b quark). It is only in the area to the right of the solid line, in which the spontaneous breaking of the $SU(2) \times U(1)$ symmetry takes place at the correct scale. The region ruled out by the bound $BR(b \to s\gamma) \geq 10^{-3}$ is also shown (hatched area). The precise values of these constraints depend on the top quark mass m_t and the ratio v_2/v_1 of the vacuum expectations values of two Higgs doublets introduced in these theories. From Fig. 2.11 (where $m_t = 100 \ GeV$ and $v_2/v_1 = 2$ were assumed) for $BR(b \to s\gamma) \geq 10^{-3}$ we find that gluinos of few GeV's are excluded unless $m_{\tilde{b}}$ is at least 50 GeV and, in any case, gluino masses up to 50-60 GeV are ruled out for $m_{\tilde{b}} < 60 \ GeV$. These constraints would be weaker than those obtained by the UA2 collaboration [37]. They found a limit on the squark mass of $m_{\tilde{b}} > 74 \ GeV$ (90 % C.L.) independently of the gluino mass. Similarly a limit on the gluino mass is $m_{\tilde{g}} > 79 \ GeV$ (90 % C.L.) independently of the squark mass. For equal squark and gluino masses the UA2 collaboration reported a limit $m_{\tilde{q}} = m_{\tilde{g}} > 106 \ GeV$. Let us remark that for the limit on the $BR(b \to s\gamma)$ higher than 10^{-3} the region in Fig. 2.11 ruled out by this bound would be smaller and the resulting constraints on masses of the gluino and the squark would be weaker.

15
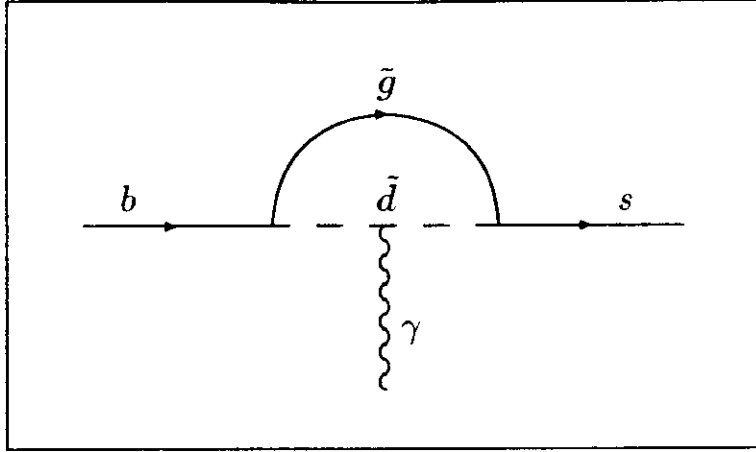
Figure 2.10: $b \to s\gamma$ transition diagram with the exchange of gluino $\tilde{g}$ and $\tilde{d}$ squark in SUSY models.
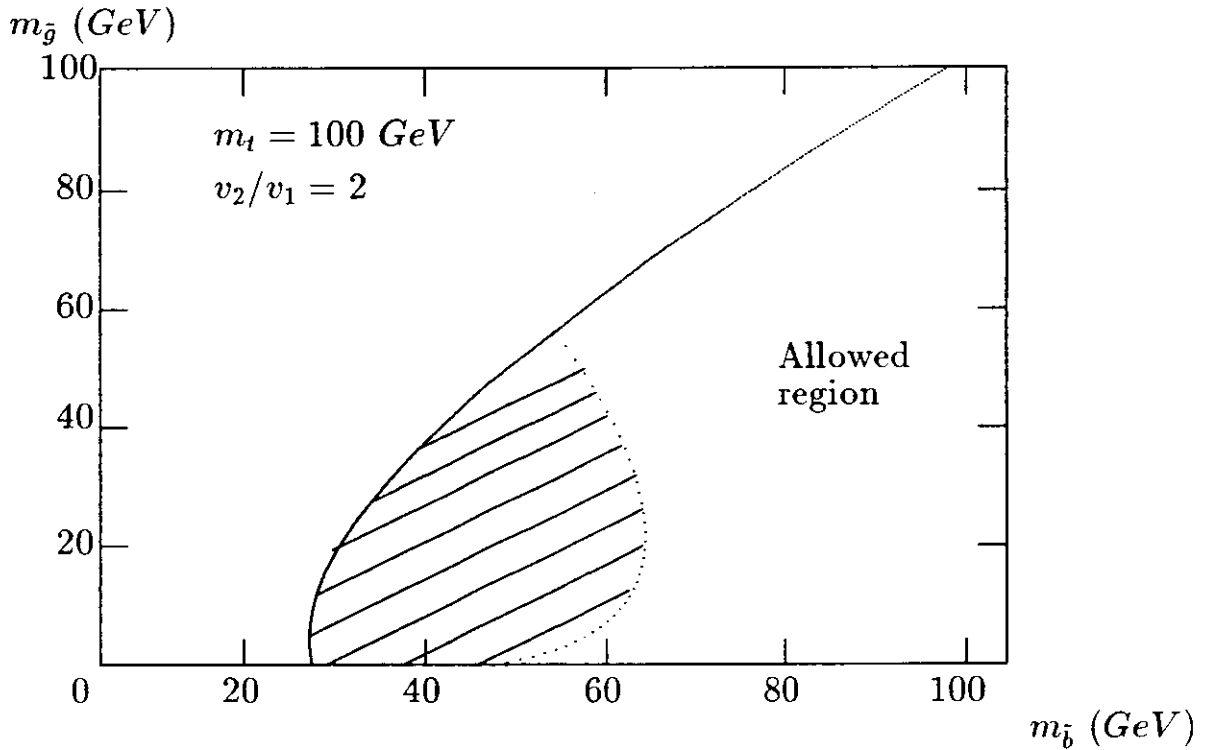
Figure 2.11: Region in the $m_{\tilde{g}}$–$m_{\tilde{b}}$ plane where $BR(b \to s\gamma) \geq 10^{-3}$ for $m_t = 100 \, GeV$ and $v_2/v_1 = 2$ (hatched area) [3]. In the region to the right of the solid line spontaneous breaking of the $SU(2) \times U(1)$ symmetry takes place at the correct scale. The 'allowed region' of values of masses of the squark and the gluino spreads to the right of the solid and dotted lines.

Table 2.3: Summary of the predictions for $BR(b \to s\gamma)$.

Model	Branching fraction
the Standard Model (SM)	10^{-4}
SM with left-right symmetry	10^{-4}
SM with two Higgs doublets	10^{-3}
supersymmetric theories	10^{-3}
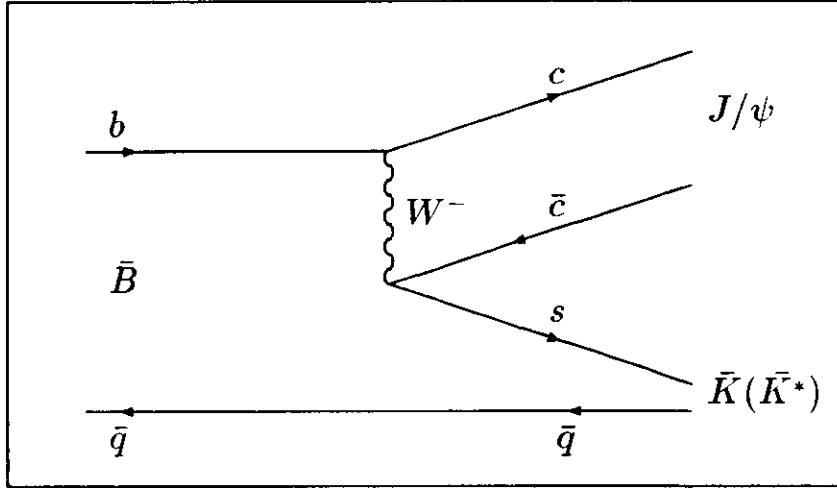
Figure 2.12: Diagram for the process $\bar{B} \to \bar{K}(\bar{K}^*)J/\psi$.

2.2.4 Summary

Measurement of the FCNC transition $b \to s$ is expected to provide valuable test of the Standard Model and its extensions. In this chapter we have discussed the theoretical predictions for the branching fraction concerning the most interesting $b \to s\gamma$ transition. The rough estimates (reliable to the order of magnitude) of this branching fraction in the models considered above are listed in Table 2.3. However the problems of QCD radiative corrections and of calculating branching fractions for exclusive channels are far from being solved in these models. The computations in the Standard Model extensions indicate an enhancement of the branching fraction for the decay $b \to s\gamma$ up to one order of magnitude over the expectation for the Standard Model. The largest enhancement up to two orders of magnitude is expected in supersymmetric theories. However, these predictions are strongly dependent on values of free parameters present in the models under investigation. The experimental estimation of the branching fraction for the process $b \to s\gamma$ down to a level of 10^{-4} would permit to distinguish between different methods of calculation of QCD corrections in the Standard Model. Further it would yield limits for the top quark mass and constraints for masses of particles predicted by the extensions of the Standard Model. Unfortunately, as we will see in the thesis, such an accuracy is outside the range of the present experimental possibilities. On the other side a larger value of this branching fraction, if observed, may indicate new physics beyond the Standard Model.

2.3 The decays $b \to sJ/\psi$, $B \to KJ/\psi$ and $B \to K^*J/\psi$

The exclusive decays $B \to KJ/\psi$ and $B \to K^*J/\psi$ are the manifestation at the hadronic level of the direct production of the J/ψ through the quark subprocess $b \to sJ/\psi$ (Fig. 2.12). As the $c\bar{c}$ pair forming the J/ψ must be a colour singlet these processes are suppressed. Taking into account the radiative QCD corrections in the leading-log approximation, the Hamiltonian for the process $b \to sJ/\psi$ is of the form (from Ref. [38])

$$\mathcal{H}_{eff}^{QCD} = \frac{G_F}{\sqrt{2}} V_{cs}^* V_{cb}(c_1 O_1 + c_2 O_2), \tag{2.15}$$

where G_F is Fermi constant. The operators O_1 and O_2 read

$$O_{1(2)} = \bar{s}_i \gamma_\mu (1 - \gamma_5) b_{i(j)} \cdot \bar{c}_j \gamma_\mu (1 - \gamma_5) c_{j(i)} \tag{2.16}$$

with the summation over the colour indices i and j. $c_{1(2)}$ are QCD renormalization constants

$$c_{1(2)} = \frac{1}{2} \left\{ [\alpha_s(m_b)/\alpha_s(m_W)]^{-6/23} \mp [\alpha_s(m_b)/\alpha_s(m_W)]^{12/23} \right\}. \tag{2.17}$$

The resulting width of the decay $b \to sJ/\psi$ is

$$\Gamma(b \to sJ/\psi) = \frac{g_{J/\psi}^2 \kappa^2 \lambda_b}{8\pi} \cong 0.01, \tag{2.18}$$

where

$$\kappa = \frac{G_F}{\sqrt{2}} V_{cs}^* V_{cb}(c_1 + c_2/3). \tag{2.19}$$

The exact form of the function λ_b depending on the masses of the J/ψ and the quarks b and s may be found in Ref. [38]. In the same paper it was shown that $g_{J/\psi}^2 = (2.38 \pm 0.14) \, (GeV)^4$. This estimate is in agreement with the experimental value (from Particle Data Group tables [39])

$$\Gamma(B \to J/\psi X) = (1.12 \pm 0.18) \times 10^{-2}. \tag{2.20}$$

For the calculation of the width for the exclusive decays $B \to KJ/\psi$ and $B \to K^*J/\psi$ we need the hadronic matrix elements $< K(k) \mid \bar{s}\gamma_\mu b \mid B(p) >$ and $< K^*(k) \mid \bar{s}\gamma_\mu (1 - \gamma_5) b \mid B(p) >$ where the p and k are the four-momenta of the B and the K meson, respectively. They are linear combinations of momenta and of four form-factors depending on $q = p - k$. The exact form of the form-factors is obtained with the help of the model proposed by M. Bauer, B. Stech and M. Wirbel [9, 38]. This yields the following formulae for the widths of the decays $B \to KJ/\psi$ and $B \to K^*J/\psi$

$$\Gamma(B \to K(K^*)J/\psi) = \frac{g_{J/\psi}^2 \kappa^2 \lambda_B^{(*)}}{8\pi}, \tag{2.21}$$

where the functions λ_B and λ_B^* depend on the known values of the respective form-factors and on the masses of the mesons which participate in the decay. Now we can calculate the following ratios:

$$\frac{\Gamma(B \to KJ/\psi)}{\Gamma(b \to sJ/\psi)} = 0.08 \qquad \frac{\Gamma(B \to K^*J/\psi)}{\Gamma(b \to sJ/\psi)} = 0.16. \tag{2.22}$$

As a result the branching fractions for the decays $B \to KJ/\psi$ and $B \to K^*J/\psi$ are estimated to be equal to $(8 \pm 2) \times 10^{-4}$ and $(16 \pm 4) \times 10^{-4}$, respectively.

3. Experimental Layout

Our data were taken at the DORIS II (**DO**ppel **RI**ng Speicher) storage ring at Deutsches Elektronen Synchrotron (DESY) in 1985–1986 with the help of the Crystal Ball detector.

3.1 DORIS II
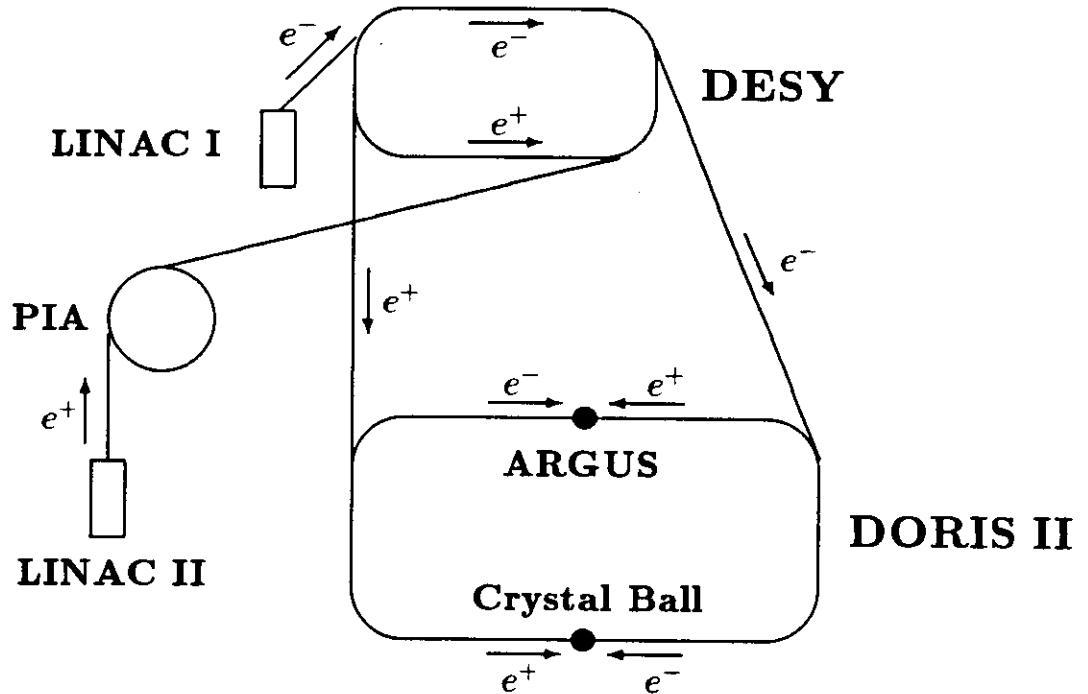
Figure 3.1: Layout of the DORIS II storage ring together with the injection system.

DORIS has been in operation since 1974 [40]. Its present version is a single storage ring with a maximum CMS energy of 11.2 GeV and with a luminosity of 10^{31} $cm^{-2}sec^{-1}$.

The DORIS II acceleration system is shown in Fig. 3.1. The electrons are emitted from a heated surface and accelerated with a linear accelerator called LINAC I to the energy of 60 MeV. Electrons are also accelerated in LINAC II to 240 MeV when they hit a tungsten target and their Bremsstrahlung radiation yields e^+e^- pairs. The positrons are then separated, cooled and accumulated in the small ring called PIA (Positron Intensity Accumulator). The electrons from the LINAC I and the positrons from PIA are injected into the DESY synchrotron where they are accelerated up to an energy of 5.3 GeV. Finally electron and positron bunches are transferred to DORIS II where they circulate and collide every microsecond in two interaction points around which the Crystal Ball (North intersection) and the ARGUS (South intersection) detectors were installed.

Each bunch contains about 10^{11} particles. In the z direction along the beam the bunch is Gaussian-like distributed with $\sigma_z = 2.1$ cm. This causes a spread of the interaction point along the beam axis which is approximately Gaussian with $\sigma = 1.5$ cm.

The energy resolution of an electron-positron storage ring is limited mainly by synchrotron radiation, which gives at DORIS II an average energy loss of about 4 MeV per revolution. This results in a beam energy spread of 9.6 MeV at FWHM. The energy loss must be compensated all the time by the high frequency transmitters. On the other hand the synchrotron radiation plays also a positive role polarizing the beams (up to 90% of polarization) due to the Sokolov-Ternov effect [41]. By destroying this polarization with an adjustable RF frequency transmitter it is possible to measure the beam energy with the best accuracy (± 0.2 MeV).
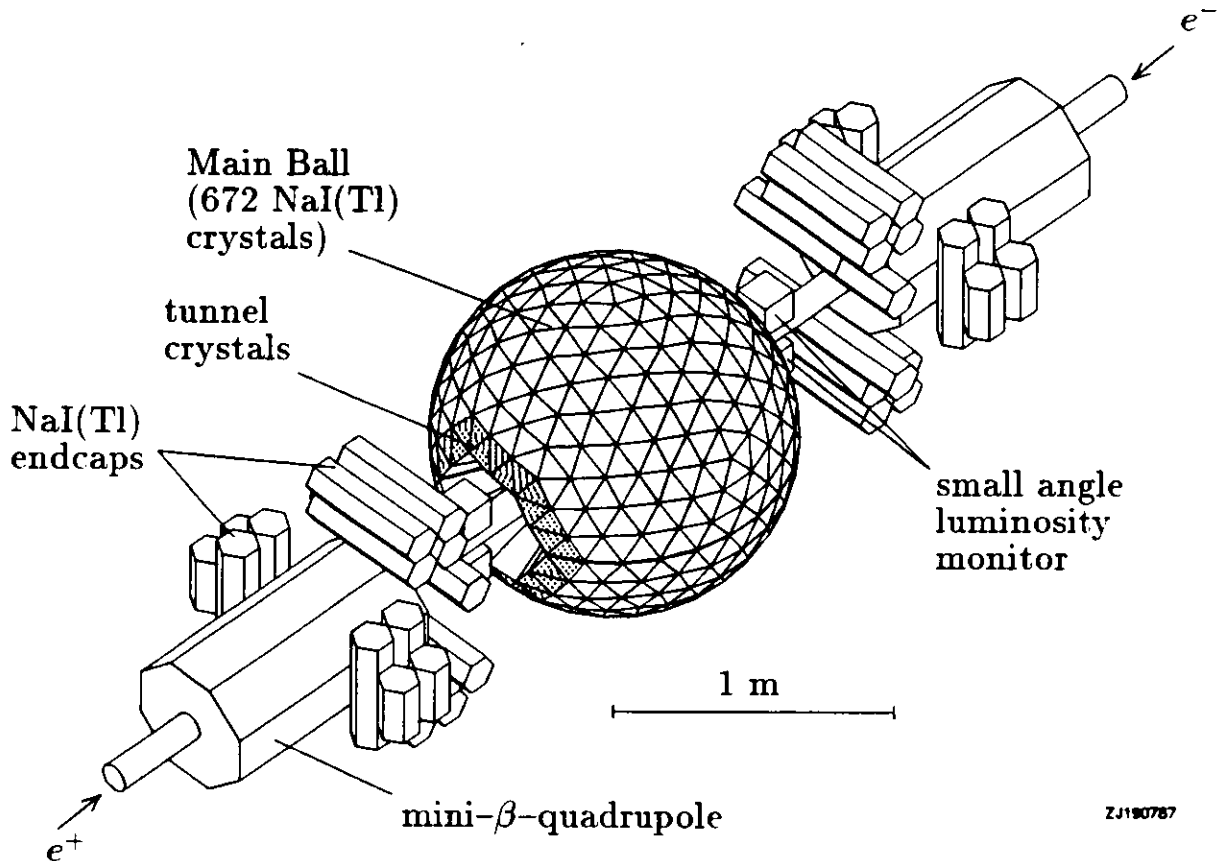
Figure 3.2: View of the Crystal Ball detector.

3.2   The Crystal Ball detector

The Crystal Ball detector [42] was designed in 1974 and started data taking in the energy region of the $c\bar{c}$ resonances at the SPEAR storage ring in SLAC, Stanford (USA) in 1978. In 1982–1986 the detector was working at DORIS II in the CMS energy range of the Υ resonances collecting a total of 264 pb^{-1} of integrated luminosity. The Crystal Ball returned to Stanford in 1987.

The experimental setup of the Crystal Ball detector is shown in Fig. 3.2. It is designed to measure precisely the energy and direction of electromagnetically showering particles. The

major part of the detector is a non-magnetic calorimeter called Main Ball, built as a spherical shell of 672 NaI(Tl) crystals covering 93% of full solid angle. Its inner radius is 10 *inch* (25.6 *cm*), while the outer one is 26 *inch* (66.2 *cm*). The beam particles enter the interaction point (centre of the sphere) via two holes in the Main Ball. The holes (also called tunnels) extend over the remaining 7% of the full solid angle. The 40 NaI(Tl) crystals of the endcaps increase the active area of the detector up to 98% of 4π. Charged particles are detected in four double layers of proportional tube chambers placed inside the shell and surrounding the beam pipe. The outer layer covers 78% of 4π. A source of additional information is a time-of-flight (ToF) system providing a shield against the cosmic background and a small-angle luminosity monitor (described in Appendix B). The whole detector (besides the ToF system which is also not shown in Fig. 3.2) is placed inside a dry house because of the hygroscopic properties of NaI(Tl).

The Main Ball has the shape of an icosahedron (Fig. 3.3). Its 20 triangle faces are called 'major triangles' and each of them is subdivided into four 'minor triangles'. Each minor triangle consists of 9 crystals. Therefore, in principle we would have 20 major triangles × 4 minor triangles × 9 = 720 crystals covering the full solid angle. Leaving room for the beam pipe reduces the number of crystals to 672 and the solid angle to 93% of 4π. Each crystal has the shape of a 16 *inch* (40.6 *cm*) long truncated pyramid. Its thickness corresponds to 16 radiation lengths and one nuclear absorption length. The 60 crystals surrounding the beam pipe are called tunnel crystals. The angular range covered by them is equal to $0.85 <| \cos\theta |< 0.93$. The crystals are optically isolated by wrapping them into white paper and aluminium foil. Each of them is connected to the photomultiplier which converts the collected light into an analog electrical signal. These signals are afterwards amplified and digitized in the two ADC (Analog to Digital Converters). The relationship between the energy deposition in the Main Ball and the ADC output is linear.

The energy resolution of the Main Ball is

$$\sigma_E/E = (2.7 \pm 0.2)\% / \sqrt[4]{E/GeV} \qquad (3.1)$$

and the spatial resolution is $(1-3)°$, slightly depending on energy.

In order to detect charged particles a set of tube chambers working in the proportional mode was mounted around the beam pipe. There were four double layers of 800 aluminium tubes filled with a gas mixture of 80% Ar, 19% CO_2 and 1% CH_4 (Fig. 3.4). The position of the hit in the z direction along the beam axis was determined by charge division with an accuracy of about 2 *cm* in the inner layers and 0.6 *cm* in the outer layers. In the azimuthal direction a resolution per double layer of 6 *mrad* in the outer and of 15 *mrad* in the inner double layers was achieved.

A variety of triggers was applied during the Crystal Ball operation. The data used in this study have been collected using the total energy trigger which required that the sum of energy depositions in all minor triangles without tunnel crystals is greater than 1800 *MeV*.
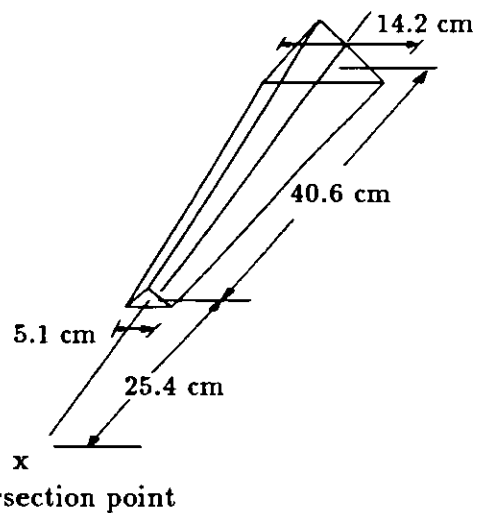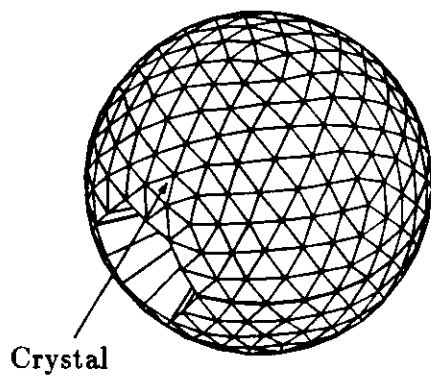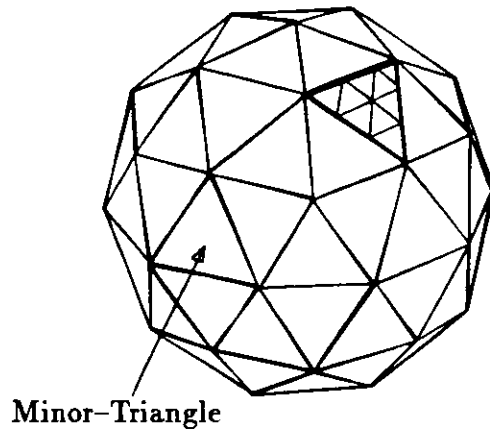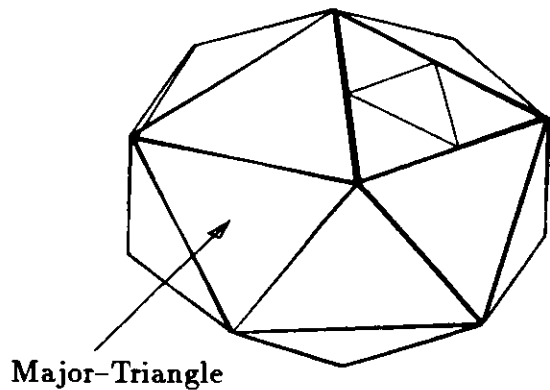
Figure 3.3: The Main Ball geometry. The upper pictures show the division of the ball into major and minor triangles. The lower pictures show respectively: the division into individual crystals and the shape of one of them.
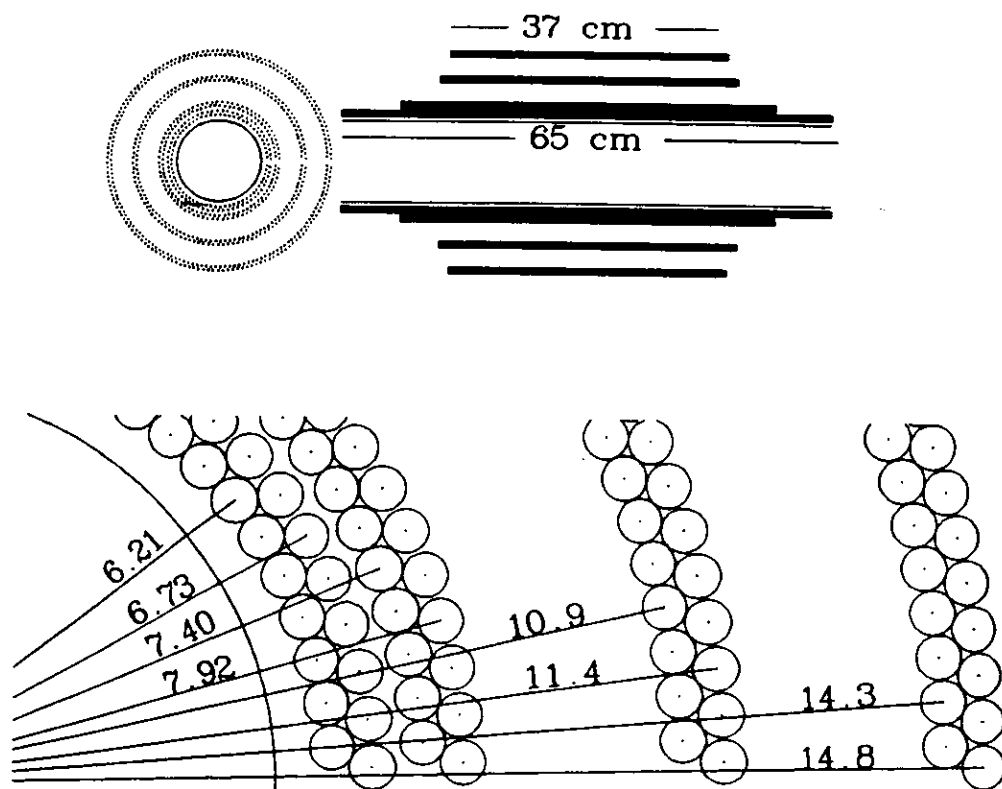
Figure 3.4: View of the tube chamber system. The upper left and lower parts of the picture represent the projection in the plane perpendicular to the beam axis with the distances from the beam axis to the different layers in *cm*. The upper right part of the picture shows the projection onto a plane containing the beam axis.

4. Data Processing

Our data sample was taken at the centre of the $\Upsilon(4S)$ resonance with an integrated luminosity of 75.9 pb^{-1} (so-called ON $\Upsilon(4S)$ data) and in continuum below the resonance peak with an integrated luminosity of 18.5 pb^{-1}. In this chapter we describe the procedures of reconstruction of energies and directions of particles from the raw data; selection of multi-hadron events will be also presented. Finally we determine the number of genuine $B\overline{B}$ pairs in our data sample.

4.1 Reconstruction program

The raw data written on magnetic tapes are processed by the reconstruction program. This procedure is called 'data production'. The electronic counts, e.g. digital signals from the photomultipliers of the crystals and the pulse heights at each end of the chambers are then converted into physical quantities, like energies of individual crystals or the hit coordinates in the tube chambers. From them the information about energies and directions of detected particles can be obtained. In this chapter we describe these aspects of the reconstruction algorithm which are important for our study.

The first step of the reconstruction is the recalculation of the ADC counts into energies deposited in individual crystals (see Apppendix A).

After determining the crystal energies we search within the Main Ball for energy clusters called 'connected regions'. A set of crystals forms a connected region if each member of it has an energy deposition of at least 10 MeV and if it shares a vertex or a face with another crystal of this set (see Fig. C.1 in Appendix C for examples). The sum of energy depositions of all crystals belonging to it will be denoted as E_{CONREG}.

Next one looks for local maxima in the energy distribution within each energy cluster. This is done by an empirical algorithm called BUMPS. First, the crystal with the highest energy in a connected region is labelled a 'bump' (see Fig. 4.1) and three nearest neighbours are associated with it. The sum of energies of these four crystals is called E_4 (Fig. 4.1).

Additional crystals belonging to this connected region are associated with the bump crystal if the angle β between the centres of the bump and the crystal under investigation is smaller than 15^0 or if

$$15^0 < \beta < 45^0 \quad and \quad E_{CRYSTAL} < E_4 \times 0.72 \times \exp[(-9.4(1 - \cos\beta)]. \tag{4.1}$$

This empirical formula was obtained by scanning Monte Carlo events. The crystal with the highest energy and not yet associated to the bump is called the next bump crystal and the procedure is repeated until all crystals in a connected region are associated to bumps.

In the following the information from the tube chambers is used to distinguish between charged and neutral particles. First the raw tube chamber data i.e. pulse heights at each end of a tube are converted into hit coordinates in the chambers with the help of the method of charge division.

At this stage we attempt to fit straight line trajectories to the hits in the chambers. If there are at least three hits which can be fitted to the straight line passing through the vertex this track is called IR (Interaction Region) track. The IR track whose direction forms an angle
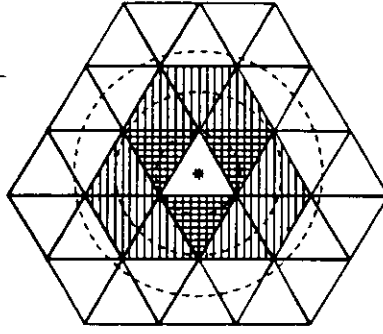
Figure 4.1: Three nearest layers of crystals surrounding the bump crystal (with the energy E_1; marked with an asterisk in the centre). The energies of the first layer (area of crossed lines) together with the bump energy add to the energy E_4. Adding the energies of the second and third layer (vertical lines and blank areas, respectively) results in the energies E_{13} and E_{37}. The dashed circles represent Moliére radii described in Appendix C.

smaller than 15° with the direction to the centre of the bump crystal is associated with this bump as a 'tracked charged' particle and its direction is defined as the fitted direction of the track. If two or more tracks are associated to a bump the closest track is assigned to the bump.

All the remaining hits which have not been associated to tracked charged particles are used to check if any of the other bumps correspond to the charged particles. A special algorithm looks through the bumps and if a small window in the azimuthal angle ϕ ($\delta\phi = 0.15\ rad$) and in the z coordinate measured along the beam direction ($\delta z = 8, 8, 5, 5\ cm$ in four layers of the chambers) contains at least two hits this bump is called 'tagged charged'. For all remaining bumps neutral charge is assumed.

The aim of the next step is to assign energy to all tracks and to determine the directions of the neutral and the 'tagged charged' particles (for the 'tracked charged' ones this was done previously). For the purpose of this study the particle energy was calculated as the sum of energies of the bump crystal and its 12 closest neighbours (see Fig. 4.1). This so-called E_{13} energy is corrected for two effects. One correction of 2.25% is due to the energy deposited outside of the group of 13 crystals. Secondly, the energy fraction deposited in 13 crystals depends on the entry point of the particle into the crystal. A particle entering near a crystal border will leave more energy in the wrapping medium of the crystals than a particle entering near to its centre. As a measure of this so-called position correction 'PCORR' we take the ratio E_1/E_{13} and we use an empirical function obtained from analysis of events coming from Bhabha scattering $e^+e^- \rightarrow e^+e^-$:

$$PCORR(E_1/E_{13}) = \begin{cases} 1.055 & if \quad E_1/E_{13} < 0.4 \\ (1/(0.898 + 0.125 E_1/E_{13}) & if \quad 0.4 < E_1/E_{13} < 0.82 \\ 1 & if \quad E_1/E_{13} > 0.82. \end{cases} \qquad (4.2)$$

Finally the energy is calculated as

$$E_{13}^{CORR} = 1.0225 \times PCORR(E_1/E_{13}) \times \sum_{i=1}^{13} E_i. \qquad (4.3)$$

In order to determine the directions of non-IR tracks each bump crystal is divided into 16 sub-crystals. The algorithm compares the observed energy distribution in the group of 13 crystals

25

entries / 50 *MeV*
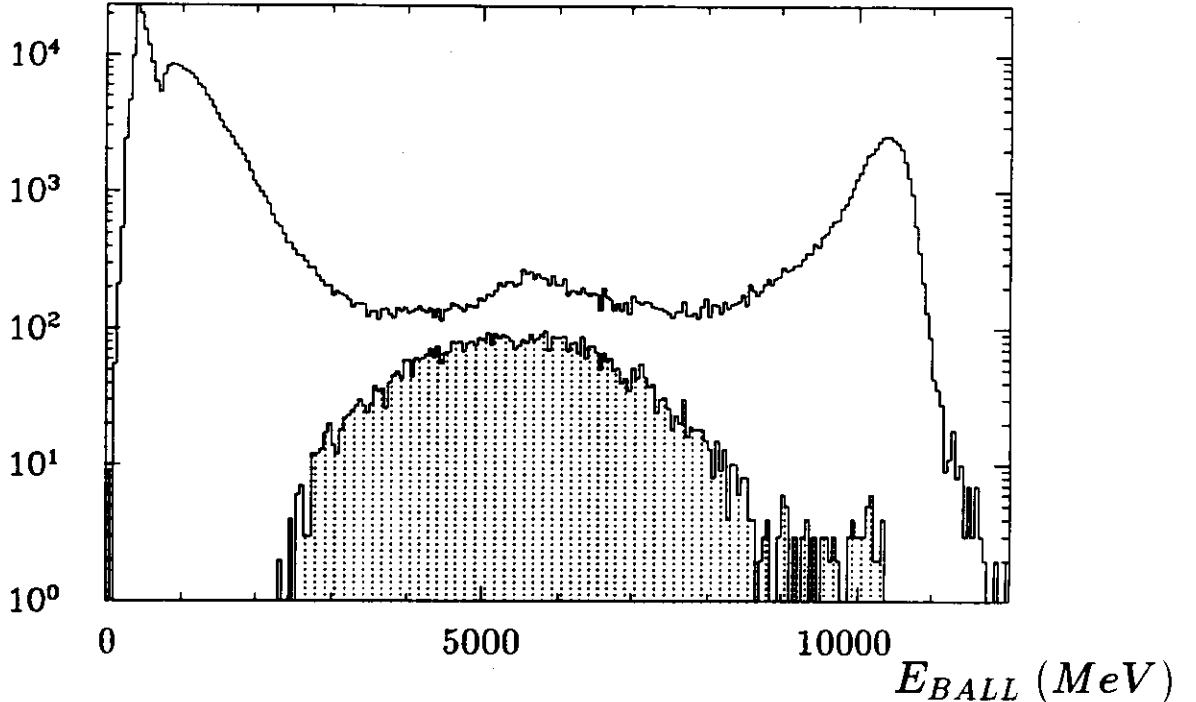
Figure 4.2: The energy deposited in the Main Ball E_{BALL} for events recorded on one magnetic tape during data taking. Multi-hadron events are shown as shaded area. Watch the vertical scale which is logarithmic.

with the distribution expected for Monte Carlo photons, when the particle enters the centre of each one of these 16 subcrystals. The direction of the track is taken from the subcrystal for which there is the smallest difference between observed energy deposition and its predicted shape.

4.2 Selection of multi-hadron events

The next step in the data processing is the selection of multi-hadron events from the decay of the $\Upsilon(4S)$ resonance ($B\overline{B}$ events are obviously expected in this sample). Unfortunately only a few percent of the triggers on the raw data tape are of that type. This can be seen from the total energy distribution for all the triggers from one raw data tape and for the final sample of hadronic events (Fig. 4.2). The low energy triggers in this picture are due to cosmic rays, beam-gas interactions and $\gamma\gamma$-reactions. Triggers around 10 GeV correspond to Bhabha scattering. Hadronic events are between these two peaks for energy E_{BALL} ranging from 2.5 GeV to 10.5 GeV. The energy E_{BALL} is defined as the sum of energy deposits in all crystals of the Main Ball

$$E_{BALL} = \sum_{i=1}^{672} E_i. \qquad (4.4)$$

The background to hadronic events in this energy interval comes mainly from two photon interactions, QED events like $e^+e^- \rightarrow l^+l^-(\gamma)$, where $l = e,\mu,\tau$ (the tail in Fig. 4.2 at $E_{BALL} \geq 10$ GeV is due to Bhabha events faking multi-hadron ones), and beam-gas or beam-

wall interaction. Most of this background can be removed by the selection of hadronic events, which is based on cuts on event parameters like energy, multiplicity and parameters describing the topology of the event. In this analysis the selection of hadronic events is done by the standard Crystal Ball program [43]. Now we describe our selection cuts in some detail. One should note that after applying this procedure our hadronic event sample contains not only multi-hadron events from the $\Upsilon(4S)$ resonance but also non-removable background of hadronic events generated in non-resonant production. Fig. 4.3 shows a Mercator type display of the Main Ball for a multi-hadron event.

The beam-gas and beam-wall interactions are efficiently reduced by a cut in the (β, x_{trans}) plane, where

$$\beta = \left| \sum_{i=1}^{672} E_i \, \hat{p}_i \right| / E_{BALL} \tag{4.5}$$

is the absolute value of the normalized vector sum of the crystal energies and measures the energy imbalance of an event ($\hat{p}_i$ is a unit vector pointing to the centre of the ith crystal in which energy E_i was deposited) and

$$x_{trans} = \left(\sum_{i=1}^{672} E_i \, \sin \theta_i \right) / W \tag{4.6}$$

is the normalized transverse energy of an event (θ_i is the polar angle with respect to the e^+ beam direction of the ith crystal). The centre-of-mass energy is

$$W = 2E_{BEAM}, \tag{4.7}$$

where E_{BEAM} is the beam energy.

Hadronic events must satisfy the following requirements:

- $0.1W < E_{BALL} < 1.5W$.

- $x_{trans} > 0.2$, $\beta < 0.7$ and $x_{trans} > 0.5\,\beta + 0.1$.

The upper limit of the first cut was set to $1.5W$ in order to reject some rare events of cosmic background and beam-dump. Fig. 4.4 shows the plane (β, x_{trans}) for ON $\Upsilon(4S)$ events and for single-beam data with the above cut (solid line). The rejection of beam-related background is clearly seen.

As beam-gas and beam-wall interactions deposit a large fraction of energy at small angles we apply also the cuts:

- $E_{TUNNEL}/E_{BALL} < 0.5$ and $E_{ENDCAPS}/E_{BALL} < 0.4$,

where E_{TUNNEL} and $E_{ENDCAPS}$ are the sums of the energies of the 60 tunnel crystals adjacent to the beam pipe and of the endcap crystals, respectively.

In order to suppress Bhabha events we demand a minimum multiplicity, i.e.

- at least three connected regions, each with $E_{CONREG} > 100 \ MeV$.

Further suppression of radiative Bhabha events with photons of energy greater than $100 \ MeV$ is obtained as follows:

- There should be at most one connected region with $E_{CONREG} > 0.80\,E_{BEAM}$.

- There cannot be any connected region with $E_{CONREG} > 0.80\,E_{BEAM}$ if $E_{BALL} > 0.75\,W$.

Events satisfying the above requirements are called hadronic ones and we denote their number by N_{vis}^{had}.
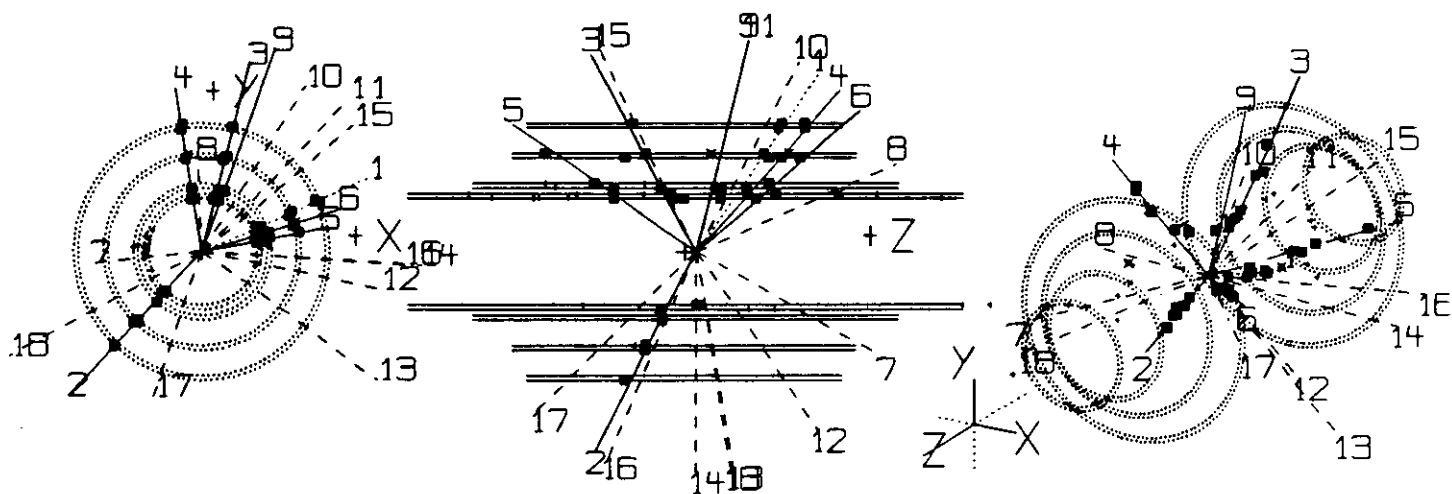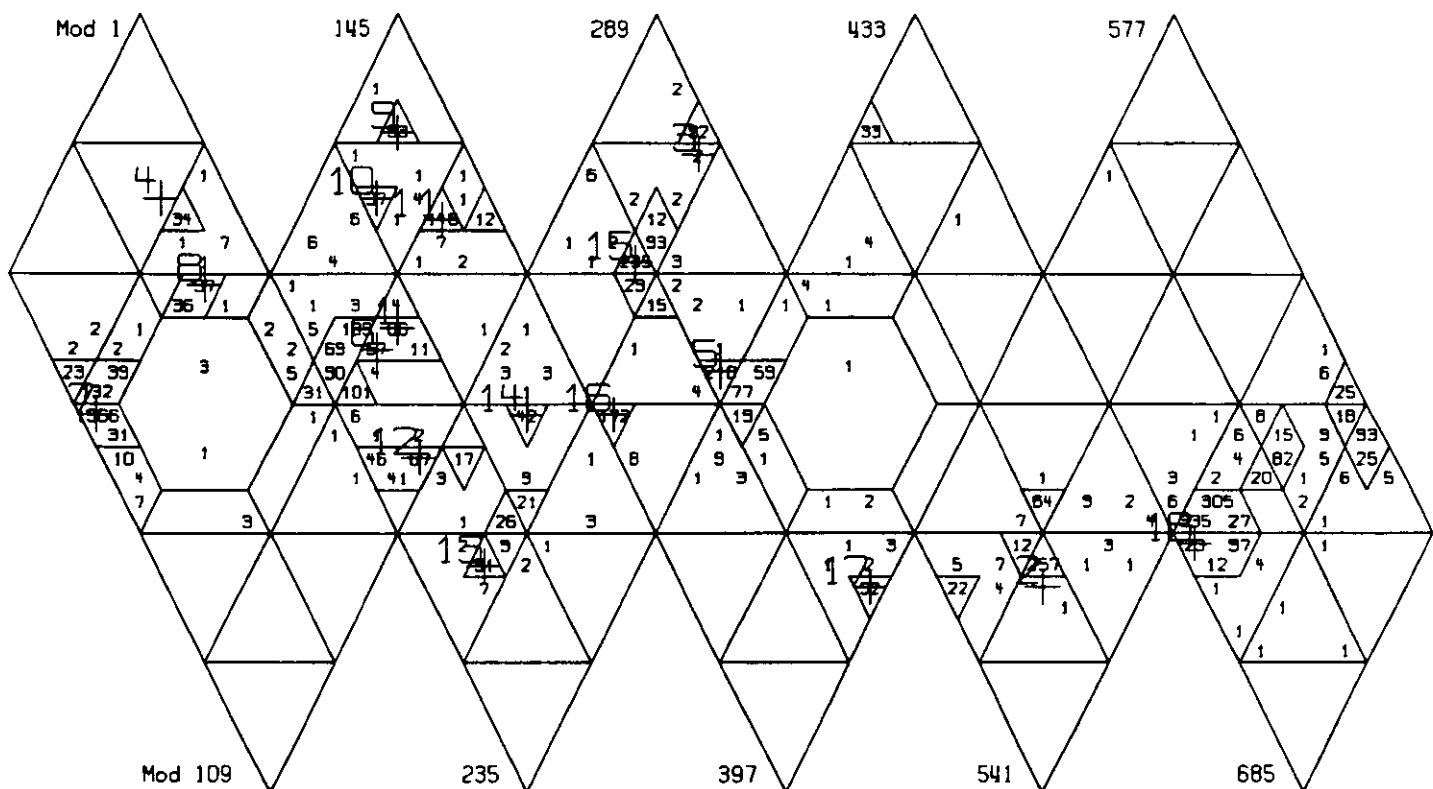
Figure 4.3: A Mercator type display of the Main Ball for one hadronic event. The numbers represent energies (in MeV) deposited in the individual crystals. Only minor triangles are marked. The energy clusters (connected regions) are surrounded by solid lines. The crosses mark positions of local maxima of the energy deposits (bumps). The lower part of the picture shows hits in the tube chambers in various projections with tracks corresponding to charged and neutral particles presented as solid and dashed lines, respectively.

28
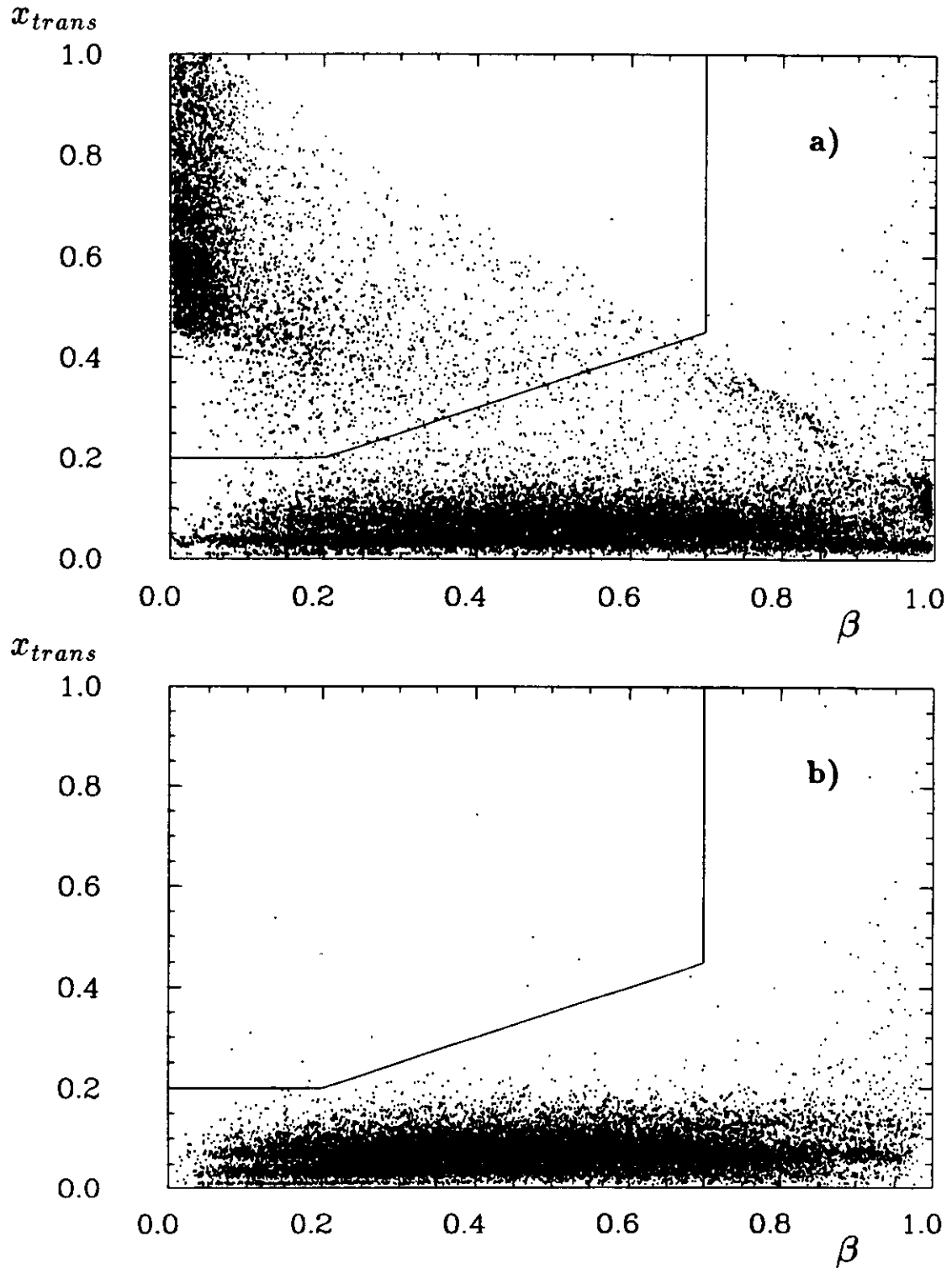
Figure 4.4: (β, x_{trans}) plane for (a) ON $\Upsilon(4S)$ data and (b) single-beam data. Our cut is shown as a solid line. We accept events in the upper left part of the plane.

4.3 Data sample

The data samples used in this analysis were taken in 1985 and 1986 (see Fig. 4.5) on the $\Upsilon(4S)$ resonance (75.6 pb^{-1}) at the beam energy of (5.290 ± 0.005) GeV and in the continuum below this resonance (18.5 pb^{-1}) in the beam energy range from 5.23 GeV to 5.26 GeV (see Table 4.1). The author participated in the data taking in 1985.

4.3.1 Visible hadronic cross-section

The visible hadronic cross section is calculated as

$$\sigma_{vis}^{had} = \frac{N_{vis}^{had}}{L}, \tag{4.8}$$

where L is the integrated luminosity (see Appendix B). It has been measured at several values of the centre-of-mass energy W (Fig. 4.6) around the position of the $\Upsilon(4S)$ resonance. As it can be seen from Fig. 4.6 the total visible cross-section is equal to about 3.6 nb at the maximum. However, the contribution from the continuum is large, i.e. about 2.7 nb and the ratio of the $\Upsilon(4S)$ resonance signal to the continuum background is 1 : 3.

Table 4.1: Data samples used in the analysis.

	ON $\Upsilon(4S)$	continuum
luminosity (pb^{-1})	75.9 ± 0.8	18.5 ± 0.4
number of Bhabha events(N^{Bh})	874035	217146
number of multi-hadron events observed (N^{had})	288563	56720

4.3.2 Number of multi-hadron events from the $\Upsilon(4S)$ resonance

The estimation of the number of multi-hadron events from the $\Upsilon(4S)$ resonance N_{4S}^{had} requires the knowledge about the contribution from the continuum. This can be achieved by taking data not only at the resonance but also at energies outside the maximum (in this case 30 to 60 MeV below the peak). Let us denote the number of multi-hadron events and the number of Bhabha events measured outside the resonance by N_{OFF}^{had} and N_{OFF}^{Bh}, respectively. The same quantities measured at the peak are N_{ON}^{had} and N_{ON}^{Bh}. The number of multi-hadron events arising from the resonance (the number of $B\bar{B}$ pairs) can be determined in the following way:

$$N_{4S}^{had} = N_{B\bar{B}}^{vis} = N_{ON}^{had} - N_{OFF}^{had} \times \frac{N_{ON}^{Bh}}{N_{OFF}^{Bh}} = (60.3 \pm 1.1) \times 10^3. \tag{4.9}$$

The quantity $r_{lum} = N_{ON}^{Bh}/N_{OFF}^{Bh}$ which represents the luminosity scale factor is in our case equal to 4.025 ± 0.009. For details concerning the luminosity measurement see Appendix B. The error of 1.7% on $N_{B\bar{B}}^{vis}$ is dominated by the statistical error of the continuum sample of 0.4% multiplied by the luminosity ratio factor r_{lum}. The smaller contributions are: 0.2% uncertainty in r_{lum}, and less than 0.2% from a possible difference between the beam-gas background contribution of the ON $\Upsilon(4S)$ and the continuum data samples.

Integrated luminosity (pb^{-1})
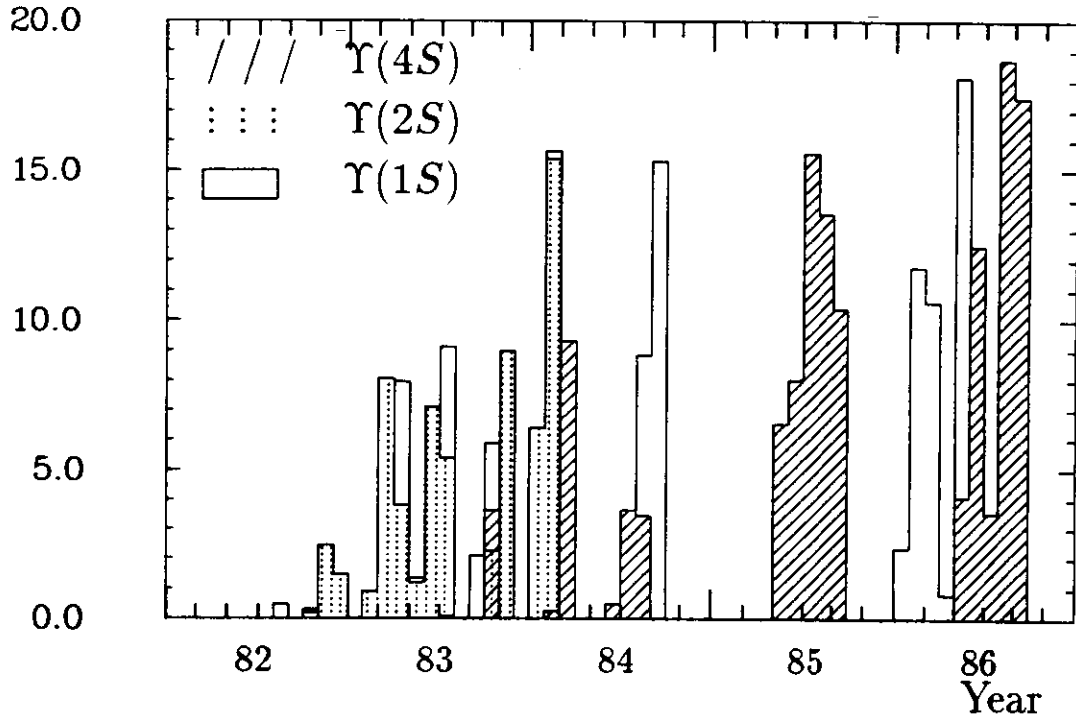
Figure 4.5: The integrated luminosity (per month) collected by Crystal Ball at DORIS II. The open histogram represents data from the $\Upsilon(1S)$ resonance peak and nearby, the dotted and hatched histograms correspond to the $\Upsilon(2S)$ and $\Upsilon(4S)$, respectively. It is only the $\Upsilon(4S)$ events collected in 1985-86 which are used in this work.

$\sigma_{vis}^{had}\ (nb)$
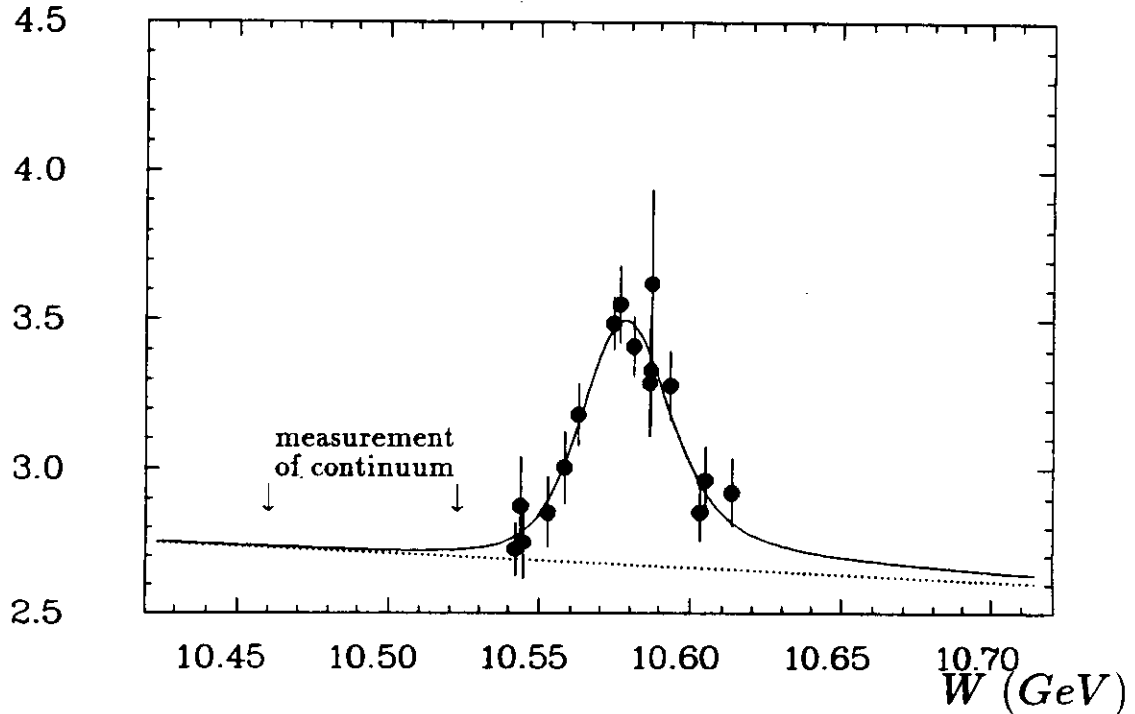
Figure 4.6: Visible hadronic cross-section as a function of the centre-of-mass energy W at the $\Upsilon(4S)$ resonance. The curve is drawn solely to guide the eye. Watch the vertical scale which does not start from zero. Arrows mark the region of the centre-of-mass energy in which the continuum data sample was taken.

31

5. Data analysis

In this chapter we present the search for the flavour changing neutral current $b \to s\gamma$ ($B \to K^*\gamma$), as well as for the decays $B \to KJ/\psi$ and $B \to K^*J/\psi$ in our data. The selection cuts, the fits to the selected data, the procedure of efficiency calculation and the estimation of systematic errors are described.

5.1 Reduction of non-$B\overline{B}$ events

First we try to enhance the ratio of the number of multi-hadron events from the decays $\Upsilon(4S) \to B\overline{B}$ to the number of events from hadronic continuum and to reduce background from $\tau^+\tau^-$ events in our hadronic data sample. This is achieved by applying cuts on the event multiplicity and topology. We expect that $B\overline{B}$ events are more spherical and of higher multiplicity than continuum ones. $\tau^+\tau^-$ events are jet-like and also of a lower multiplicity. As a quantitative measure of the event topology we use the second Fox-Wolfram moment $H2$ [44]. It is close to zero for spherically-symmetric events and near to one for jet-like events. This moment is defined here as:

$$H2 = \frac{\sum_{i,j=1}^{N_{bumps}} E_1^i E_1^j (3\cos^2 \alpha_{i,j} - 1)}{2(\sum_{k=1}^{N_{bumps}} E_1^k)^2}, \tag{5.1}$$

where E_1^i is the energy deposition in the bump module i, and $\alpha_{i,j}$ is the angle between the i-th and j-th bump directions. We use a non-standard definition because usually the Fox-Wolfram moments deal with the momenta of the particles. Unfortunately they are not known here since the Crystal Ball is a non-magnetic detector. The detector measures only a small fraction of the energy of charged hadrons (2/3 of all hadrons, 1/2 of them interact in the detector). Therefore the energies E_{13} or E_{CONREG} are not good measures of the particle energy in the definition of the Fox-Wolfram moments and using them we would underestimate the energy contribution from charged hadrons in comparison to electromagnetically showering particles. Monte Carlo studies showed that this imbalance almost disappears while applying the energy of the bump crystal E_1 (it underestimates energies of electromagnetically showering particles and hadrons approximately in the same way).

Selecting the sample of $\Upsilon(4S) \to B\overline{B}$ events which will be further used to search for photons from the decay $b \to s\gamma$ we demand that:

- the second Fox-Wolfram moment $H2$ is < 0.4,

- the total number of local energy maxima (bumps) is ≥ 8.

Similar cuts are used in the search for the decays $B \to KJ/\psi$ and $B \to K^*J/\psi$

- the second Fox-Wolfram moment $H2$ is < 0.5,

- the total number of local energy maxima (bumps) is ≥ 7.

Events / 0.05
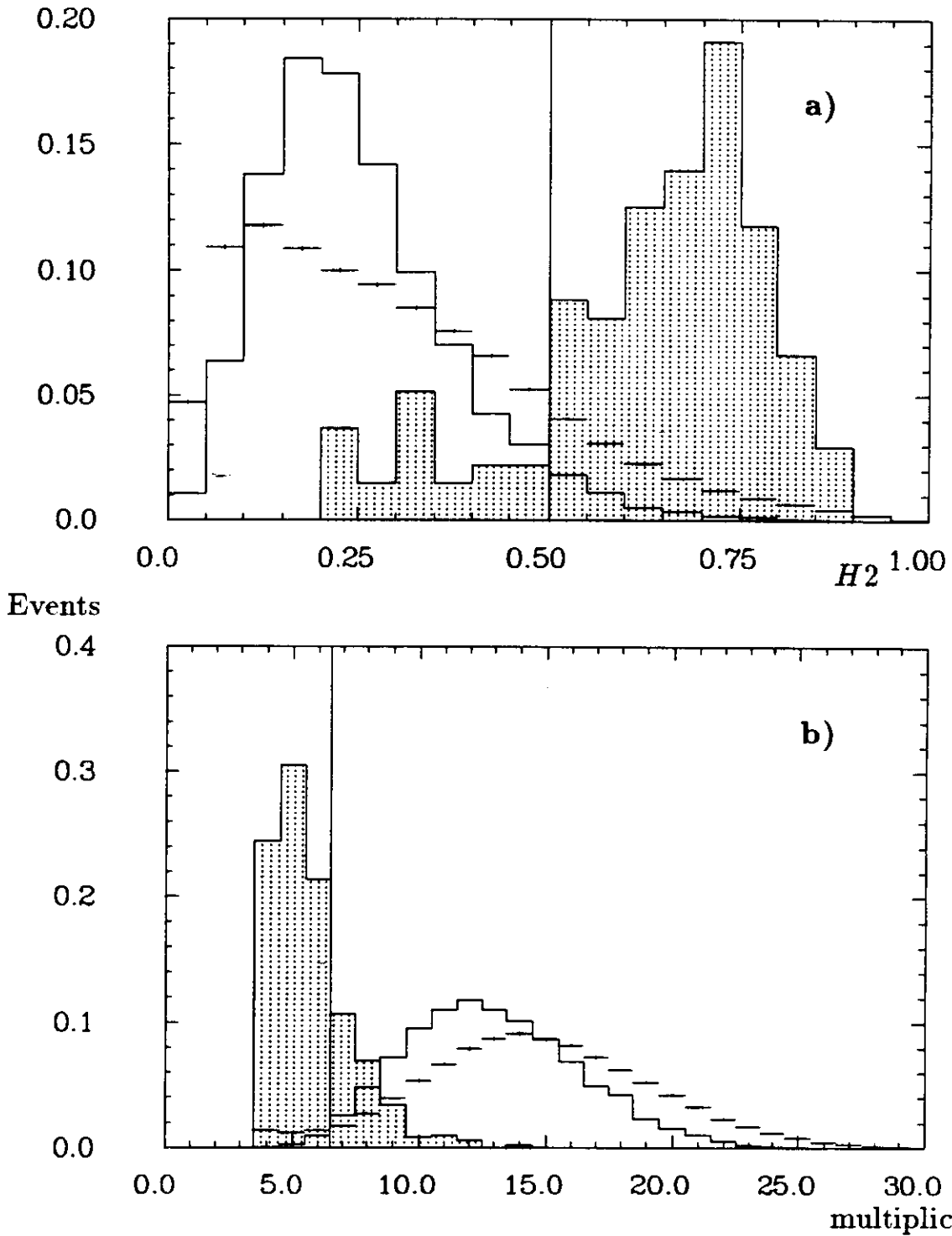
Figure 5.1: Distributions of the second Fox-Wolfram moment $H2$ (a) and of the multiplicity (total number of bumps) (b) for ON $\Upsilon(4S)$ data (solid segments) and for the Monte Carlo sample simulating the process $\Upsilon(4S) \rightarrow B\overline{B}, B \rightarrow K^*(892)J/\psi$ (solid histogram) and for the Monte Carlo prediction for the $\tau^+\tau^-$ contribution (shaded histogram). All distributions are normalized to the same area. The cuts are shown by vertical lines.

$$(dN/d\ln(E_{13}^{CORR'}))/0.03$$
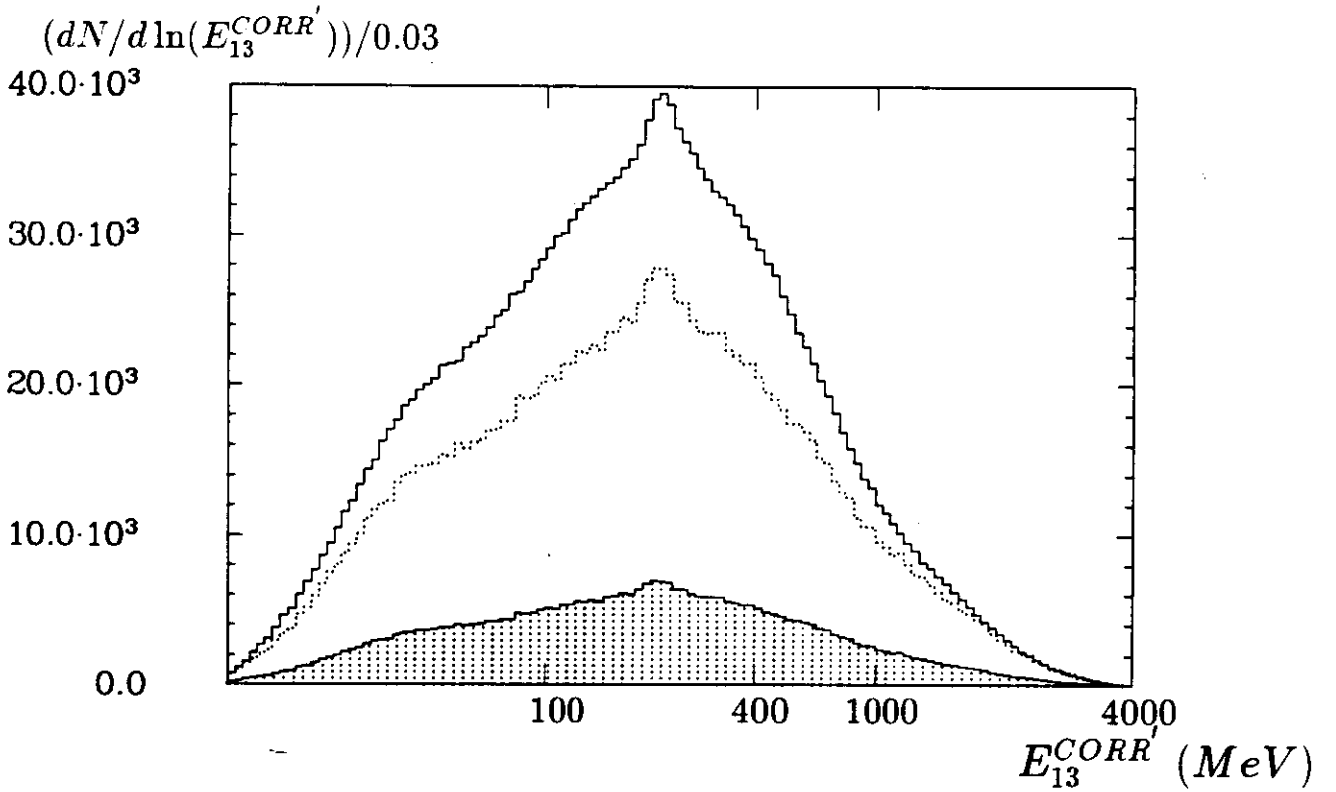
Figure 5.2: Spectrum of neutral particles from ON $\Upsilon(4S)$ (solid histogram) and continuum (shaded histogram) data samples before applying our selection cuts. The dotted histogram represents continuum spectrum scaled by a factor $r_{lum} = 4.025$ (cf. sec. 4.3.2).

Monte Carlo studies showed that after these last two cuts almost no $\Upsilon(4S) \to B\overline{B}$ events are lost ($< 2\%$). At the same time we rejected at least 16% of continuum and 84% of $\tau^+\tau^-$ events, respectively. Fig. 5.1 show the $H2$ and multiplicity distributions for ON $\Upsilon(4S)$ data and for Monte Carlo data simulating the process $\Upsilon(4S) \to B\overline{B}, B \to K^*(892)J/\psi$.

5.2 Search for the process $b \to s\gamma$ $(B \to K^*\gamma)$

After reduction of events which do not originate from the decays $\Upsilon(4S) \to B\overline{B}$ we select events with high-energy photons. Studying their inclusive spectrum we will look for any photons coming from the process $b \to s\gamma$. This sample allows also a search for exclusive decays $B \to K^*\gamma$.

5.2.1 Topology of $B \to K^*\gamma$ events

We look for the process $B \to K^*\gamma$ (one should remind that the decay mode $B \to K\gamma$ is forbidden because of the conservation of angular momentum) where the B meson comes from the $\Upsilon(4S)$ decay into a $B\overline{B}$ pair. The $\Upsilon(4S)$ resonance decays at rest and the momentum of the $B(\overline{B})$ meson is very small (about 320 MeV/c) since the $B\overline{B}$ threshold is just below $\Upsilon(4S)$ mass. Therefore $B(\overline{B})$ mesons decay almost at rest. As a result we expect a fairly isotropic angular distribution of their decay products in the laboratory frame.

In case of the two-body $B \to K^*\gamma$ decay the K^* and the high-energy photon (about 2.5 GeV) are emitted almost exactly in opposite directions in the laboratory frame since the B meson is very slow. The products of the K^* decay lie in a relatively narrow cone with a maximum opening angle of maximum 35° around the K^* direction. Therefore the process under investigation

should manifest itself in a more abundant production of particles in the direction opposite to that of the selected photon, i.e. in the presence of at least one particle in a cone with opening angle greater than 145° with respect to the photon. As the Crystal Ball detector is not able to identify the K^* decay products we can only search for the process $B \rightarrow K^* \gamma$ by investigation of the inclusive photon spectrum and of the distribution of the largest angle formed between the direction of the selected photon and the direction of any other particle. We mark this angle by α. The particle with the biggest opening angle with respect to the photon will be called 'opposite' one.

This picture of the $B \rightarrow K^* \gamma$ decay topology is based on the Monte Carlo study of the kinematics of the above process (Appendix D).

5.2.2   Photon selection

We describe here the selection of high-energy photon candidates. They are defined as well separated neutral clusters with the lateral pattern of their energy deposition consistent with that of electromagnetically showering particles. The energy spectrum of all neutral particles from ON $\Upsilon(4S)$ and continuum events is shown in Fig. 5.2. As a measure of a particle energy we use here the energy $E_{13}^{CORR'}$, which is the energy E_{13}^{CORR} as described in Chapter 4 with the application of a small empirical correction discussed in Appendix A. Now we apply various cuts.

The first cut selects only high-energy photon candidates:

- $E_{13}^{CORR'} > 1000 \; MeV$

since such photons are expected from $B \rightarrow K^* \gamma$ decay.

The next two requirements reject charged particles, e.g. electrons. The cut in the polar angle θ

- $\mid \cos \theta \mid < 0.75$

selects particles which pass all four layers of the tube chambers and thus ensures reliable charge information. Here the particle direction is determined from the Main Ball only, and not from the tube chambers.

- The particle is recognized as neutral by the standard reconstruction procedure.

The standard Crystal Ball tag for neutral particles is the presence of at most one hit in the tube chambers pointing to the cluster seen in the main detector as described in Chapter 4.

The next pair of cuts chooses well separated high-energy photon candidates (isolation cuts):

- There should be only one local maximum of energy (bump) in a given cluster (connected region).

- $E_{24h} < 40 \; MeV$.

The E_{24h} energy is defined as the highest energy deposit in a single crystal belonging to the layer of 24 third order neighbours. In case of a connected region corresponding to a single particle this parameter should be small because almost the whole particle energy is deposited in the nearest two layers. If the directions of two or more particles are close to each other their energy clusters overlap and the value of E_{24h} is usually much bigger. In Fig. 5.3 we present the

35

E_{24h} (MeV)

500.0

400.0

a)

300.0

200.0

100.0

0.0

1000.0   2000.0   3000.0 $E_{13}^{CORR'}$ (MeV) 4000.0

E_{24h} (MeV)

500.0

400.0

b)

300.0

200.0

100.0

0.0

1000.0   2000.0   3000.0 $E_{13}^{CORR'}$ (MeV) 4000.0
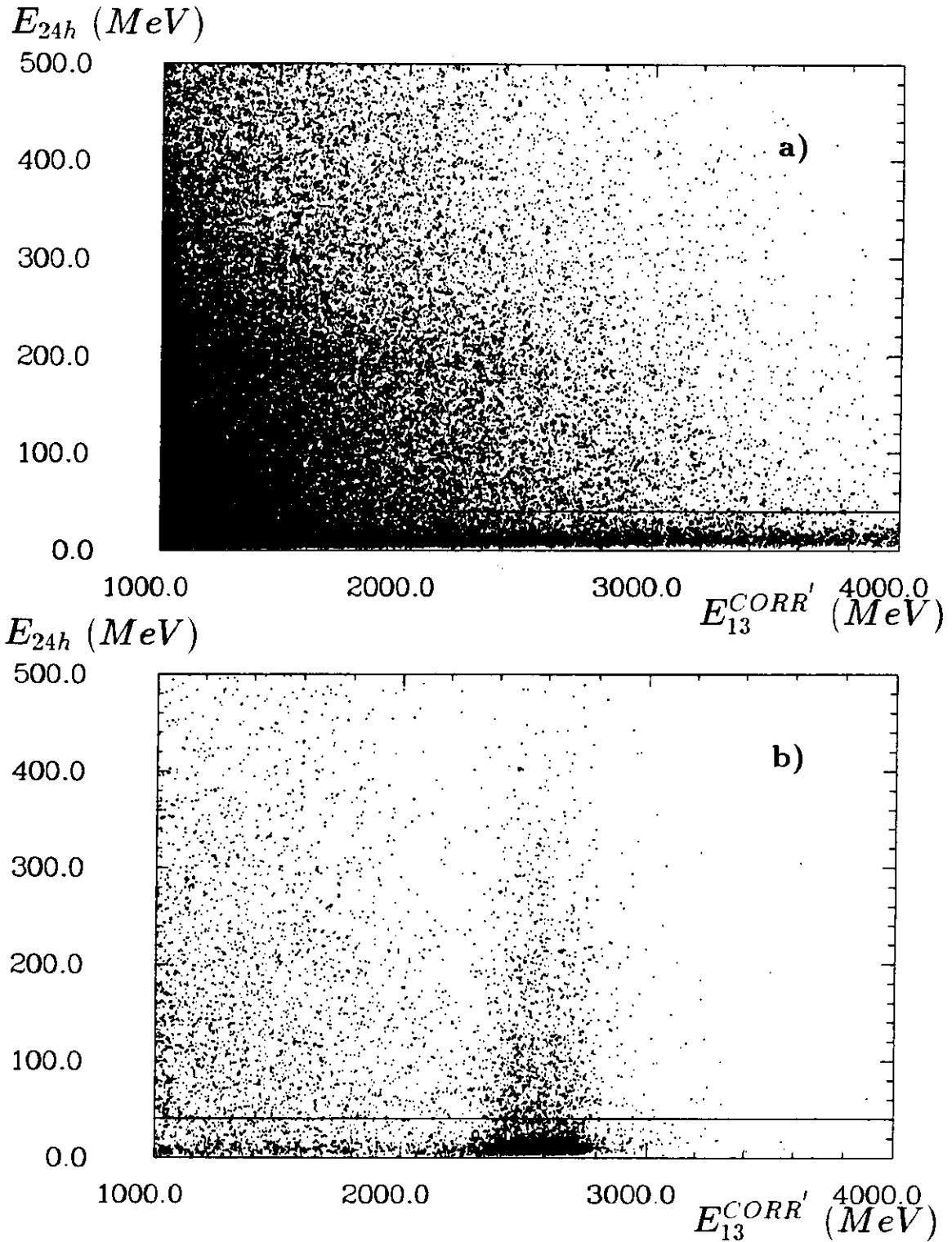
Figure 5.3: Scatter plots of the energy E_{24h} versus the energy $E_{13}^{CORR'}$ for photon candidates for (a) ON $\Upsilon(4S)$ data and (b) the Monte Carlo sample simulating the process $\Upsilon(4S) \to B\overline{B}, B \to K^*(892)\gamma$. The plots were obtained before applying the cut on E_{24h} for candidates which satisfied all the requirements listed before this cut. We accept candidates below the horizontal line.
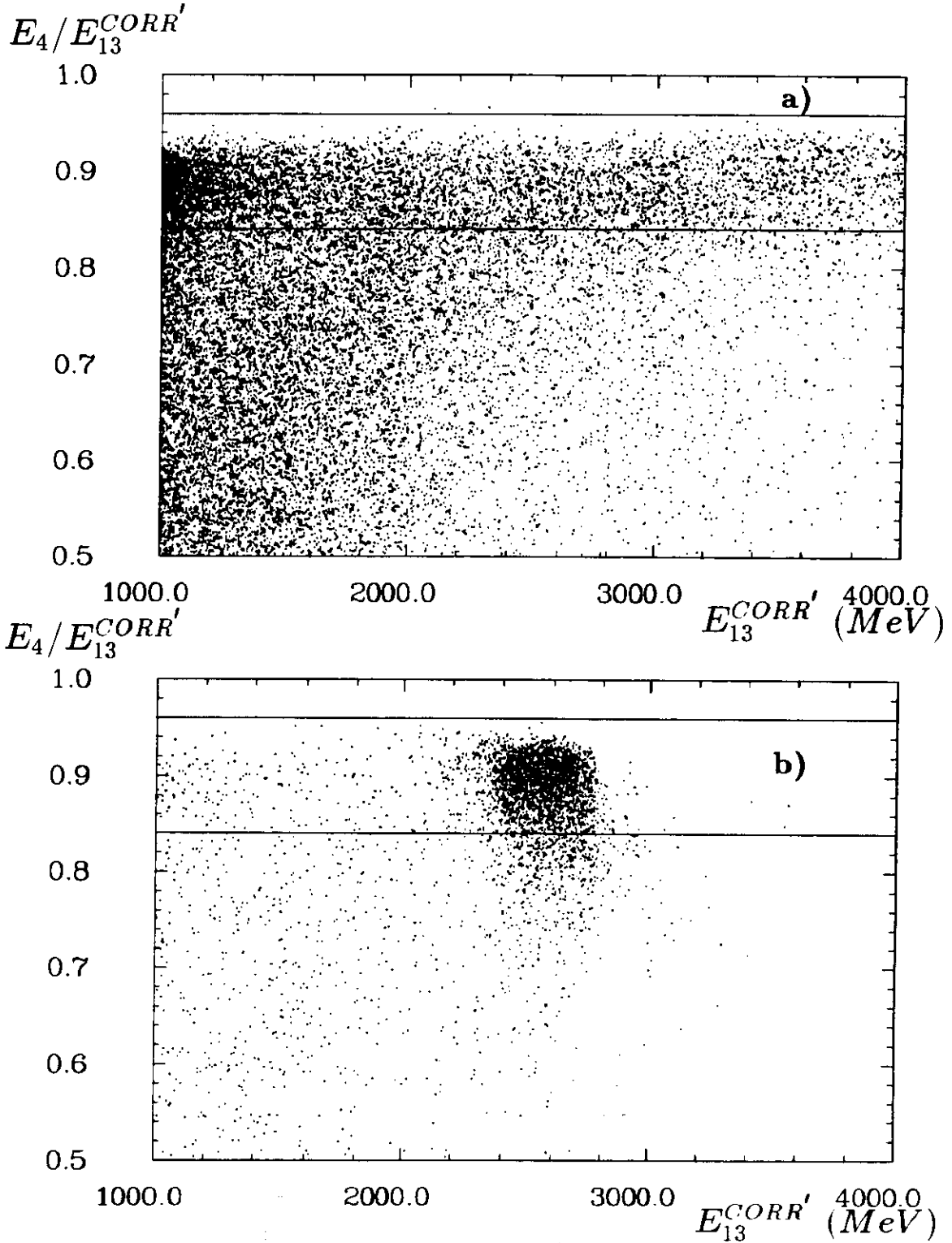
Figure 5.4: Scatter plots of the energy ratio $E_4/E_{13}^{CORR'}$ versus the energy $E_{13}^{CORR'}$ for photon candidates for (a) ON $\Upsilon(4S)$ data and (b) the Monte Carlo sample simulating the process $\Upsilon(4S) \rightarrow B\overline{B}, B \rightarrow K^*(892)\gamma$. The plots were obtained before applying the cut on $E_4/E_{13}^{CORR'}$ for candidates which satisfied all the requirements listed before this cut. We accept candidates between horizontal lines.
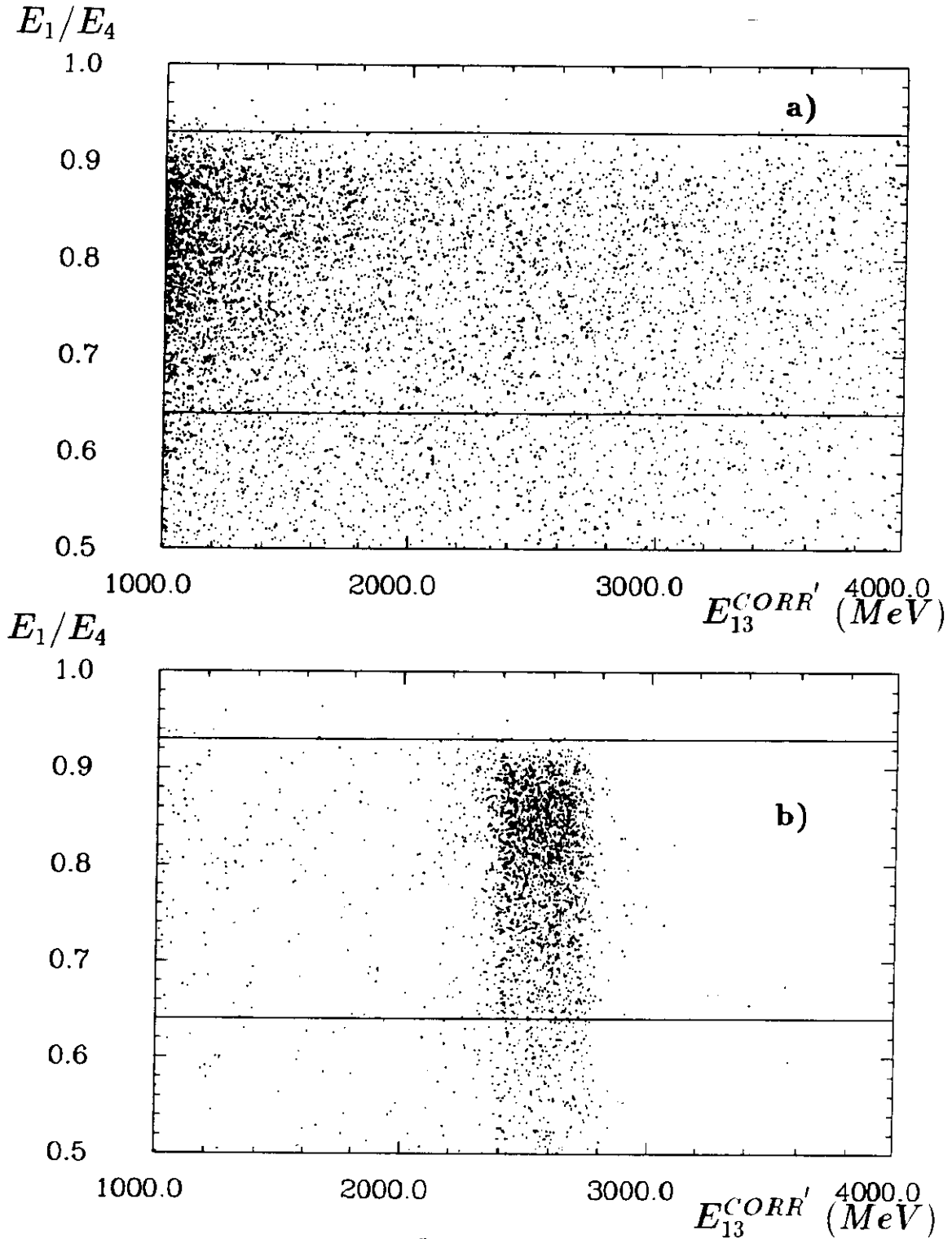
Figure 5.5: Scatter plots of the energy ratio E_1/E_4 versus the energy $E_{13}^{CORR'}$ for photon candidates for (a) ON $\Upsilon(4S)$ data and (b) the Monte Carlo sample simulating the process $\Upsilon(4S) \rightarrow B\overline{B}, B \rightarrow K^*(892)\gamma$. The plots were obtained before applying the cut on E_1/E_4 for candidates which satisfied all the requirements listed before this cut. We accept candidates between horizontal lines.
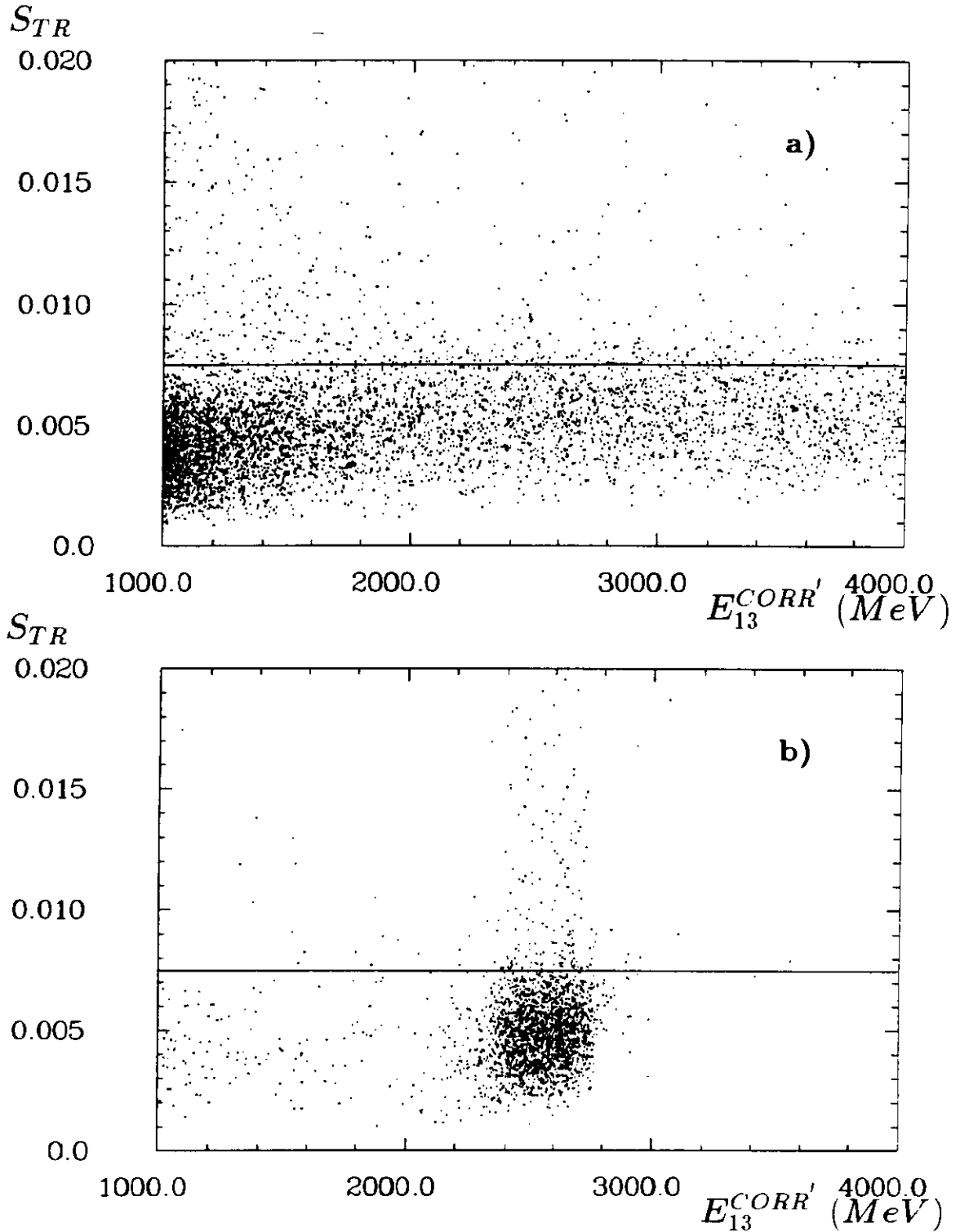
Figure 5.6: Scatter plots of the second moment of the lateral energy S_{TR} versus the energy $E_{13}^{CORR'}$ for photon canddates for (a) ON $\Upsilon(4S)$ data and (b) the Monte Carlo sample simulating the process $\Upsilon(4S) \rightarrow B\overline{B}, B \rightarrow K^*(892)\gamma$. The plots were obtained before applying the cut on S_{TR} for candidates which satisfied all the requirements listed before this cut. We accept candidates below the horizontal line.

scatter plots of E_{24h} versus the energy $E_{13}^{CORR'}$ for photon candidates for ON $\Upsilon(4S)$ data and for the Monte Carlo sample simulating the process $\Upsilon(4S) \to B\overline{B}, B \to K^*(892)\gamma$.

In order to distinguish electromagnetically showering particles from hadrons we apply two cuts on the energy ratios describing the lateral pattern of the particle energy deposition in the Main Ball (so-called 'pattern cuts' described in Appendix C):

- $0.84 < E_4/E_{13}^{CORR'} < 0.96$.

- $0.64 < E_1/E_4 < 0.93$.

The energies E_1 and E_4 were defined in Fig. 4.1. Plots of $E_4/E_{13}^{CORR'}$ and E_1/E_4 versus the energy $E_{13}^{CORR'}$ for photon candidates from ON $\Upsilon(4S)$ data and for the Monte Carlo sample simulating the process $\Upsilon(4S) \to B\overline{B}, B \to K^*(892)\gamma$ are shown in figures 5.4 and 5.5.

The cut on the second moment of the lateral energy distribution S_{TR} defined in Appendix C is intended to suppress the π° background. We demand:

- $S_{TR} < 0.0075$.

As described in Appendix C two photons from the decay of a π° with energy above 1 GeV tend to overlap and produce one energy cluster with one or two bumps. The energy deposition of such π°'s is of more oval shape (bigger S_{TR}) than in case of the almost radially symmetrical deposit of single photons. The plots of the second moment of the lateral energy versus the energy $E_{13}^{CORR'}$ for photon candidates for ON $\Upsilon(4S)$ data and for the Monte Carlo sample simulating the process $\Upsilon(4S) \to B\overline{B}, B \to K^*(892)\gamma$ are shown in Fig. 5.6.

The inclusive photon spectrum for the ON $\Upsilon(4S)$ and the continuum data samples after all cuts is shown in Fig. 5.7. The spectrum from $B\overline{B}$ events, i.e. after subtraction of the continuum contribution from ON $\Upsilon(4S)$ events, is presented (Fig. 5.8). To check our procedure, we calculate the total number of photons in the inclusive spectrum from $B\overline{B}$ events in the energy range above 2.7 GeV (see Fig. 5.8), i.e. above the kinematical limit for photons from B meson decay. This results in (8 ± 54) photons which shows that the subtraction has been done correctly. The excess of photons from other B meson decays is significant only below photon energies of 1.5 GeV. Unfortunately no evidence for any signal of monochromatic photon line could be found. In order to calculate an upper limit we have to determine the efficiency of our hardware and software selection for the relevant exclusive decay modes $B \to K^*\gamma$ (see below).

5.2.3 Efficiency of the selection of hadronic events

The efficiency for the selection of multi-hadron events is estimated by simulating $\Upsilon(4S)$ decays according to the reaction

$$e^-e^- \to \Upsilon(4S) \to B\overline{B} \to hadrons \tag{5.2}$$

using the standard LUND string fragmentation model (version 6.1) [45]. The generated events were then reconstructed with our standard software described in Chapter 4 and subjected to the same cuts as real data. The details concerning the Monte Carlo techniques in the Crystal Ball experiment are collected in Appendix D. The efficiency of the selection of multi-hadron events was found to be

$$\epsilon_{had} = (92.0 \pm 0.5 \pm 0.9)\%, \tag{5.3}$$

where the first error is statistical one and the second, systematic error is due to variations using different fragmentation models.

40

$(dN/d\ln(E_{13}^{CORR'}))/0.03$

250.0

200.0

150.0

100.0

50.0

0.0

1100   1500   2000 2500   3000   4000

$E_{13}^{CORR'}$ (MeV)
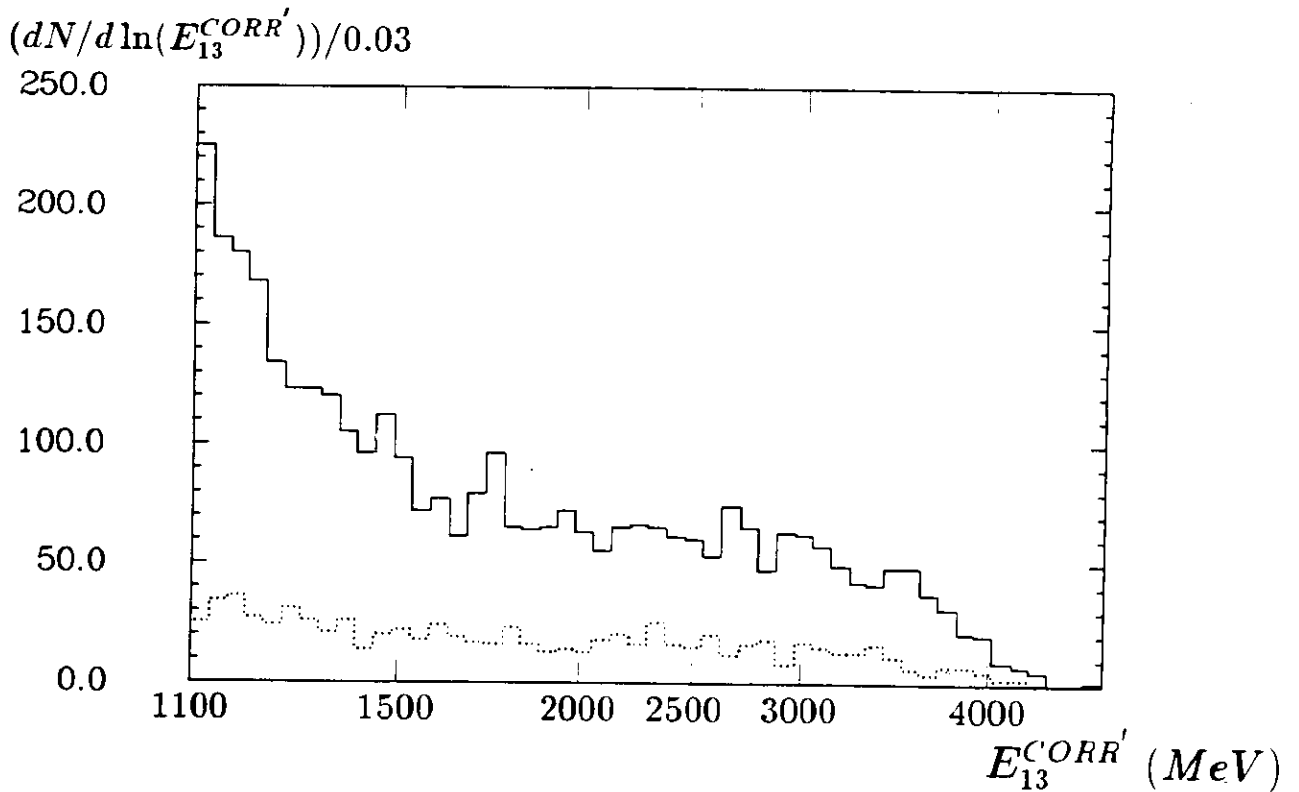
Figure 5.7: Inclusive spectrum of photons from the ON $\Upsilon(4S)$ (solid histogram) and the continuum (dotted histogram) data samples. The luminosity ratio r_{lum} is 4.025.

$(dN/d\ln(E_{13}^{CORR'}))/0.03$

100.0

possible photons from B decays $\leftarrow$ | $\rightarrow$ photons which cannot come from B decays

| $\rightarrow$ expected signal $\leftarrow$ | region

50.0

0.0

-50.0

E_γ : 1850   2725 MeV
m_X : 2900   892 MeV

-100.0

1100   1500   2000 2500   3000   4000

$E_{13}^{CORR'}$ (MeV)
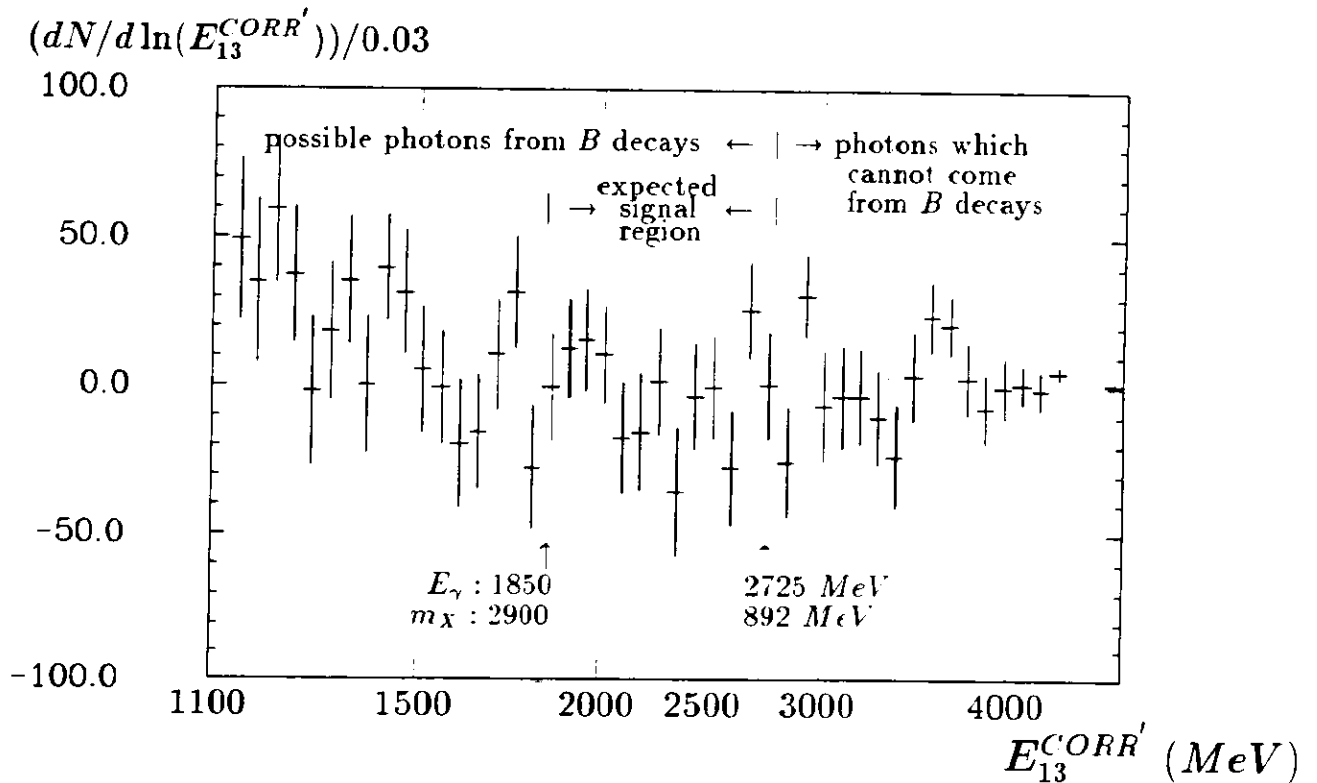
Figure 5.8: The inclusive photon spectrum from $B\overline{B}$ events (after the subtraction of the continuum contribution from the ON $\Upsilon(4S)$ events). The boundaries of the 'signal region' in which we search for photons from the decay $B \rightarrow \gamma X$ are also shown.

41

$(dN/d\ln(E_{13}^{CORR'}))/0.05$
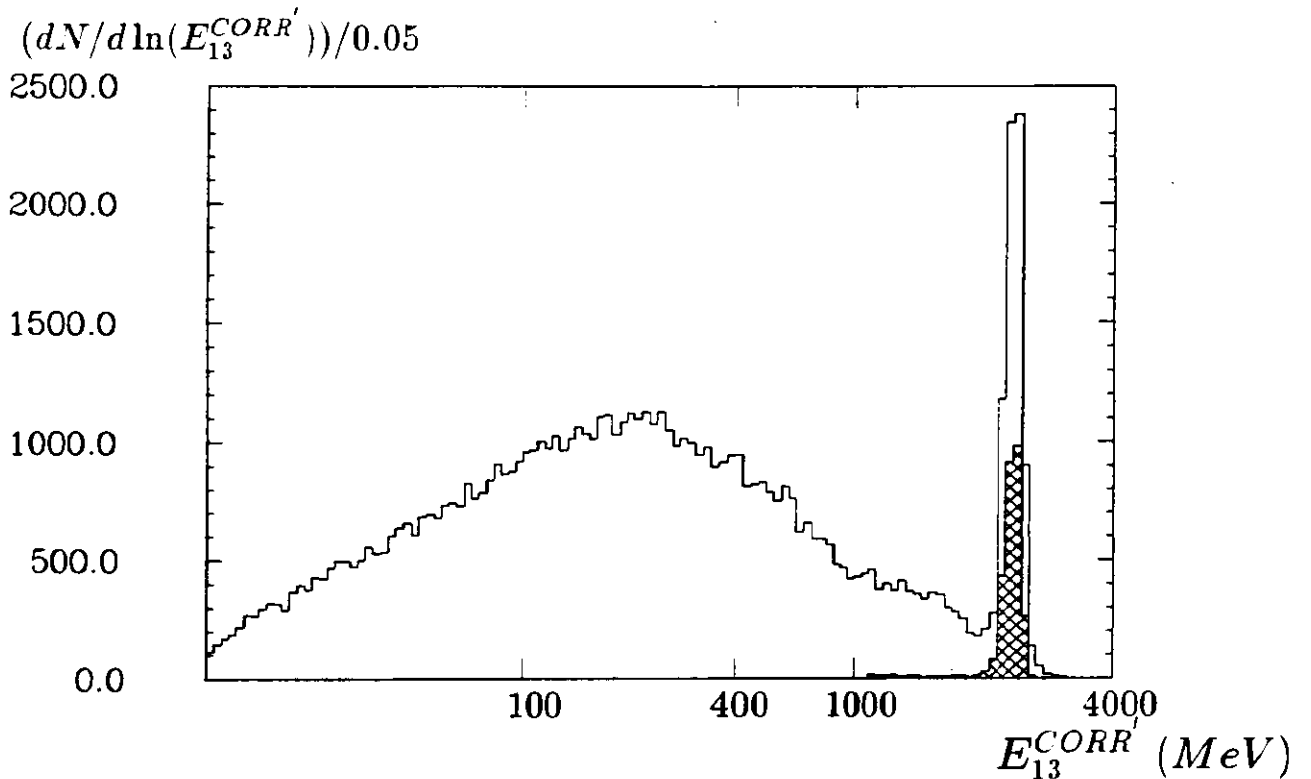
Figure 5.9: Energy spectrum of all neutral particles from the Monte Carlo sample simulating the process $\Upsilon(4S) \rightarrow B\bar{B}, B \rightarrow K^*(892)\gamma$ (solid histogram). Photons selected as described in the text are also shown (double-hatched histogram).

5.2.4 Efficiency of photon selection

In order to estimate the photon detection efficiency we use the same LUND program to simulate the $\Upsilon(4S)$ meson decays at rest into $B\bar{B}$ pairs. In each simulated event exactly one $B(\bar{B})$ meson decays further into one of the K^* states and a high-energy (about 2.5 GeV) photon. The angular distribution of this decay was assumed to be described by the phase space. The decays of the other B meson were simulated using the branching fractions for various decay modes listed in Table D.1 of Appendix D. We concentrated on four FCNC decay channels: $B \rightarrow K^*(892)\gamma$, $B \rightarrow K_1(1400)\gamma$, $B \rightarrow K_2(1770)\gamma$ and $B \rightarrow K_4^*(2045)\gamma$. Fig. 5.9 shows the energy spectrum of neutral particles for the Monte Carlo sample simulating the process $\Upsilon(4S) \rightarrow B\bar{B}, B \rightarrow K^*(892)\gamma$. The efficiency of photon selection is defined as the ratio of the number of selected photons to the number of generated events. We obtain the following values:

$$\epsilon_\gamma^{K^*(892)} = (13.5 \pm 0.4 \pm 0.8)\% \qquad (5.4)$$

$$\epsilon_\gamma^{K_1(1400)} = (17.0 \pm 0.6 \pm 0.8)\% \qquad (5.5)$$

$$\epsilon_\gamma^{K_2(1770)} = (20.4 \pm 0.6 \pm 0.8)\% \qquad (5.6)$$

$$\epsilon_\gamma^{K_4^*(2045)} = (20.3 \pm 0.6 \pm 0.8)\%, \qquad (5.7)$$

where the first error is statistical and the second systematic one. The latter includes systematic uncertainty in branching fractions for B meson decays simulated in the LUND program (0.6%) and the uncertainty in the choice of the fragmentation function applied in the program of 0.4% (as a measure of this error we take the difference in efficiencies between the string and Feynman-Field fragmentation functions). For the mode $B \rightarrow K^*(892)\gamma$ we studied by Monte Carlo the

42

difference in the efficiencies between neutral and charged B meson decays (0.3%). The increase of the efficiency with the mass of the K^* state, used in the simulation of the decay $B \to K^*\gamma$, is mainly due to the cut on the second Fox-Wolfram moment $H2$. For higher masses of the K^* state, the topology of the event is more symmetrical (smaller values of $H2$) as the K^* decays into more particles and at the same time the photon energy becomes smaller.

5.2.5 Determination of the upper limit for the process $b \to s\gamma$

Our present task is to estimate the upper limit on the branching fraction for the process $b \to s\gamma$. First we calculate the total number of photons from $B\overline{B}$ events in the energy range where photons from the decay under investigation may occur (see Fig. 5.8). This range spreads up to photon energies of 2700 MeV, which corresponds to the highest possible energy of photons from the decay $B \to K^*(892)\gamma$, taking into account the Doppler shift and the energy resolution of our detector. The lowest value of photon energy was set to 1850 MeV. This is motivated by the fact that below this energy the background of photons from other B meson decays becomes substantial (Fig. 5.8). In case of the process $B \to \gamma X$ this corresponds to the recoil mass m_X of 2900 MeV. Therefore we are looking for photons coming from the process $B \to \gamma X$, where by X we understand any hadron state in the mass range between 892 MeV and 2900 MeV. Assuming that only states containing non-zero strangeness contribute here we can refer our estimate to the process $b \to s\gamma$. The presence of non-strange states e.g. those with charm would lead to overestimation of our upper limit i.e. the real upper limit for $b \to s\gamma$ would be lower than that determined by us.

The efficiency of selection of photons from the decays $B \to K^*\gamma$ evaluated for four different modes in the previous section depends on the photon energy (or, equivalently, on the recoil mass). Therefore in the region defined above we corrected the number of photons for the efficiency of their selection in each bin of the inclusive photon spectrum. We assumed that possible photons with energy from 2700 MeV to 2500 MeV are detected with the efficiency $\epsilon_\gamma^{K^*(892)}$ (Fig. 5.10) as most of them come from the decay $B \to K^*(892)\gamma$. In the same way the next two efficiency values, namely $\epsilon_\gamma^{K_1(1400)}$ and $\epsilon_\gamma^{K_2(1770)}$ are associated to the ranges (2500–2420) MeV and (2420–2300) MeV, respectively. For the rest of the range i.e. for photon energies from 2300 MeV to 1850 MeV (recoil masses from 1950 MeV to 2900 MeV) we assumed the efficiency $\epsilon_\gamma^{K_4^*(2045)}$.

We claim that in this way we are possibly underestimating the efficiency which leads to a conservative upper limit. As we mentioned before the increase of the efficiency for the selection of photons from the decays $B \to K^*\gamma$ with the recoil mass in the range from 892 MeV to 1770 MeV is caused by the cut on the event topology i.e. on the second Fox-Wolfram moment $H2$. For the masses of the K^* states bigger than 1770 MeV our events become more spherical and their topology is very similar for different K^* modes as it was studied by comparing the $H2$ distributions for $B \to K_2(1770)\gamma$ and $B \to K_4^*(2045)\gamma$ modes. Therefore our extrapolation of the constant efficiency above the recoil mass of 2045 MeV is justified.

The total number of photons in the energy range from 2700 MeV to 1850 MeV (Fig. 5.10) is then:

$$N_\gamma = -167 \pm 370. \tag{5.8}$$

which corresponds to the following 90% C.L. upper limit on N_γ

$$N_\gamma^{UL} = 516. \tag{5.9}$$

43

N_γ/ϵ_γ
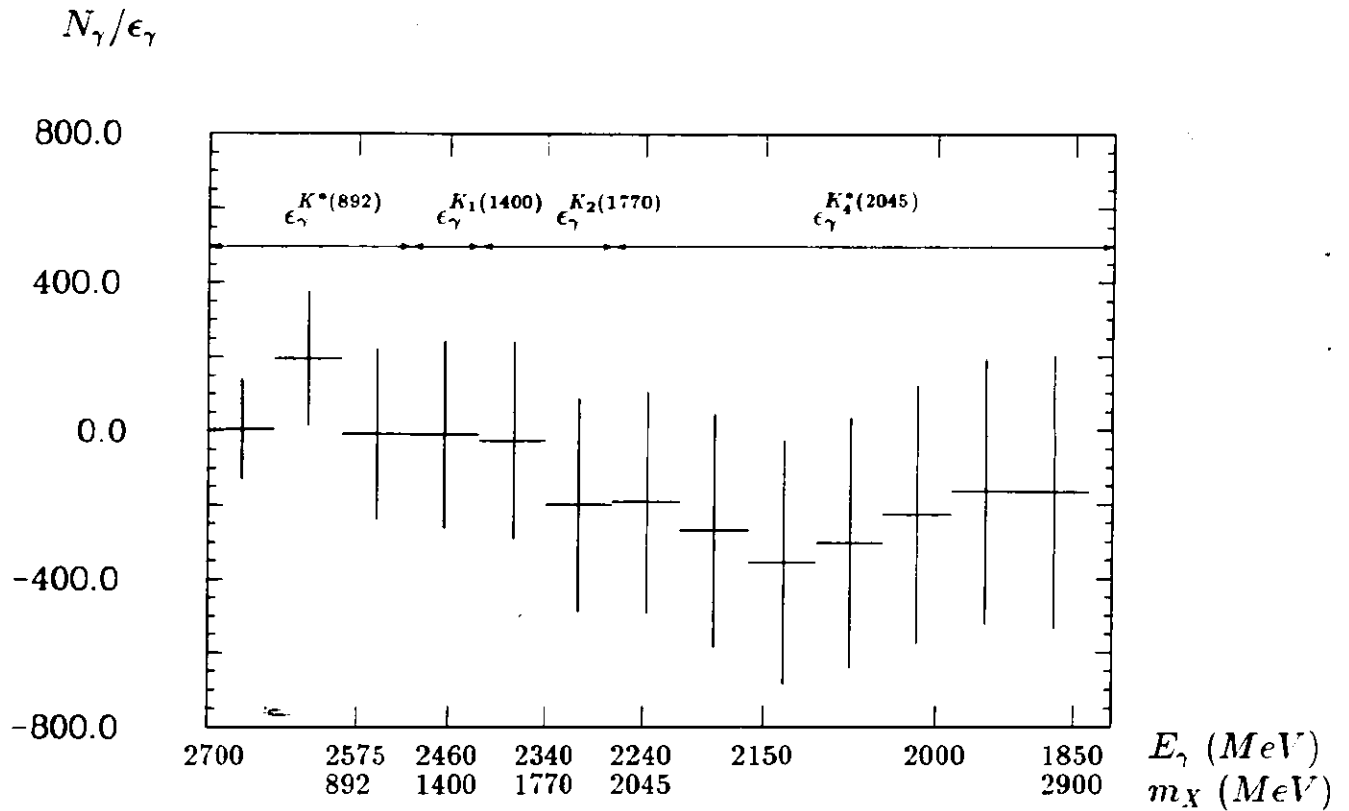
Figure 5.10: The total number of photons (corrected for efficiency of their selection) from the process $B \rightarrow \gamma X$ versus the lowest value of photon energy (or, equivalently, the highest value of the recoil mass m_X), for which the summation of the number of photons was performed.

$(dN/d\cos\alpha)/0.01$
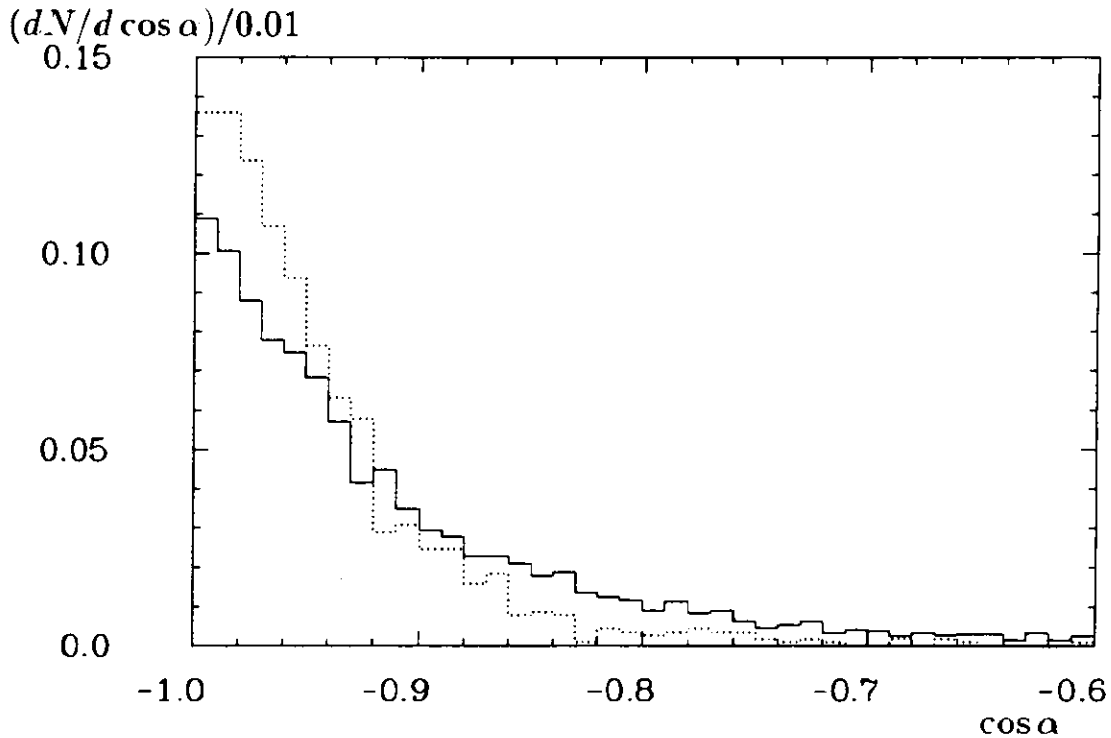
Figure 5.11: The distributions (normalized to the same area) of the angle between photon and the 'opposite' particle for ON $\Upsilon(4S)$ data (solid histogram) and a Monte Carlo simulation of the decay chain $\Upsilon(4S) \rightarrow B\overline{B}, B \rightarrow K_4^*(2045)\gamma$ (dotted histogram).

The 90% C.L. upper limit on the branching fraction for the decay $b \rightarrow s\gamma$ is evaluated according to the formula [46]:

$$BR(b \rightarrow s\gamma) < \frac{N_\gamma^{UL}(1 + 1.28\sigma_{rel})}{2N_{B\overline{B}}^{vis}/\epsilon_{had}} < 4.1 \times 10^{-3}, \tag{5.10}$$

where σ_{rel} denotes the relative error of the factor $2N_{B\overline{B}}^{vis}/\epsilon_{had}$ with the individual contributions added in quadrature. The factor $(1 + 1.28\sigma_{rel})$ converts this quotient into an upper limit at 90% confidence level. The discussion of this result will be presented in Chapter 6.

5.2.6 Determination of upper limits for the decays $B \rightarrow K^*\gamma$

We search for the decays $B \rightarrow K^*\gamma$ in two ways i.e. by the investigation of the inclusive photon spectrum and by studying the distribution of the cosine of the angle between a high-energy photon and the 'opposite' particle (particle emitted at the largest angle with respect to the photon). In Fig. 5.11 we present this angular distribution for ON $\Upsilon(4S)$ data and for a Monte Carlo simulation of the process $\Upsilon(4S) \rightarrow B\overline{B}, B \rightarrow K_4^*(2045)\gamma$. The Monte Carlo distribution is more sharply peaked towards $\cos\alpha = -1$ than the data. The difference is more pronounced for the lower mass K^* states. This shows that the angular distribution can also be used for the selection of $K^*\gamma$ decays.

We estimate upper limits on the number of photons originating from the exclusive decays using a procedure based on the method of maximum likelihood [46] which is common in both approaches. The detailed description is given for the fit to the inclusive photon spectrum. The ON $\Upsilon(4S)$ and the continuum data were fitted simultaneously. The likelihood function is defined as

$$\mathcal{L} = \mathcal{L}_{ON}(Y, N) \times \mathcal{L}_{CONT}(V, M) \times \mathcal{L}_{lum}$$

$$= (\prod_i^{N_{bins}} \frac{Y_i^{N_i} \cdot \exp(-Y_i)}{N_i!}) \times (\prod_k^{N_{bins}} \frac{V_k^{M_k} \cdot \exp(-V_k)}{M_k!}) \times (\exp(-\frac{(R - r_{lum})^2}{2\sigma_{r_{lum}}^2})), \tag{5.11}$$

where:

N_{bins} — number of bins used in the fit

E_i — mean energy in the i-th bin

N_i — number of selected ON $\Upsilon(4S)$ photons in the i-th bin

$Y_i = Y_i^b + Y_i^s$ — number of fitted ON $\Upsilon(4S)$ photons in the i-th bin

Y_i^s — number of fitted ON $\Upsilon(4S)$ signal photons in the i-th bin

Y_i^b — number of fitted ON $\Upsilon(4S)$ background photons in the i-th bin

M_k — number of selected continuum photons in the k-th bin

V_k — number of fitted continuum photons in the k-th bin

r_{lum} — luminosity ratio factor (4.025)

$\sigma_{r_{lum}}$ — error on the luminosity ratio factor (0.009)

R — fit parameter corresponding to the luminosity ratio.

Here the first and second factors represent the likelihoods for the ON $\Upsilon(4S)$ and the continuum data (Poisson error distribution is assumed). The number of fitted background events in the ON $\Upsilon(4S)$ spectrum was constrained (by the third factor in the likelihood function) to

be equal to the fitted continuum contribution multiplied by the luminosity ratio factor (see Chapter 4). The strength of this constraint is given by $\sigma_{r_{lum}}$, the error on the luminosity ratio. The fit results gave R within one standard deviation of r_{lum}. The binning of the fitted spectra is logarithmic with bin width of 3%. This results in an appproximately constant energy resolution per bin in the relevant energy range. The fit window covers 30 bins and spreads from 1450 MeV to 3680 MeV. We use wider range then in search for the inclusive process $b \rightarrow s\gamma$ in order to reduce the errors coming from the subtraction of the continuum.

The background is parametrized as the sum of a constant and linear contribution. The parametrization is as follows:

$$Y_i = Y_i^b + Y_i^s = R \times (N_0 + N_1 \times \ln E_i) + N_\gamma \times F_B \ln E_i$$
$$V_k = N_0 + N_1 \times \ln E_k. \qquad (5.12)$$

with four parameters: N_0, N_1, R and N_γ to be determined by the fit. The number of degrees of freedom for the fit $NDF = 56$ (2×30 bins of data and 4 parameters to be fitted).

F_B is a 'bell' function used for a parametrization of the expected signal (see Appendix E and Table E.1). We have checked that our results are not sensitive whether we use the bell or Gaussian parametrization of the signal.

The goodness of the fit is calculated according to S. Baker and R.D. Cousins [47] as:

$$\chi^2 = -2\ln(\frac{\mathcal{L}_{ON}(Y, N)}{\mathcal{L}_{ON}(N, N)}) = 2 \sum_{i=1}^{N_{bins}} (Y_i - N_i + N_i \ln \frac{N_i}{Y_i}). \qquad (5.13)$$

The denominator $\mathcal{L}_{ON}(N, N)$ is the normalization to guarantee that χ^2 is zero if $Y_i = N_i$ in all bins.

We minimize $-\ln(\text{likelihood})$ using the MINUIT [48] program. Two examples of the fits are shown in Fig. 5.12 and 5.13. The numbers of photons N_γ obtained from the fits are listed in Table 5.1. As the fits do not give any signal for the decays $B \rightarrow K^*\gamma$ we convert their results to the 90% C.L. upper limits on the number of photons (N_γ^{UL} in Table 5.1). This conversion is obtained by integrating the likelihood function over the positive range of the signal amplitude N_γ.

A similar fit is performed for the distribution of the cosine of the angle α between the photon selected in the desired energy range and the 'opposite' particle i.e. the particle with the largest opening angle with respect to the photon. The expected signal is parametrized as a Gaussian function centered at $\alpha = 180°$ and with a width estimated from the Monte Carlo events simulating $B \rightarrow K^*\gamma$ decays (Table E.2 in Appendix E). The background is described by the sum of contributions from constant and quadratic terms. Our parametrization is as follows:

$$Y_i = Y_i(\cos^2 \alpha_i) = Y_i^b(\cos^2 \alpha_i) + Y_i^s(\cos^2 \alpha_i) = R \times (N_0 + N_2 \times \cos^2 \alpha_i) - N_\gamma \times F_G(\cos^2 \alpha_i)$$
$$V_k = V_k(\cos^2 \alpha_k) = N_0 + N_2 \times \cos^2 \alpha_k. \qquad (5.14)$$

Four parameters N_0, N_2, R and N_γ are determined by the fit. Two examples of the fits are shown in Fig. 5.14 and 5.15. Their results are presented in Table 5.2.

So far we considered two methods of search for the decays $B \rightarrow K^*\gamma$ i.e. the investigation of the inclusive photon spectrum ('Method I') and of the distribution of the cosine of the angle α between photon and the 'opposite' particle ('Method II'). In order to obtain a better discrimination between $B \rightarrow K^*\gamma$ decays and the other B decays or continuum events we make

$(dN/d\ln(E_{13}^{CORR'}))/0.03$
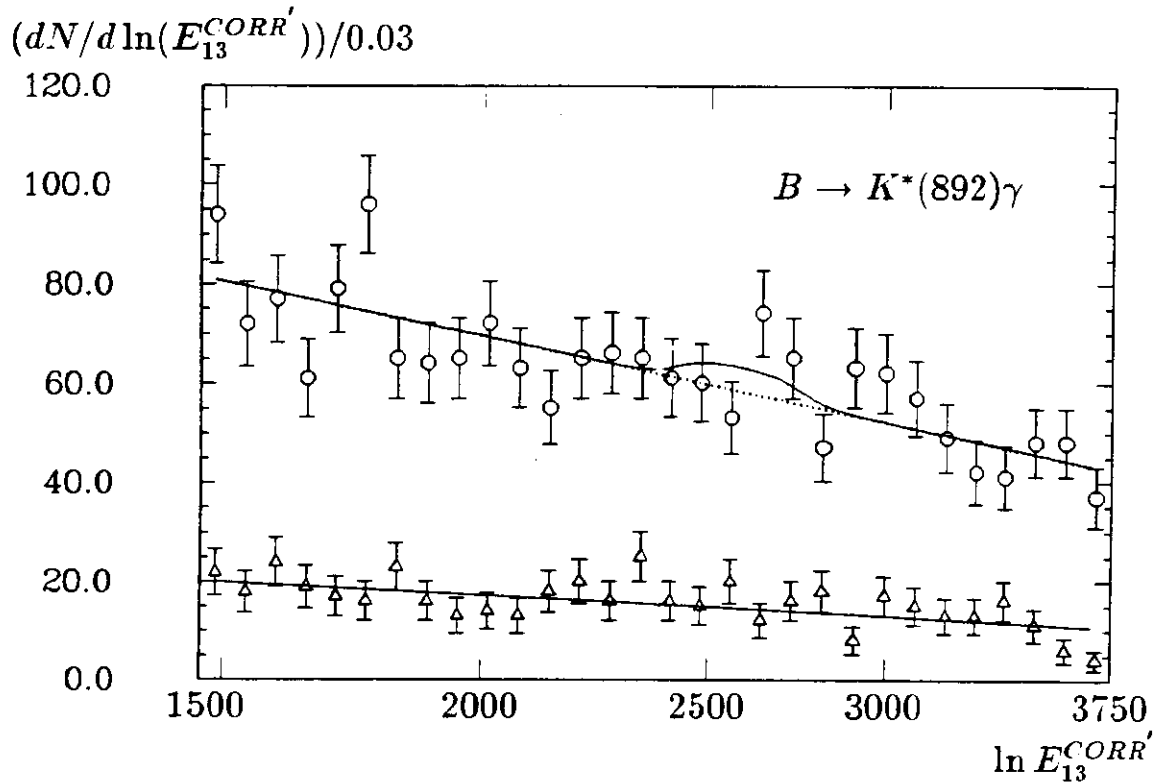
Figure 5.12: The fit (solid line) to the inclusive photon spectrum for ON $\Upsilon(4S)$ (circles) and continuum (triangles) photons in search for the $B \to K^*(892)\gamma$ decay. The area between the solid and dotted line (contribution from the background) corresponds to the fitted signal.

$(dN/d\ln(E_{13}^{CORR'}))/0.03$
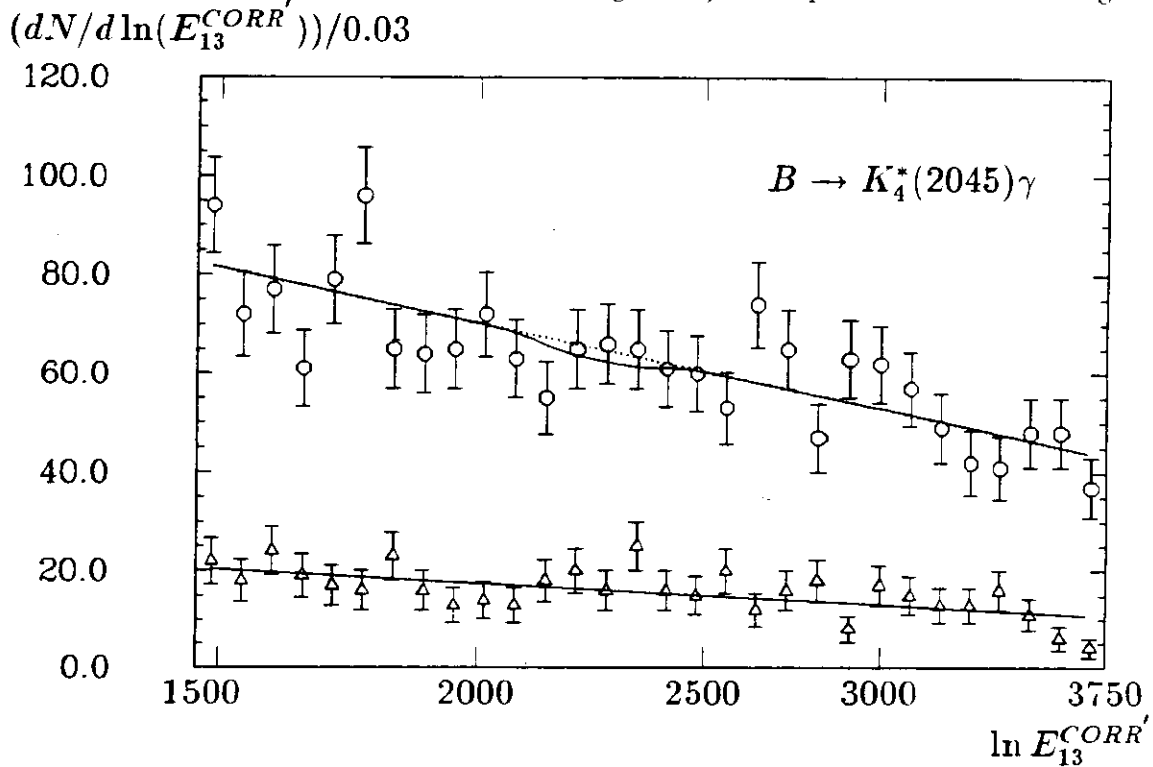
Figure 5.13: The fit (solid line) to the inclusive photon spectrum for ON $\Upsilon(4S)$ (circles) and continuum (triangles) photons in search for $B \to K_4^*(2045)\gamma$ decay. The area between the solid and dotted line (contribution from the background) corresponds to the fitted signal.
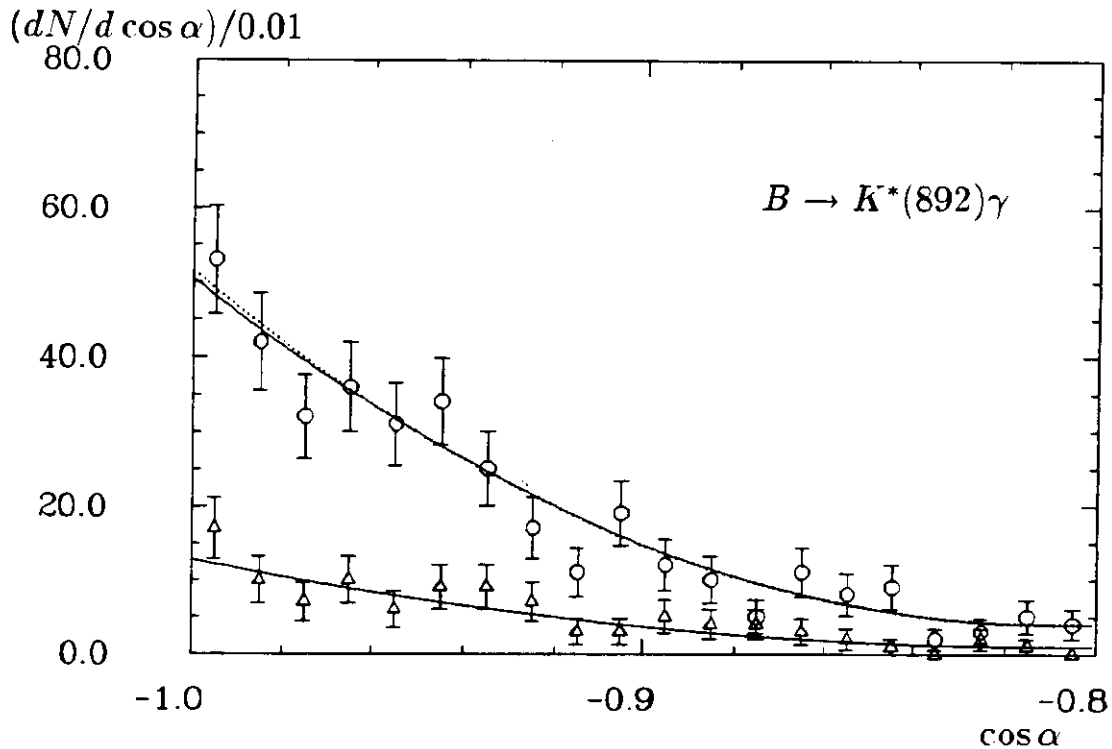
Figure 5.14: The fit (solid line) to the distribution of the cosine of the angle α between photon and the 'opposite' particle for ON $\Upsilon(4S)$ (circles) and continuum (triangles) photons with energies expected for the $B \to K^*(892)\gamma$ decay. The area between the solid and dotted line (contribution from the background) corresponds to the fitted signal.
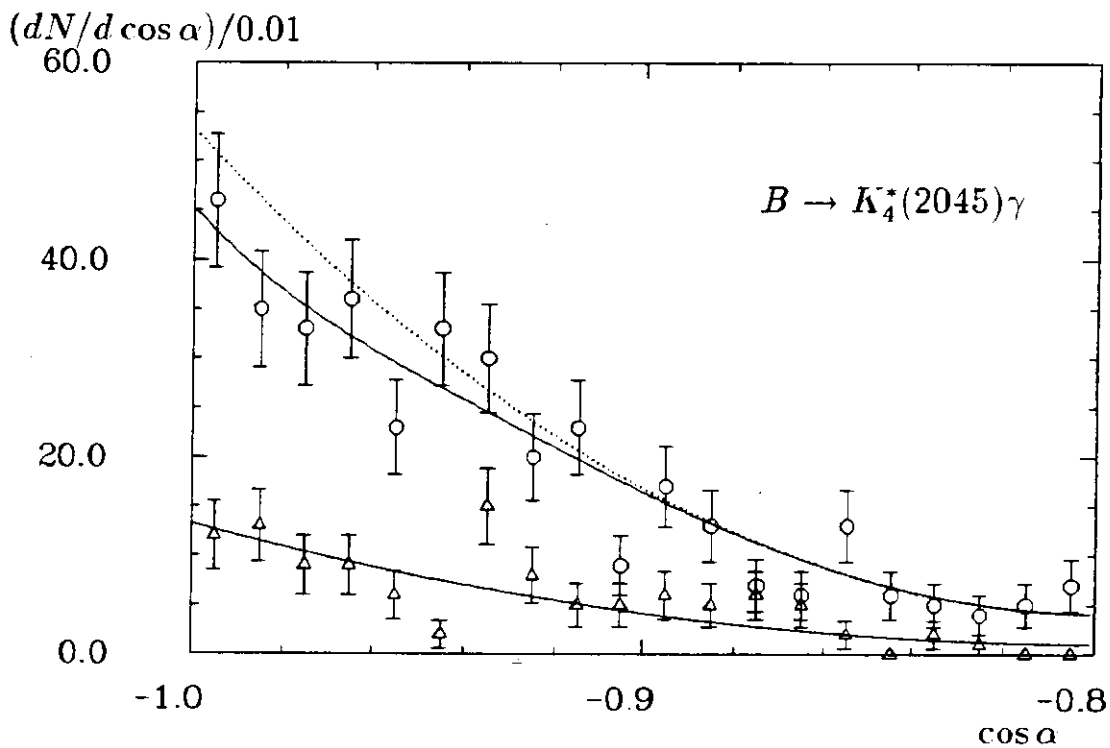
Figure 5.15: The fit (solid line) to the distribution of the cosine of the angle α between photon and the 'opposite' particle for ON $\Upsilon(4S)$ (circles) and continuum (triangles) photons with energies expected for the $B \to K_4^*(2045)\gamma$ decay. The area between the solid and dotted line (contribution from the background) corresponds to the fitted signal.

48

joint fits to the photon spectrum and the $\cos \alpha$ distribution for each K^* state. The likelihood function is now the product of five factors:

$$\mathcal{L} = \mathcal{L}_{ON}^{\overline{I}} \times \mathcal{L}_{CONT}^{I} \times \mathcal{L}_{ON}^{II} \times \mathcal{L}_{CONT}^{II} \times \mathcal{L}_{lum} \tag{5.15}$$

with the same parametrization as described before. The results of the fits are presented in Table 5.3.

Systematic errors in the upper limits on the number of photons originating from the decays $B \to K^*\gamma$ resulting from the fits to the inclusive photon spectrum have been studied by:

- varying selection cuts (up to 15% of values of cut parameters presented above),

- changing the fit range by one bin,

- shifting the binning to the left by a half of a bin,

- changing the signal parametrization from the bell to the Gaussian distribution (Table E.1 in Appendix E).

The results of the estimation are collected in Table 5.4. Uncertainties from the individual sources are summed in quadrature.

In case of the fits to the distribution of the cosine of the angle between photon and the 'opposite' particle we estimate the systematic uncertainties by (Table 5.5):

- changing selection cuts (up to 15% of values of cut parameters presented above),

- narrowing the range of energies of photons taken to the fit by 10%,

- changing the binning from 0.01 to 0.0125,

- varying the width (inside its error) of the Gaussian distribution used as a signal parametrization (Table E.2 in Appendix E).

The uncertainties are added in quadrature to obtain total systematic errors on the upper limits on the number of photons from the relevant decays.

In case of the joint fits to the inclusive photon spectrum and to the distribution of the cosine of the angle between photon and the 'opposite' particle we estimate systematic effects by investigating separatively each individual contribution from both methods (Table 5.6).

We calculate the 90% C.L. upper limits on branching fractions for the decays $B \to K^*\gamma$ from the formula [46]:

$$BR(B \to K^*\gamma) < \frac{N_\gamma^{UL}/\epsilon_\gamma^{K^*}(1 + 1.28\sigma_{rel}^{stat})}{2N_{B\overline{B}}^{vis}/\epsilon_{had}}, \tag{5.16}$$

where σ_{rel}^{stat} denotes the relative statistical error of the factor $(2N_{B\overline{B}}^{vis}/\epsilon_{had})\epsilon_\gamma^{K^*}$ with the individual contributions added in quadrature. The factor $(1 + 1.28\sigma_{rel}^{stat})$ converts this expression into an upper limit at 90% confidence level. The relative systematic errors in efficiencies for the hadronic event selection, for photon selection and the systematic uncertainties in the calculation of the upper limit on the number of signal events originating from the fit procedure were summed in quadrature resulting in the relative systematic error σ_{rel}^{sys} of the estimation of the upper limit for the branching fraction on the decays $B \to K^*\gamma$. These errors have been added linearly to the result obtained according to formula 5.16 by multiplying it by the factor $(1 + \sigma_{rel}^{sys})$. Our results obtained from the fits to the inclusive photon spectrum, from the fits to the cosine of the angle between the selected photon and the 'opposite' particle and from joint fits to both spectra are collected in Tables 5.1, 5.2 and 5.3. respectively. They are discussed in Chapter 6.

49

Table 5.1: 90% C.L. upper limits on $BR(B \to K^*\gamma)$ obtained from the fits to the inclusive photon spectrum.

Decay mode	Number of photons N_γ	N_γ^{UL} 90% C.L.	Systematic error on N_γ^{UL}	BR^{UL} 90% C.L.	χ^2/NDF
$B \to K^*(892)\gamma$	$19.7^{+19.8}_{-19.2}$	45	5.4	3.0×10^{-3}	60/56
$B \to K_1(1400)\gamma$	$4.6^{+20.2}_{-19.5}$	36	4.3	1.9×10^{-3}	61/56
$B \to K_2(1770)\gamma$	$-0.1^{+20.3}_{-19.6}$	33	4.0	1.5×10^{-3}	61/56
$B \to K_4^*(2045)\gamma$	$-9.5^{+19.9}_{-19.3}$	28	5.3	1.3×10^{-3}	61/56

Table 5.2: 90% C.L. upper limits on $BR(B \to K^*\gamma)$ obtained from the fits to the angular distribution photon–'opposite' particle.

Decay mode	Photon energies	Number of photons N_γ	N_γ^{UL} 90% C.L.	Systematic error on N_γ^{UL}	BR^{UL} 90% C.L.	χ^2/NDF
$B \to K^*(892)\gamma$	2320–2840	$-1.4^{+16.4}_{-15.9}$	26	4.9	1.8×10^{-3}	31/36
$B \to K_1(1400)\gamma$	2200–2690	$-18.4^{+25.7}_{-25.8}$	32	3.8	1.7×10^{-3}	33/36
$B \to K_2(1770)\gamma$	2120–2590	$-32.7^{+27.0}_{-27.1}$	28	5.9	1.3×10^{-3}	44/36
$B \to K_4^*(2045)\gamma$	2040–2490	$-49.3^{+31.8}_{-32.2}$	29	6.1	1.4×10^{-3}	49/36

Table 5.3: 90% C.L. upper limits on $BR(B \to K^*\gamma)$ obtained from the joint fits to the inclusive photon spectrum and to the distribution of cosine of the angle between photon and the 'opposite' particle.

Decay mode	Number of photons N_γ	N_γ^{UL} 90% C.L.	Systematic error on N_γ^{UL}	BR^{UL} 90% C.L.	χ^2/NDF
$B \to K^*(892)\gamma$	$8.5^{+12.5}_{-12.2}$	26	4.2	1.8×10^{-3}	93/94
$B \to K_1(1400)\gamma$	$-3.0^{+15.6}_{-15.2}$	24	4.3	1.3×10^{-3}	96/94
$B \to K_2(1770)\gamma$	$-10.2^{+15.8}_{-15.5}$	20	3.4	0.9×10^{-3}	106/94
$B \to K_4^*(2045)\gamma$	$-19.2^{+16.4}_{-16.1}$	18	3.8	0.9×10^{-3}	110/94

Table 5.4: Systematic uncertainties (in %) in the upper limit on the number of photons from the decays $B \to K^*\gamma$ resulting from the fits to the inclusive photon spectrum.

Mode	Source of systematic error				Total systematic error
	Selection cuts	Signal shape	Fit range	Binning	
$B \to K^*(892)\gamma$	3	4	9	6	12
$B \to K_1(1400)\gamma$	3	3	11	3	12
$B \to K_2(1770)\gamma$	3	3	10	9	14
$B \to K_4^*(2045)\gamma$	3	7	13	11	19

Table 5.5: Systematic uncertainties (in %) in the upper limit on the number of photons from the decays $B \to K^*\gamma$ resulting from the fits to the distribution of the cosine of the angle between photon and the 'opposite' particle. By the 'fit range' we understand here the energy range of photons for which the fit was performed.

Mode	Source of systematic error				Total systematic error
	Selection cuts	Signal shape	Fit range	Binning	
$B \to K^*(892)\gamma$	10	4	7	14	19
$B \to K_1(1400)\gamma$	10	6	3	1	12
$B \to K_2(1770)\gamma$	10	5	17	3	21
$B \to K_4^*(2045)\gamma$	10	5	18	1	21

Table 5.6: Systematic uncertainties (in %) in the upper limit on the number of photons from the decays $B \to K^*\gamma$ resulting from the joint fits to the inclusive photon spectrum ('Method I') and to the distribution of the cosine of the angle between photon and the 'opposite' particle ('Method II').

Mode	Source of systematic error							Total systematic error
	Selection cuts	Method I			Method II			
		Signal shape	Fit range	Binning	Signal shape	Fit range	Binning	
$B \to K^*(892)\gamma$	6	2	8	9	4	2	7	16
$B \to K_1(1400)\gamma$	6	4	13	1	5	7	4	18
$B \to K_2(1770)\gamma$	6	5	10	4	5	8	6	17
$B \to K_4^*(2045)\gamma$	6	3	12	10	2	11	3	21

5.3 Search for processes $B \to KJ/\psi$ and $B \to K^*J/\psi$

We present here the analysis of the missing mass spectrum with respect to the e^+e^- pair coming from the J/ψ decay. It is intended to search for the processes $B \to KJ/\psi$ and $B \to K^*J/\psi$ denoted shortly as $B \to K^{(*)}J/\psi$ where $K^{(*)}$ stands for both K and K^* states.

5.3.1 Topology of $B \to KJ/\psi$ and $B \to K^*J/\psi$ events

The general features of the topology of the $\Upsilon(4S)$ decay into a $B\bar{B}$ pair in which one of the B mesons decays to a photon and a K (K^*) meson (see section 5.2.1) are valid also for the modes $B \to KJ/\psi$ and $B \to K^*J/\psi$ where the J/ψ decays further into an e^+e^- pair ($BR(J/\psi \to e^+e^-) = (6.9 \pm 0.9)\%$). In particular $K(K^*)$ and J/ψ are emitted almost exactly in opposite directions in the laboratory frame since the B meson is very slow. The particle with the biggest opening angle with respect to the J/ψ will be called the 'opposite' one. The opening angle between e^- and e^+ is greater than $120°$ and peaks at $135°$. The electron energy distribution is almost flat and spreads from $0.9\ GeV$ to $2.7\ GeV$. The momentum of the e^+e^- pair is smaller than $2\ GeV$. This picture of the topology of the $B \to KJ/\psi$ and $B \to K^*J/\psi$ decays is based on the Monte Carlo studies (Appendix D).

5.3.2 Tagging of the decay $J/\psi \to e^+e^-$

Our task is to select multi-hadron events with at least two charged high-energy electromagnetically showering particles, called further electrons, which could originate from the $J/\psi \to e^+e^-$ decay. The reduction of the non-$B\bar{B}$ background was described in section 5.1.

First we select events with two or more high-energy electrons satisfying the following cuts:

- $800\ MeV < E_{13}^{CORR'} < 2800\ MeV$,

- $|\cos\theta| < 0.85$,

- A particle is recognized as charged by the standard reconstruction procedure, i.e. it has to be 'tagged' or 'tracked charged',

- $E_{24h} < 50\ MeV$,

- $0.84 < E_4/E_{13}^{CORR'} < 0.97$,

- $0.6 < E_1/E_4 < 0.98$.

The cut parameters have been described in detail in section 5.2. In comparison with the cuts applied in the analysis of the inclusive photon spectrum the requirements for the electron selection are looser. This is because we are interested here not in a single electron but in electron pair candidates from the J/ψ decay and stricter requirements would significantly reduce our efficiency of J/ψ reconstruction. The window in the electron energies comes from the kinematic limits for electrons from J/ψ decay. The spectrum of the e^+e^- invariant mass from ON $\Upsilon(4S)$ and continuum data obtained after this selection procedure is shown in Fig. 5.16. There is an indication of a signal around $3100\ MeV$. The background to the signal comes from pairs of particles in which one of them was misidentified as an electron and from pairs of electrons in which one of them comes from the decay of the other B meson. A spectrum of the e^+e^-
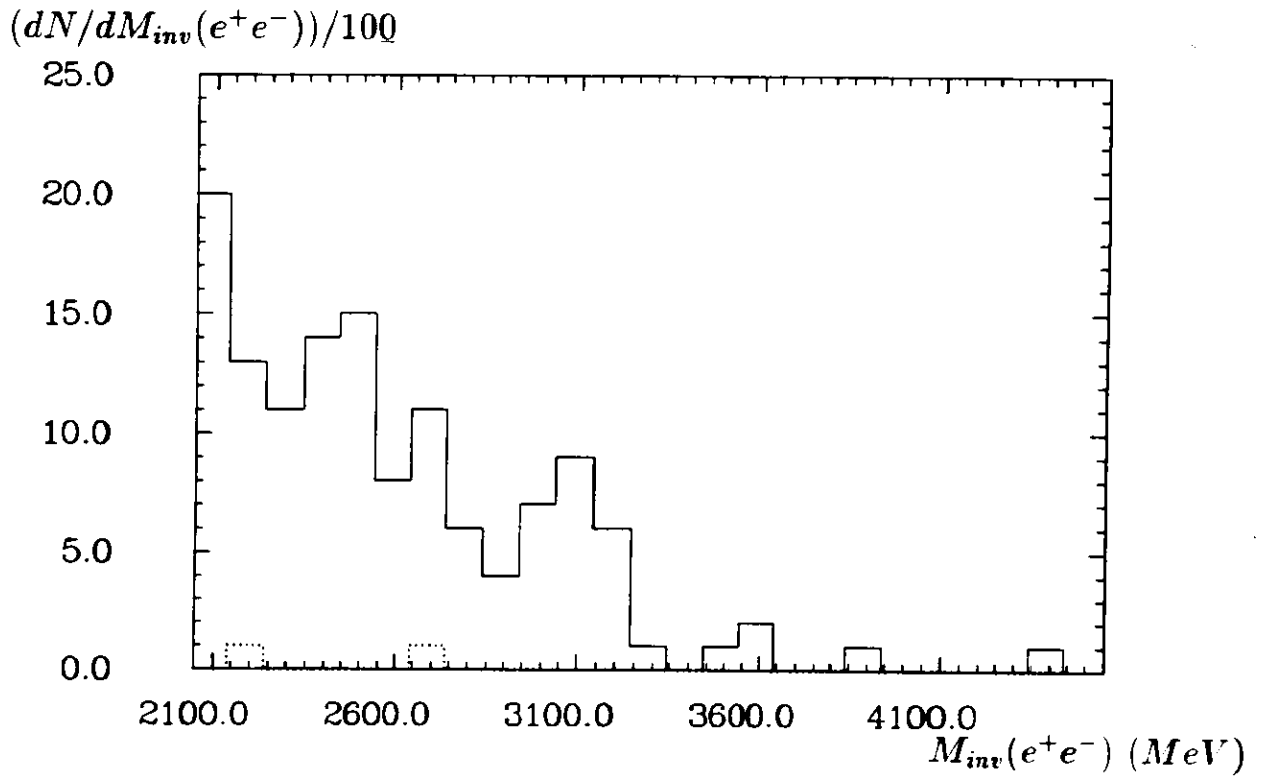
Figure 5.16: Spectrum of the e^+e^- invariant mass from ON $\Upsilon(4S)$ (solid histogram) and continuum data (two entries in the dotted histogram).
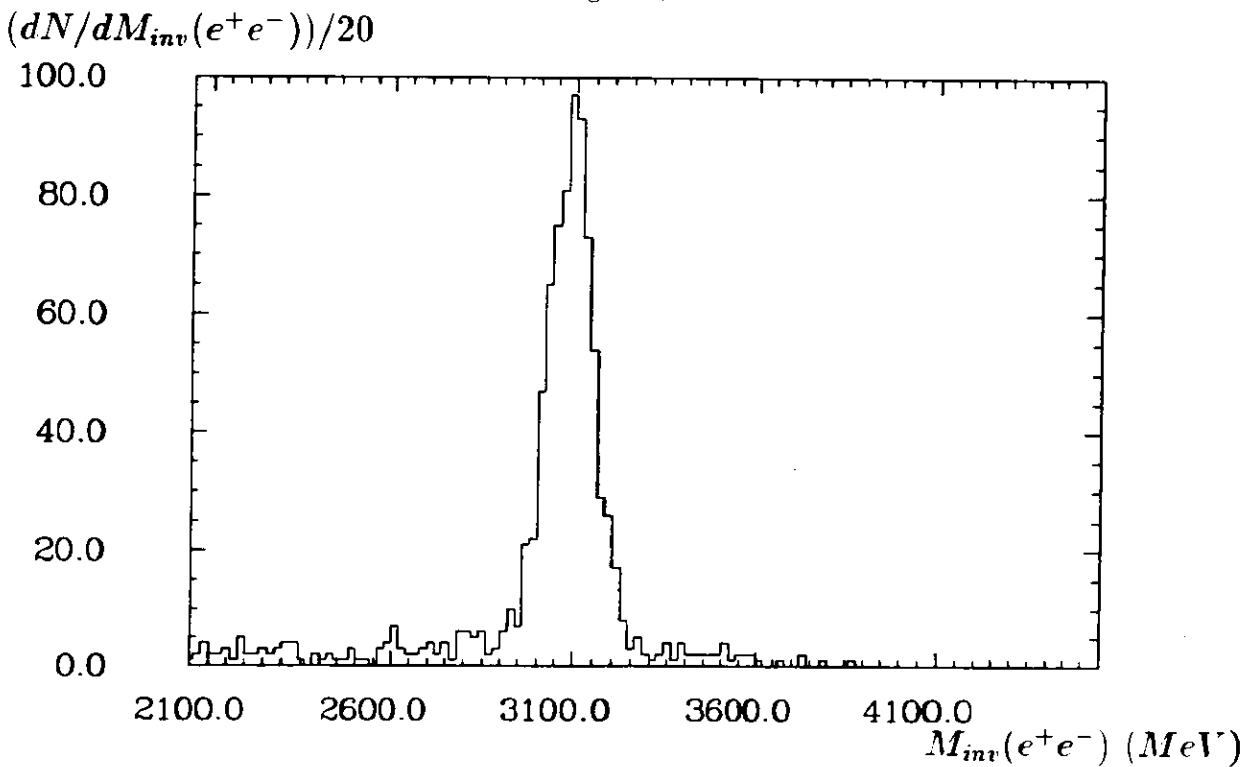
Figure 5.17: Spectrum of the e^+e^- invariant mass for the Monte Carlo sample simulating the process $\Upsilon(4S) \to B\bar{B}, B \to K^*(892)J/\psi, J/\psi \to e^+e^-$.

$(dN/d\cos(e1,e2))/0.02$
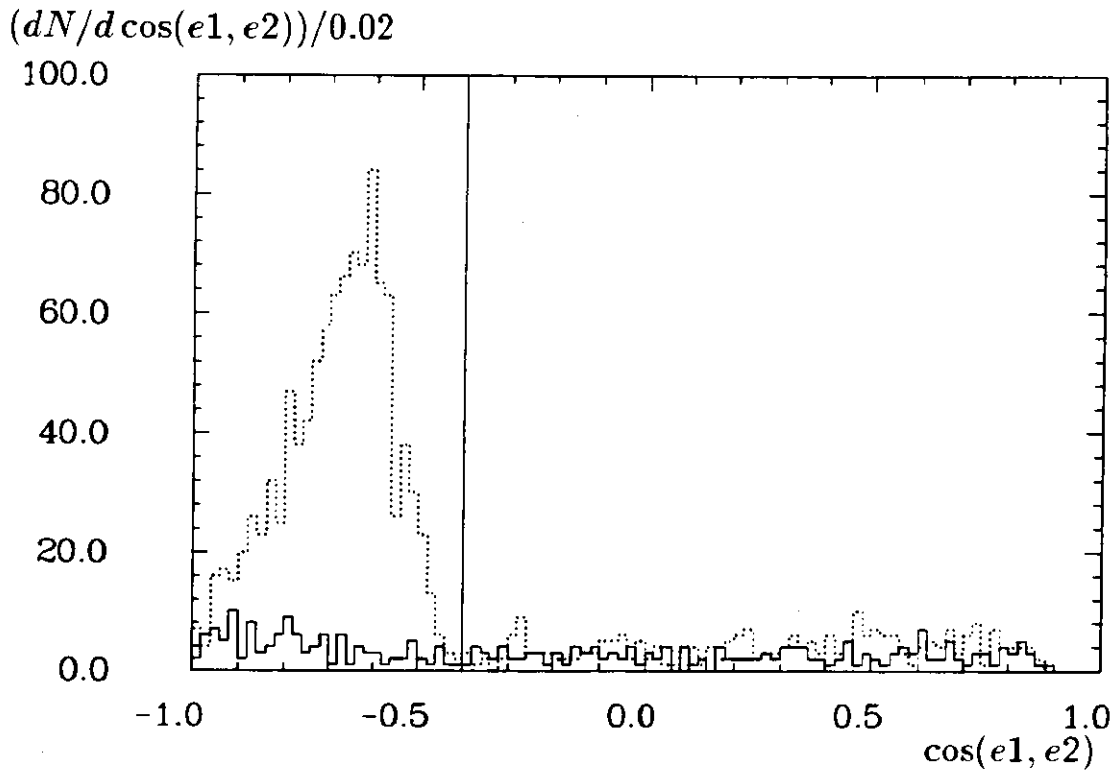
Figure 5.18: Distributions of the cosine of the angle between two electrons (all pairs of particles in one event which have passed our electron selection) for ON $\Upsilon(4S)$ data (solid histogram) and Monte Carlo sample (dotted histogram) simulating the process $\Upsilon(4S) \to B\overline{B}, B \to K^*(892)J/\psi, J/\psi \to e^+e^-$. We accept events to the left of a solid line.

$(dN/d \mid \vec{p}_{e_1 e_2} \mid)/250$
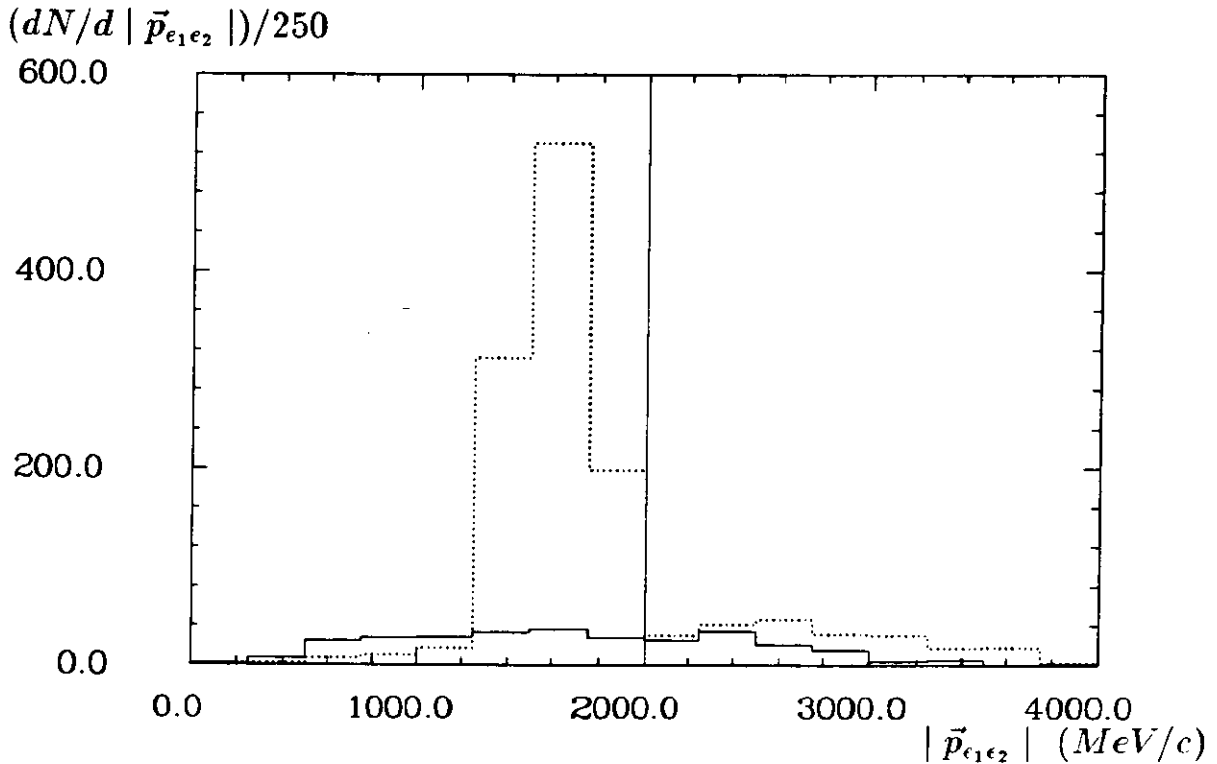
Figure 5.19: Momentum distributions of electron pairs (all pairs of particles in one event which have passed our electron selection) for ON $\Upsilon(4S)$ data (solid histogram) and Monte Carlo sample (dashed histogram) simulating the process $\Upsilon(4S) \to B\overline{B}, B \to K^*(892)J/\psi, J/\psi \to e^+e^-$. We accept events to the left of a solid line.

54

invariant mass from Monte Carlo sample simulating the process $B \rightarrow K^*(892)J/\psi$ is shown in Fig. 5.17.

In the selected events we tag the decay $J/\psi \rightarrow e^+e^-$ by looking for electron pairs satisfying the following requirements (in case of more than two electron candidates we consider all combinations):

- $2900\ MeV < M_{inv}(e1, e2) < 3300\ MeV$,

- $\cos(e1, e2) < -0.4$,

- $|\vec{p}_{e1e2}| < 2000\ MeV/c$.

Fig. 5.16, 5.18 and 5.19 show the distributions of the invariant mass of the electron pair, of the angle between two electrons and of the momentum of the electron pair, respectively, for ON $\Upsilon(4S)$ data and the Monte Carlo sample simulating the process $\Upsilon(4S) \rightarrow B\overline{B}, \overline{B} \rightarrow$ all, $B \rightarrow K^*(892)J/\psi, J/\psi \rightarrow e^+e^-$ before applying the above cuts. By the electron momentum we understand the vector whose direction coincides with the track direction of the selected particle and whose absolute value is equal to the particle energy. The momentum of the electron pair $\vec{p}_{e1e2}$ is defined as

$$\vec{p}_{e1e2} = \vec{p}_{e1} + \vec{p}_{e2}. \tag{5.17}$$

The invariant mass $M_{inv}(e1, e2)$ of electron pair is calculated according to the formula

$$M_{inv}^2(e1, e2) = (E_{e1} + E_{e2})^2 - (\vec{p}_{e1} + \vec{p}_{e2})^2 \tag{5.18}$$

and we demand that it should be equal to the J/ψ mass (3097 MeV) within 3σ. The last two cuts have been tuned with the Monte Carlo simulation. They are very loose and do not reject any of electron pairs simulated for our processes. Electron pairs which do not pass these cuts result from combining an electron from the decays $\Upsilon(4S) \rightarrow B\overline{B}, B \rightarrow K^{(*)}J/\psi, J/\psi \rightarrow e^+e^-$ with a high-energy electron from the decay of the other B meson or where both B mesons decay semileptonically.

5.3.3 Branching fraction for the decay $B \rightarrow J/\psi X$

As a cross-check, e.g. of our mass scale, we fit a Gaussian signal with a polynomial background to the $M_{inv}(e1, e2)$ invariant mass spectrum (Fig. 5.16) in order to obtain J/ψ parameters (Table 5.7). The branching fraction for the inclusive $B \rightarrow J/\psi X$ (X denotes here any system of particles allowed by the relevant conservation laws) decay is calculated as:

$$BR(B \rightarrow J/\psi X) = \frac{N_{J/\psi}^{vis}/\epsilon_{J/\psi}}{(2N_{B\overline{B}}^{vis}/\epsilon_{had})BR(J/\psi \rightarrow e^+e^-)}. \tag{5.19}$$

The efficiency of the selection of multi-hadron events was found to be $\epsilon_{had} = (92.0 \pm 0.5 \pm 0.9)\%$ in section 5.2 describing the analysis of inclusive photon spectrum. As the efficiency for the J/ψ tagging we used the mean value from Table 5.8 (see below) i.e. $\epsilon_{J/\psi} = (11.9 \pm 0.9)\%$. An agreement of our mass and BR with the PDG [39] values represents an overall check of our procedure.

55

5.3.4 The spectrum of the missing mass with respect to the J/ψ

We search for the decay modes $B \to KJ/\psi$ and $B \to K^*J/\psi$ in the spectrum of the missing mass with respect to the J/ψ . The missing mass is defined as:

$$M_{miss}^2 = (E_B - E_{ele2})^2 - (\vec{p}_B - \vec{p}_{ele2})^2 \approx (E_{BEAM} - E_{ele2})^2 - (\vec{0} - \vec{p}_{ele2})^2, \qquad (5.20)$$

where:

$$E_{ele2} = E_{e1} + E_{e2}. \qquad (5.21)$$

This definition contains two approximations. We use the well measured beam energy E_{BEAM} instead of energy E_B of the B meson and we neglect its momentum (320 MeV/c). These approximations result in a broadening of the signal distribution. This is included in our Monte Carlo simulations of the processes $B \to KJ/\psi$ and $B \to K^*J/\psi$, in the M_{miss}^2 spectrum.

The last cut in the plane ($M_{miss}^2, \cos\alpha$) is intended to select events with at least one particle with a large angle with respect to the J/ψ :

- $\cos\alpha < 0.05(M_{miss}/GeV)^2 - 0.9$,

where α denotes here the angle between J/ψ as reconstructed from e^+e^- pair and the direction of the 'opposite' particle (see section 5.3.1). Plots of $\cos\alpha$ versus the square of the missing mass M_{miss}^2 for ON $\Upsilon(4S)$ data and for events from a Monte Carlo simulation of the process $\Upsilon(4S) \to B\bar{B}, B \to K^{(*)}J/\psi, J/\psi \to e^+e^-$ are shown in Fig. 5.20.

The plot of the square of the missing mass with respect to the J/ψ versus the e^+e^- invariant mass for ON $\Upsilon(4S)$ data after our full selection is shown in Fig. 5.21.

5.3.5 Efficiency of the J/ψ tagging

In order to estimate the efficiency for tagging the decay modes $B \to K^{(*)}J/\psi$ by the selection of two electrons coming from the J/ψ decay we use the LUND 6.1 program to simulate the $\Upsilon(4S)$ meson decays at rest into $B\bar{B}$ pairs. In each simulated event exactly one $B(\bar{B})$ meson decays further into one of the $K^{(*)}$ states and J/ψ which in turn decays into a e^-e^- pair. The efficiencies for the detection of one electron (ϵ_e) , two electrons (ϵ_{ee}), for the J/ψ reconstruction based on the selection of the electron pairs ($\epsilon_{J/\psi}$) and of the selection of events with a particle at large angle with respect to the J/ψ ($\epsilon_{K^{(*)}J/\psi}$) are collected in Table 5.8. We estimate these efficiencies for the modes: $B \to KJ/\psi$, $B \to K^*(892)J/\psi$, $B \to K_1(1400)J/\psi$ and $B \to K_3^*(1780)J/\psi$.

For the modes $B \to KJ/\psi$ and $B \to K^*(892)J/\psi$ we have studied by Monte Carlo the differences in the efficiency for neutral and charged B meson decays. The total systematic error on $\epsilon_{J/\psi}$ is 0.7%. It has been calculated in the same way as for the efficiency in the inclusive photon spectrum analysis (section 5.2).

5.3.6 Determination of the upper limits for the decays $B \to KJ/\psi$ and $B \to K^*J/\psi$

We estimate upper limits of the number of events originating from the decays $B \to KJ/\psi$ and $B \to K^*J/\psi$ by performing a maximum likelihood fit to the unbinned data points (22 entries) of the squares of the missing mass with respect to the J/ψ. We use the extended likelihood
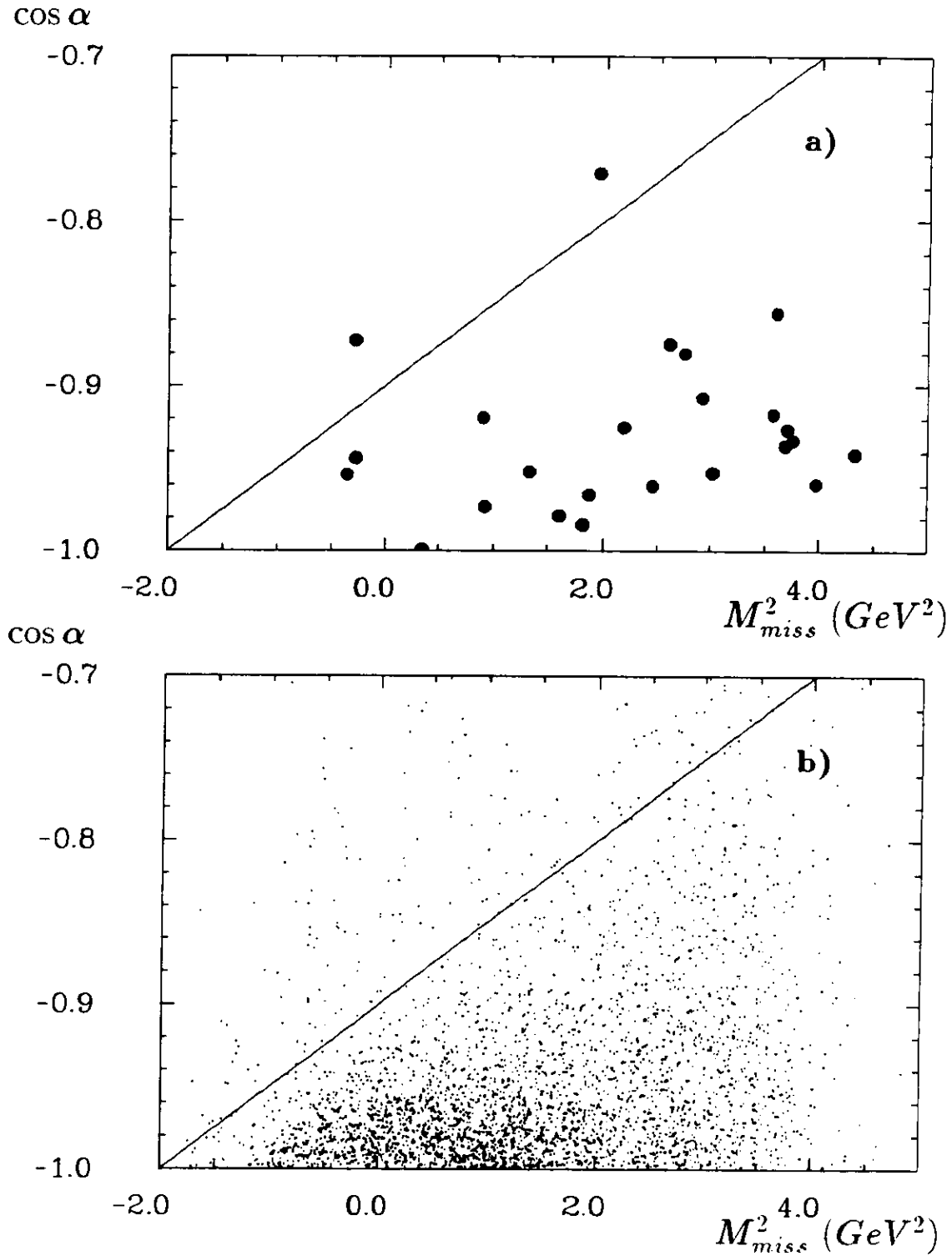
Figure 5.20: Scatter plots of the cosine of the angle between J/ψ and the 'opposite' particle versus the square of the missing mass with respect to the J/ψ for (a) ON $\Upsilon(4S)$ data and for (b) the Monte Carlo sample simulating the processes $\Upsilon(4S) \rightarrow B\overline{B}, B \rightarrow K^{(*)}J/\psi, J/\psi \rightarrow e^+e^-$ (four Monte Carlo samples for K, $K^*(892)$, $K_1(1400)$ and $K_3^*(1780)$ have been merged here). The plots were obtained for events which satisfied all the requirements listed before applying the cut in this plane. We accept events below the solid line.

Table 5.7: J/ψ parameters resulting from the fit to the spectrum of the invariant mass of the electron pair.

Parameter	This analysis	PDG
mass (MeV)	3093 ± 33	3096.9 ± 0.1
$N^{vis}_{J/\psi}$ (events)	12.8 ± 5.2	
$BR(B \to J/\psi X)$ (%)	1.1 ± 0.6	1.12 ± 0.18

Table 5.8: Efficiencies (in %) for $B \to K J/\psi$ and $B \to K^* J/\psi$ decay modes. The errors are only statistical. The common systematic error on $\epsilon_{J/\psi}$ is 0.7%.

Mode	ϵ_e	ϵ_{ee}	$\epsilon_{J/\psi}$	$\epsilon_{K^{(*)}J/\psi}$
$B^- \to K^- J/\psi$	57.1 ± 0.9	16.2 ± 0.5	12.7 ± 0.4	11.8 ± 0.4
$B^\circ \to K^\circ J/\psi$	57.3 ± 0.9	16.7 ± 0.5	13.2 ± 0.4	12.3 ± 0.4
$B^- \to K^{*-}(892)J/\psi$	58.7 ± 0.9	16.2 ± 0.5	12.4 ± 0.4	11.7 ± 0.4
$B^\circ \to K^{*\circ}(892)J/\psi$	57.3 ± 1.0	16.6 ± 0.6	12.7 ± 0.5	12.0 ± 0.5
$B^- \to K_1^-(1400)J/\psi$	57.0 ± 0.9	15.2 ± 0.5	11.4 ± 0.4	11.0 ± 0.4
$B^- \to K_3^{*-}(1780)J/\psi$	55.4 ± 0.9	14.6 ± 0.5	10.9 ± 0.4	10.1 ± 0.4

method [46] with the following likelihood function

$$\mathcal{L}(N_{J/\psi}, N_{backgr}) = \frac{\exp(-(N_{J/\psi} + N_{backgr}))}{N!} \times \prod_i^N (N_{J/\psi} \cdot F_B(M^2_{miss_i}) + \frac{N_{backgr}}{\Delta M}), \qquad (5.22)$$

where:

$N = 22$ – number of fitted events

$N_{J/\psi}$ – number of signal events from the decay $B \to K^{(*)}J/\psi$ (fit parameter)

N_{backgr} – number of events of a constant background (fit parameter) in the fit range ΔM

F_B – bell function used as a signal parametrization, defined in equation E.1.

The parameters of the bell function are estimated from fits to the distributions of the missing mass with respect to the J/ψ for Monte Carlo samples simulating the processes investigated by us (Table E.3 in Appendix E).

We minimize -ln(likelihood) using the MINUIT [48] program. The fits were performed in the range of the M^2_{miss} of (-1.5,4.5) GeV^2. Their results are collected in Table 5.9. An example of the fit (in search for the $B \to K^*(892)J/\psi$ decay mode) is shown in Fig. 5.22. No signal from the decays $B \to K^{(*)}J/\psi$ is seen and therefore the fit results are converted into 90% C.L. upper limits on the number of signal events ($N^{UL}_{J/\psi}$ in Table 5.9) by integrating the likelihood function over the positive range of the signal amplitude.

It should be mentioned here that we have used the full sample of 22 events in our fit, while in section 5.3.3 we found that only (12.8 ± 5.2) from these events come from the decay $B \to J/\psi X, J/\psi \to e^+ e^-$. However, we cannot distinguish them from the background events in which one of the electrons was misidentified or originate from the decay of the other B meson.

58

Table 5.9: Fit results and 90% C.L. upper limits on branching fractions for $B \to K J/\psi$ and $B \to K^* J/\psi$ decays.

Mode	Signal amplitude $N_{J/\psi}$	$N_{J/\psi}^{UL}$ (90% C.L)	Systematic error on $N_{J/\psi}^{UL}$	BR^{UL} (90% C.L)	Conf. level (%)
$B \to K J/\psi$	$-5.4^{+3.9}_{-3.8}$	4.5	1.0	0.6×10^{-2}	90
$B \to K^*(892) J/\psi$	$-2.4^{+4.5}_{-4.3}$	6.4	1.5	0.8×10^{-2}	74
$B \to K_1(1400) J/\psi$	$4.3^{+4.4}_{-4.0}$	10.7	2.4	1.5×10^{-2}	83
$B \to K_3^*(1780) J/\psi$	$6.5^{+4.2}_{-3.7}$	12.6	2.4	1.9×10^{-2}	95

Table 5.10: Systematic uncertainties (in %) in the upper limit on the number of events for decays $B \to K^{(*)} J/\psi$ obtained from the fits to the missing mass spectrum with respect to the J/ψ .

Mode	Source of systematic error			Total systematic error
	Selection cuts	Signal shape	Fit range	
$B \to K J/\psi$	17	9	11	22
$B \to K^*(892) J/\psi$	17	3	17	24
$B \to K_1(1400) J/\psi$	17	2	14	22
$B \to K_3^*(1780) J/\psi$	17	3	9	19

Therefore, our upper limits resulting from the above fits are overestimated by a factor of about two, which is however badly known.

The systematic uncertainties in the calculation of the upper limits on the number of events from the decays $B \to K^{(*)} J/\psi$ have been studied by

- varying selection cuts (up to 12% of cut parameters presented above),

- extending fit range from (-1.5,4.5) GeV^2 to (-2.0,5.0) GeV^2,

- changing the signal parametrization (Table E.3 in Appendix E) from the bell to the Gaussian distribution.

The results of the estimation are collected in Table 5.10. Uncertainties from the individual sources are summed in quadrature.

The 90% C.L. upper limits on the the branching fraction for decays $B \to K^{(*)} J/\psi$ are evaluated as [46]:

$$BR(B \to K^{(*)} J/\psi) < \frac{N_{J/\psi}^{UL}/\epsilon_{K^{(*)} J/\psi}(1 + 1.28\sigma_{rel}^{stat})}{2 N_{B\bar{B}}^{vis}/\epsilon_{had} BR(J/\psi \to e^+e^-)},$$

(5.23)

59

M_{miss}^2 $GeV^2)$

7.0

5.0

3.0

1.0

-1.0

2500.0   2700.0   2900.0   3100.0   3300.0

$M_{inv}(e^+e^-)$ (MeV)
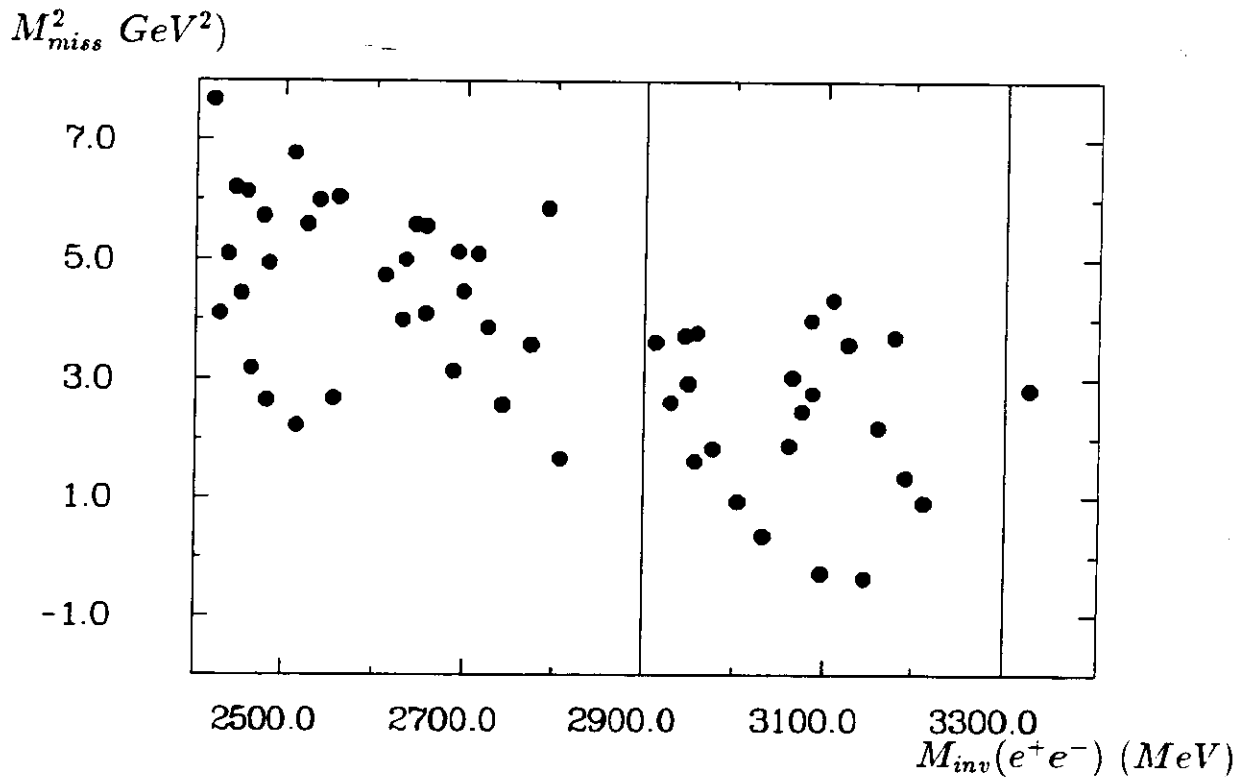
Figure 5.21: Plot of the square of the missing mass with respect to the J/ψ versus the e^+e^- invariant mass for ON $\Upsilon(4S)$ data. We accept events between the vertical lines.

$(dN / dM_{miss}^2) / 0.5$

10.0

$B \to K^*(892)J/\psi$

5.0

0.0

-2.0   0.0   2.0   4.0   6.0

M_{miss}^2 (GeV^2)
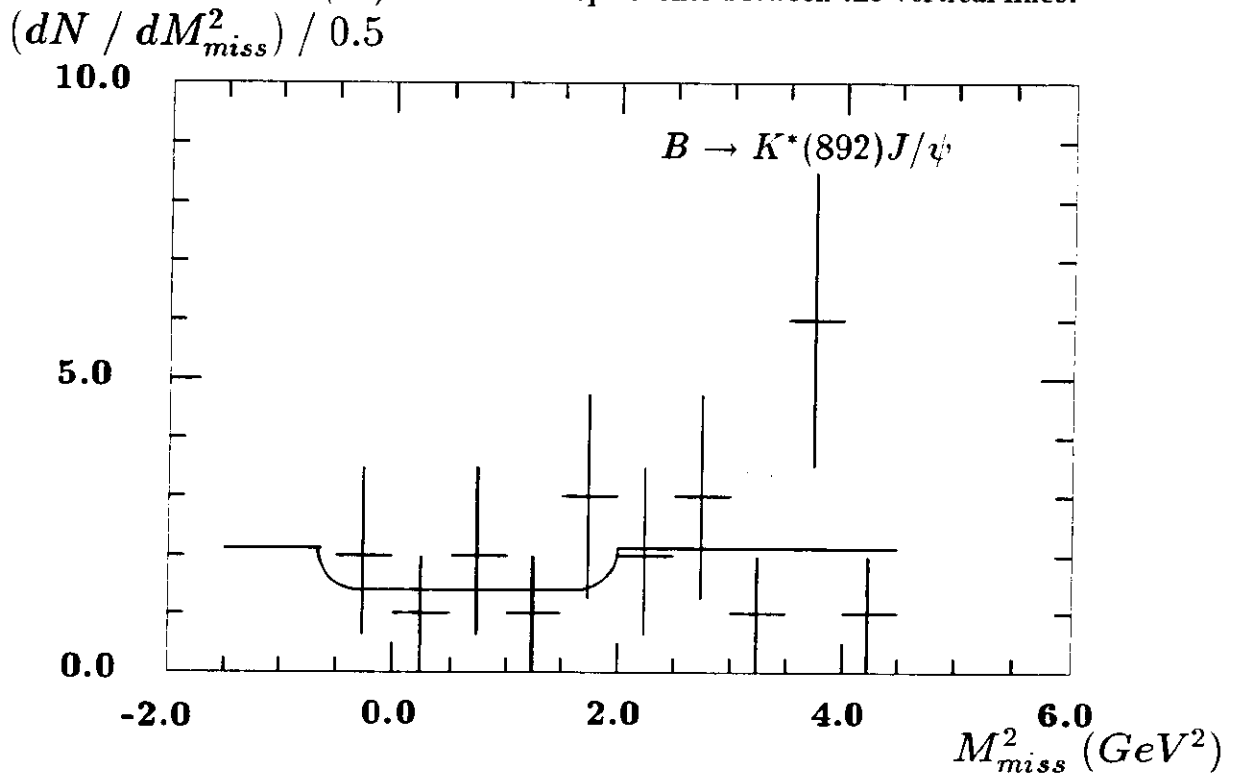
Figure 5.22: Fit of a bell function to the spectrum of the missing mass with respect to the J/ψ (in search for the decay $B \to K^*(892)J/\psi$).

60

$$BR(B \to K^{(*)}J/\psi) \times 10^3 \quad (90\% \text{ C.L.})$$
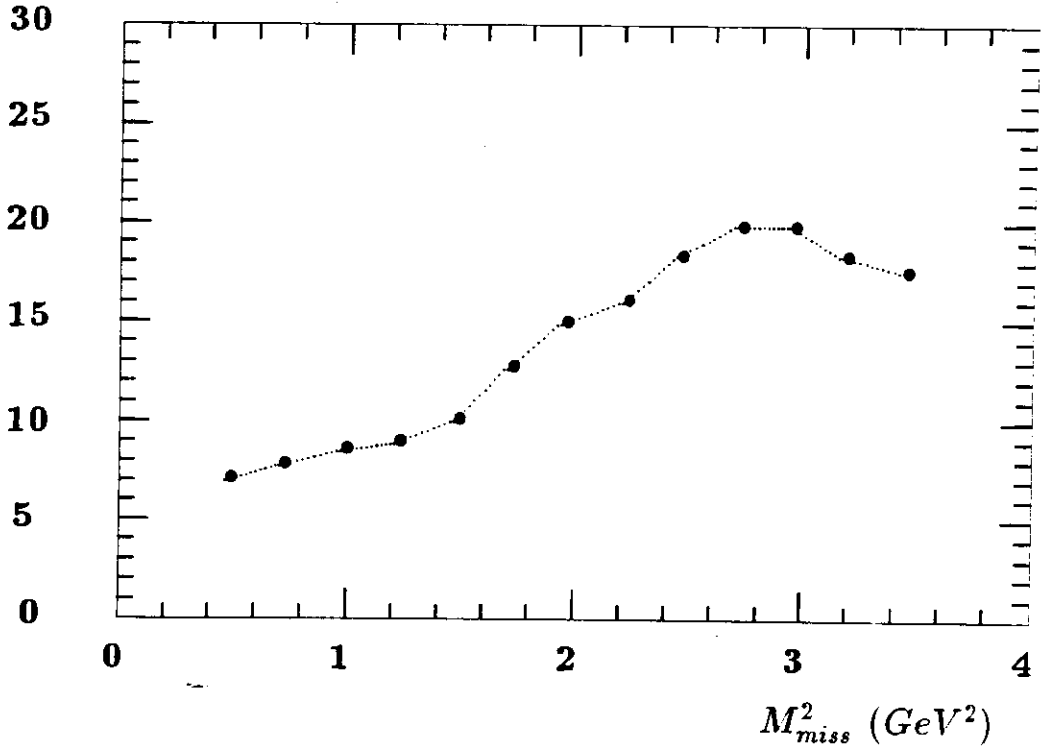
Figure 5.23: 90% C.L. upper limit for the branching fraction of the decay $B \to K^{(*)}J/\psi$ as a function of the missing mass squared M^2_{miss} measured with respect to the J/ψ.

where σ^{stat}_{rel} denotes the relative statistical error of the factor $2(N^{vis}_{B\bar{B}}/\epsilon_{had})BR(J/\psi \to e^+e^-)\epsilon_{K^{(*)}J/\psi}$ with the individual contributions added in quadrature. The factor $(1 - 1.28\sigma^{stat}_{rel})$ converts this expression into an upper limit at 90% confidence level. The systematic errors in efficiencies for the hadronic event selection, for the selection of $K^{(*)}J/\psi$ events and the systematic uncertainties in the branching fraction for the leptonic decay of the J/ψ and in the calculation of the upper limit on the number of signal events originating from the fit procedure were summed in quadrature resulting in the relative systematic error σ^{sys}_{rel} of the estimation of the upper limit on the branching fraction for the decays $B \to K^{(*)}J/\psi$. These errors have been added linearly to the result obtained according to formula (5.23) by multiplying it by the factor $(1 + \sigma^{sys}_{rel})$. Our results are collected in Table 5.9.

We also present the plot of the 90% C.L. upper limit for the the branching fraction for decays $B \to K^{(*)}J/\psi$ versus the square of the $K^{(*)}$ (missing) mass (Fig. 5.23). For these fits the bell function signal with $\sigma = 2$ and $z = 0.175$ have been taken. For the efficiency of the selection of the events in question we used

$$\epsilon_{K^{(*)}J/\psi} = ((-0.6 \pm 0.1) \times M^2_{miss} \ (GeV^2) + (12.1 \pm 0.3))\%. \tag{5.24}$$

obtained from the fit of a straight line to four $\epsilon_{K^{(*)}J/\psi}$ points from Table 5.8. A common systematic error of 22% (corresponding to the estimation for the mode $B \to K_2(1400)J/\psi$ for which the missing mass spectrum centres at 2 GeV i.e. in the middle of the range under investigation) for the upper limit for the number of signal events has been assumed.

Our results are discussed in Chapter 6.

6. Conclusions

We have not seen any monoenergetic photon line in the inclusive spectrum of high-energy photons coming from $\Upsilon(4S)$ decays. In particular no photons are seen in the decay $B \to \gamma X$, where X denotes any state with mass between 892 MeV and 2900 MeV. The same is true for the exclusive decays $B \to K^*\gamma$ where K^* denotes various strange states. Our 90% C.L upper limits on branching fractions for the decays $b \to s\gamma$ and $B \to K^*\gamma$ are listed and compared with results of the CLEO and ARGUS experiments in Tables 6.1 and 6.2. We are not able to distinguish between charged and neutral B meson decay modes. Therefore our estimates are valid for the mixture of 50% of charged and 50% of neutral B decays (see Table 6.2).

The upper limit on the branching fraction for the decay $B \to \gamma X$ may be considered as the limit for the flavour changing neutral current $b \to s\gamma$ assuming that only strange states contribute to X. This is similar to the recent ARGUS and CLEO results (Table 6.1). It is, however, obtained with the direct inclusive measurement of the photon spectrum, and therefore free from theoretical uncertainties concerning the ratio $\Gamma(B \to K^*(892)\gamma)/\Gamma(b \to s\gamma)$ ([30]-[32]). Thus it can be treated as complementary with respect to the results of the above experiments, if not more important because it is free from these theoretical uncertainties.

The present experimental constraints on the branching fraction on the decay $b \to s\gamma$ do not yet provide a stringent test of the Standard Model and do not indicate any new physics ([1]-[3]). The constraints on the mass of the top quark m_t and on masses of new particles predicted in the extensions of the Standard Model and in supersymmetric theories resulting from our work are weaker than those from other experiments. Our limit on the branching fraction for $b \to s\gamma$ (see Eq. 2.13) implies that $m_t < 2100 \; GeV$, which is far from the present bounds (cf. sec. 2.2.1). Taking into account that our limit is higher than 10^{-3} we see that the constraints on the masses of the gluino and the lightest squark (see Fig. 2.11), which may be evaluated from our result on $BR(b \to s\gamma)$, would be weaker than those obtained by the UA2 collaboration [37] ($m_{\tilde{b}} > 74 \; GeV$ independently of the gluino mass, $m_{\tilde{g}} > 79 \; GeV$ independently of the squark mass and $m_{\tilde{q}} = m_{\tilde{q}} > 106 \; GeV$ at 90% C.L.).

There is a hope that the testing of the branching fraction for the process $b \to s\gamma$ down to the level of 10^{-5} will be possible in the next generation of e^+e^- experiments, e.g. by the CLEO II

Table 6.1: Comparison of upper limits for the branching fraction for the decay $b \to s\gamma$ ($BR \times 10^3$ at 90% C.L.). The CLEO and ARGUS results from [49] and [50] are based on the experimental upper limit for the branching fraction for the exclusive mode $B^\circ \to K^{*\circ}(892)\gamma$ (see Table 6.2).

Assumed value of $\dfrac{\Gamma(B^\circ \to K^{*\circ}(892)\gamma)}{\Gamma(b \to s\gamma)}$	$BR(b \to s\gamma) \times 10^3$		
	CLEO	ARGUS	Crystal Ball
4.5%	6.2	9.3	4.1
40.0%	0.7	1.1	

Table 6.2: Summary of experimental results on upper limits for $B \to K^* \gamma$ decays ($BR \times 10^4$ at 90% C.L.). The CLEO and ARGUS results are taken from [49] and [50]. In case of the Crystal Ball the result refers to a mixture of the charged and neutral B meson decays.

Mode	CLEO	ARGUS	Crystal Ball
$B^\circ \to K^{*\circ}(892)\gamma$	2.8	4.2	18.0
$B^+ \to K^{*+}(892)\gamma$	5.5	5.2	
$B^\circ \to K_1^\circ(1270)\gamma$		78.0	
$B^+ \to K_1^+(1270)\gamma$		66.0	
$B^\circ \to K_1^\circ(1400)\gamma$		48.0	13.4
$B^+ \to K_1^+(1400)\gamma$		20.0	
$B^\circ \to K_2^{*\circ}(1430)\gamma$		4.4	
$B^+ \to K_2^{*+}(1430)\gamma$		13.0	
$B^\circ \to K^{*\circ}(1680)\gamma$		22.0	
$B^+ \to K^{*+}(1680)\gamma$		17.0	
$B^\circ \to K_2^\circ(1770)\gamma$			9.2
$B^+ \to K_2^+(1770)\gamma$			
$B^\circ \to K_3^{*\circ}(1780)\gamma$		110.0	
$B^+ \to K_3^{*+}(1780)\gamma$		50.0	
$B^\circ \to K_4^{*\circ}(2045)\gamma$		48.0	8.6
$B^+ \to K_4^{*+}(2045)\gamma$		90.0	

detector at CESR (Cornell) or by experiments performed on future machines dedicated to the B meson physics (so-called B factories [51]).

In comparison with other experiments our estimate for the mode $B \to K^*(892)\gamma$, is about an order of magnitude higher than recent CLEO and ARGUS results. However, for higher mass K^* states the upper limits obtained by us are lower (see Table 6.2). We do not give estimates for the other K^* states like e.g. $K^*(1415)$, $K_0^*(1430)$ and $K_2^*(1430)$ which are very close in mass to $K_1(1400)$. The results are the same for all these four states since the difference in the expected photon energies is very small. The same is valid for the states $K^*(1680)$, $K_3^*(1780)$ and $K_2(1770)$.

No enhancement was also observed in the spectrum of the missing mass with respect to the e^+e^- pair. In Table 6.3 our upper limits are compared with those from the CLEO and ARGUS experiments. In case of the decays $B \to KJ/\psi$ and $B \to K^*(892)J/\psi$ we present also theoretical predictions for branching fractions calculated in the Standard Model. The branching fractions for the decays $B \to KJ/\psi$ and $B \to K^*(892)J/v$ obtained by the CLEO and ARGUS are consistent with theoretical predictions (Table 6.3). Our estimates for these modes are about one order of magnitude higher. This is because the Crystal Ball cannot measure momentum of charged particles contrary to the CLEO and ARGUS detectors, which can reconstruct the K^* states. In addition their integrated luminosity was higher (162 and 212 pb^{-1}, respectively) than ours. On the other hand it is in our work that upper limits on branching fractions for decays $B \to K^{(*)}J/\psi$ with $K^{(*)}$ states heavier than $K^*(892)$ have been first determined. Let us remind here again that our upper limits are probably overestimated (see Sec. 5.3.6).

Table 6.3: Summary of theoretical predictions and experimental results for $B \to K^{(*)}J/\psi$ decays ($BR \times 10^4$). The CLEO and ARGUS results are taken from [33, 52]. In case of the Crystal Ball results we present (90 % C.L.) upper limits for the branching fractions referring to a mixture of the charged and neutral B meson decays.

Mode	Theory	CLEO	ARGUS	Crystal Ball
$B^+ \to K^+J/\psi$	8 ± 2	9 ± 6	7 ± 4	
$B^- \to K^-J/\psi$		5 ± 2		< 57
$\bar{B}^\circ \to \bar{K}^\circ J/\psi$		4 ± 3		
$B^\circ \to K^{*\circ}(892)J/\psi$	16 ± 4	41 ± 20	33 ± 18	< 83
$B \to K_1(1400)J/\psi$				< 147
$B \to K_3^*(1780)J/\psi$				< 186

Appendices

A. Energy measurement

A knowledge of the absolute energy scale is crucial in our analysis. We explain here the procedure of calibration of the crystal constants and we discuss small empirical correction to the energy E_{13}^{CORR}.

A.1 Calibration of crystals

The aim of the calibration is to determine the relation between the amount of light detected in the crystal photomultipliers and the deposited energy. The basic assumption checked experimentally by the Crystal Ball test module is that this relation is linear. The energy is measured for each crystal in two electronic channels called high- (HC) and and low-energy (LC), respectively. Therefore it is necessary to determine (in MeV) four constants per each crystal i.e. two pedestals (PED_{LC}, PED_{HC}) and two slopes ($SLOPE_{LC}$, $SLOPE_{HC}$).

After measuring pedestals (without beam presence) the slopes are determined using two physical processes. The first one is the radiation of 0.1 mC Cs^{137} source placed in the centre of each hemisphere. Gamma rays emitted with energy of 0.66 MeV deposit their whole energy in one crystal. The pulse-height from these photons determines the slope of the low-energy channel $SLOPE_{LC}$. In the second process 6.13 MeV photons are produced by 450 keV protons from the Van de Graaff generator impinging against a LiF target via the reaction $^{19}F(p,\alpha)$ $^{16}O^*$, $^{16}O^* \rightarrow$ $^{16}O + \gamma(6.13)$. In this energy range the photon shower is spread over more than one crystal. As a result a single crystal cannot be calibrated without knowing the slopes and pedestals of the others. Therefore the calibration is done iteratively starting from the slopes determined using Cs^{137}.

Final values of the calibration constants are calculated off-line. First the pedestals are determined from the crystal pulse heights for the data sample in which no signal is present. The slopes of the low- and high-energy channel are then obtained using signals from $e^+e^- \rightarrow e^+e^-$ Bhabha events (Bhabha calibration) selected as events with two clusters of energy greater than 0.8 E_{BEAM}. The calculation is done by a similar iterative procedure starting from the slopes calculated in the previous steps of calibration. The whole calibration procedure was performed every two weeks when the Crystal Ball was running.

The ADC counts C_{LC}, C_{HC} from two electronic channels of a photomultiplier are recalculated into energies deposited in individual crystals according to the formula:

$$E_{crystal} = \begin{cases} (C_{HC} - PED_{HC}) \times SLOPE_{HC} & if \quad C_{HC} > 350 \\ (C_{LC} - PED_{LC}) \times SLOPE_{LC} & if \quad C_{HC} \leq 350. \end{cases} \quad (A.1)$$

A.2 Energy correction

The absolute energy scale is set, over the whole energy range, by the calibration with Bhabha electrons, which have energies of about 5 GeV. However studies of the $\Upsilon(2S) \rightarrow \pi^\circ\pi^\circ\Upsilon(1S)$ transitions in the exclusive channels $\gamma\gamma\gamma e^+e^-$ and $\gamma\gamma\gamma\mu^-\mu^-$ reveal that, due to small nonlinearlities in the energy detection system, both the π° mass and the $\Upsilon(2S) - \Upsilon(1S)$
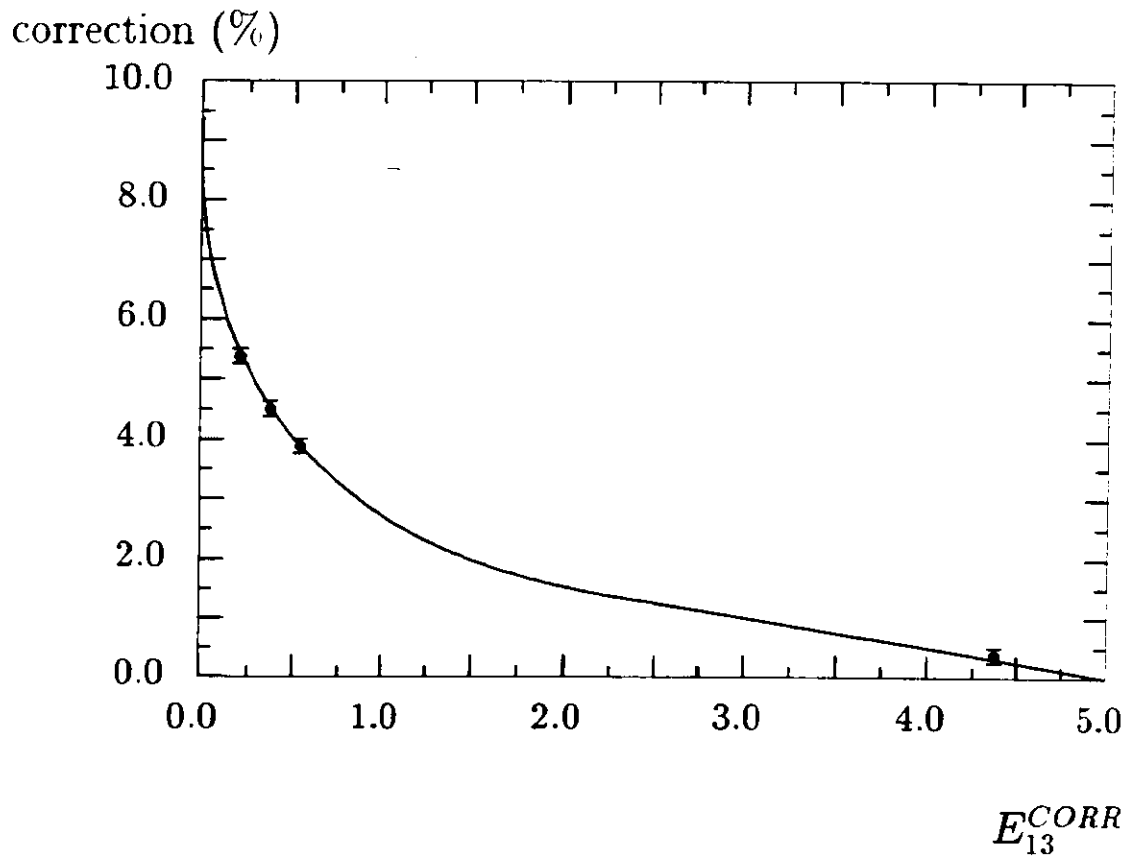
Figure A.1: Energy correction to E_{13}^{CORR}.

mass difference are too low in comparison with the values from the PDG tables [39]. In order to remove this discrepancy the following empirical correction, found by D. Gelphman [53], was applied:

$$E_{13}^{CORR'} = \frac{E_{13}^{CORR}}{1 + 0.0137 \ln \frac{E_{13}^{CORR}}{E_{BEAM}}}, \tag{A.2}$$

where E_{BEAM} is the beam energy. In this study the energy $E_{13}^{CORR'}$ is used as a measure of the energy deposition of electromagnetically showering particles. Fig. A.1 shows the correction as a function of the energy E_{13}^{CORR}.

B. Luminosity measurement
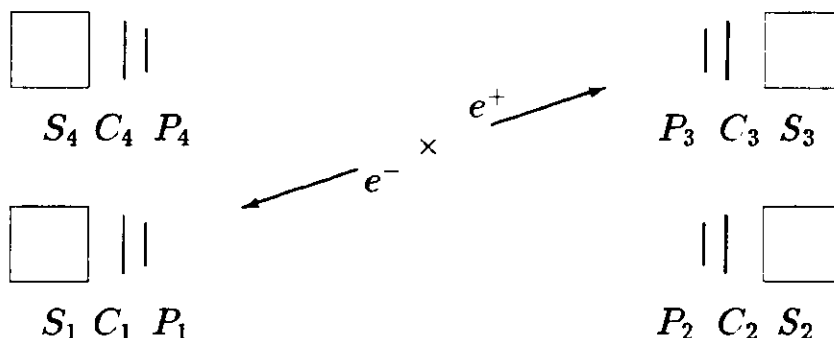
Figure B.1: Small–angle luminosity monitor. $S_i (i = 1, 2, 3, 4)$ are the lead–scintillator sandwich shower counters located at about $8°$ from the beam axis, C_i and P_i are scintillator counters. Cross and two vectors mark the interaction point and the $e^+ e^-$ Bhabha pair. Luminosity events are triggered by back-to-back coincidences of the (1–3) or (2–4) CP counters and high-energy shower in the corresponding S counters.

The luminosity $\mathcal{L}$ of an accelerator is defined as the proportionality factor between the observed rate of events $\mathcal{N}_{vis}$ and the cross-section σ_{vis} for a given process:

$$\mathcal{N}_{vis} = \mathcal{L} \times \sigma_{vis}. \tag{B.1}$$

Therefore the luminosity measurement is necessary to determine the cross-sections from the observed event rates. In principle it is possible to calculate this quantity for $e^+ e^-$ storage rings from the formula:

$$\mathcal{L} = \frac{N_b n_1 n_2 \nu}{\sigma_1 \sigma_2} \tag{B.2}$$

where N_b is the number of bunches, n_1, n_2 numbers of particles per bunch, ν, σ_1, σ_2 are the revolution frequency and the overlapping areas of the beams respectively. The main disadvantage of this method lies in the difficulty in the measurement of the beam areas. An alternative and commonly used way is based on calculating the luminosity directly from the definition B.1 by measuring the number of events for a process for which the cross-section is well known theoretically. In the case of $e^+ e^-$ experiments the most useful process is the Bhabha scattering because of its high rate and clean signature. The Crystal Ball measures luminosity by counting Bhabha events from the reactions:

$$
\begin{aligned}
e^+ e^- &\rightarrow e^+ e^- (\gamma) \\
e^+ e^- &\rightarrow \gamma\gamma(\gamma).
\end{aligned}
\tag{B.3}
$$

The second process must be considered in this measurement since the Bhabha events are reconstructed only from the signals in the Main Ball or in the small-angle luminosity monitor without using any charge information. This gives the additional contribution of about 10% in the counting rate within our selection criteria.

In our experiment the luminosity measurement is performed in two ways:

67

- at small angles (small-angle Bhabha events-SAB) using a small-angle luminosity monitor system (Fig. B.1),

- using the main detector itself (large-angle Bhabha events-LAB).

The first method is used only as a quick on-line check of the luminosity value while the second one offers more accuracy. however it has smaller counting rate and must be done off-line.

The Large Angle Bhabha events must satisfy the following requirements:

- $0.5 < E_{BALL}/(2 \times E_{BEAM}) < 1.2$,

- there should be exactly two energy clusters with $E_{13}^{CORR'} > 0.7 E_{BEAM}$ within $|\cos\theta| < 0.75$.

The integrated luminosity L is calculated from the number of events N_L passing the above cuts using the formula

$$L = N_L \times W^2/C,$$

(B.4)

where W is the centre-of-mass energy in GeV and its direct presence in the formula removes the leading $1/W^2$ behaviour of the cross-section. The constant C is related to the σ_{vis} by the formula

$$C = \sigma_{vis} \times W^2.$$

(B.5)

The factor C appears to be energy independent. Its value is determined by the Monte Carlo simulation of events from the reactions B.3 using Berends and Kleiss [54] event generator and by studying the corresponding detector response with the EGS 3 [55] program.

The systematic error of the luminosity measurement is estimated by adding in quadrature the following contributions:

- 2.0% from the dependence on the cuts applied to select Bhabha events,

- 1.0% from Monte Carlo statistics,

- 1.0% from the 4th order QED corrections [56] which are not included in the simulation,

- 0.2% from the hadronic and beam-gas background contribution,

- 0.1% from the weak energy dependence of the factor C.

The resulting systematic error of luminosity is 2.5%.

C. Particle identification

We discuss here some aspects of photon and electron identification in the Crystal Ball detector. Their selection is based on the lateral pattern of the particle energy deposition in the NaI(Tl) crystals of the Main Ball. Quantitatively, in order to distinguish electromagnetically showering particles from hadrons, we used so-called pattern cuts on the ratios E_1/E_4 and $E_4/E_{13}^{CORR'}$, while the separation of photons from π°'s was done with the help of the cut on the second moment of the lateral energy distribution.

C.1 Pattern cuts

As we have repeatedly stated the Crystal Ball is a non-magnetic detector and therefore the particle identification is based on the analysis of the lateral shape of the energy distribution in the NaI(Tl) crystals of the Main Ball. There are three classes of particles which can be identified in the detector: electromagnetically showering (e, γ, $\pi^\circ \rightarrow \gamma\gamma$), minimum ionizing (muons and $1/e \cong 1/3$ of hadrons) and hadrons which interact strongly inside the detector ($(e-1)/e \cong 2/3$ of hadrons).

Particles of the first class form an electromagnetic shower inside the Main Ball, i.e. a chain of reactions of Bremsstrahlung, e^+e^- pair production and ionization. The important parameter describing the spatial development of the shower is the radiation length. It is defined as the distance at which a high-energy electron loses all but $1/e$ of its energy to Bremsstrahlung. The thickness of the Main Ball corresponds to 16 radiation lengths and therefore electromagnetically showering particles with energies up to 5 GeV leave almost all their energy inside the detector. The lateral distribution of the energy deposition of an electron or a photon has a radial symmetry around the particle momentum direction (Fig. C.1a). Its lateral size is defined by the Molière radius (4.35 cm in case of NaI(Tl)) which almost exactly corresponds to the distance between neighbouring layers of crystals surrounding the local maximum of the energy deposit (Fig. 4.1). The cylinder based on a circle with a radius of 1, 2 and 3 Moliére radii centered along particle momentum contains 70, 95 and 99% of the shower energy, respectively (Fig. 4.1).

For hadrons the Main Ball thickness corresponds to one nuclear interaction length. This means that about $1/e$ of hadrons (and all muons) only ionize the medium of the Main Ball and deposit energy of about 210 MeV (with fluctuations described by the Landau distribution) in one or two crystals independently of nature and momentum of incident particle (Fig. C.1c). The remaining ($e - 1/e$ of hadrons interact strongly inside the Main Ball. The pattern of their lateral energy distribution is broad and very irregular (Fig. C.1d).

In order to distinguish high-energy photons from the hadronic background we have investigated the ratios

$$E_1/E4, \quad E_1/E_{13}^{CORR'}, \quad E_4/E_{13}^{CORR'} \quad \text{and} \quad E_1/E_{37}$$

for Monte Carlo events containing single photons, π^-'s and π°'s. The best acceptance has been obtained for the ratios $E_1/E4$ and $E_4/E_{13}^{CORR'}$ pattern cuts, which are plotted in Fig. C.2 for Monte Carlo photons and π^- seen in the Main Ball with energies from 2 GeV to 3 GeV. Table
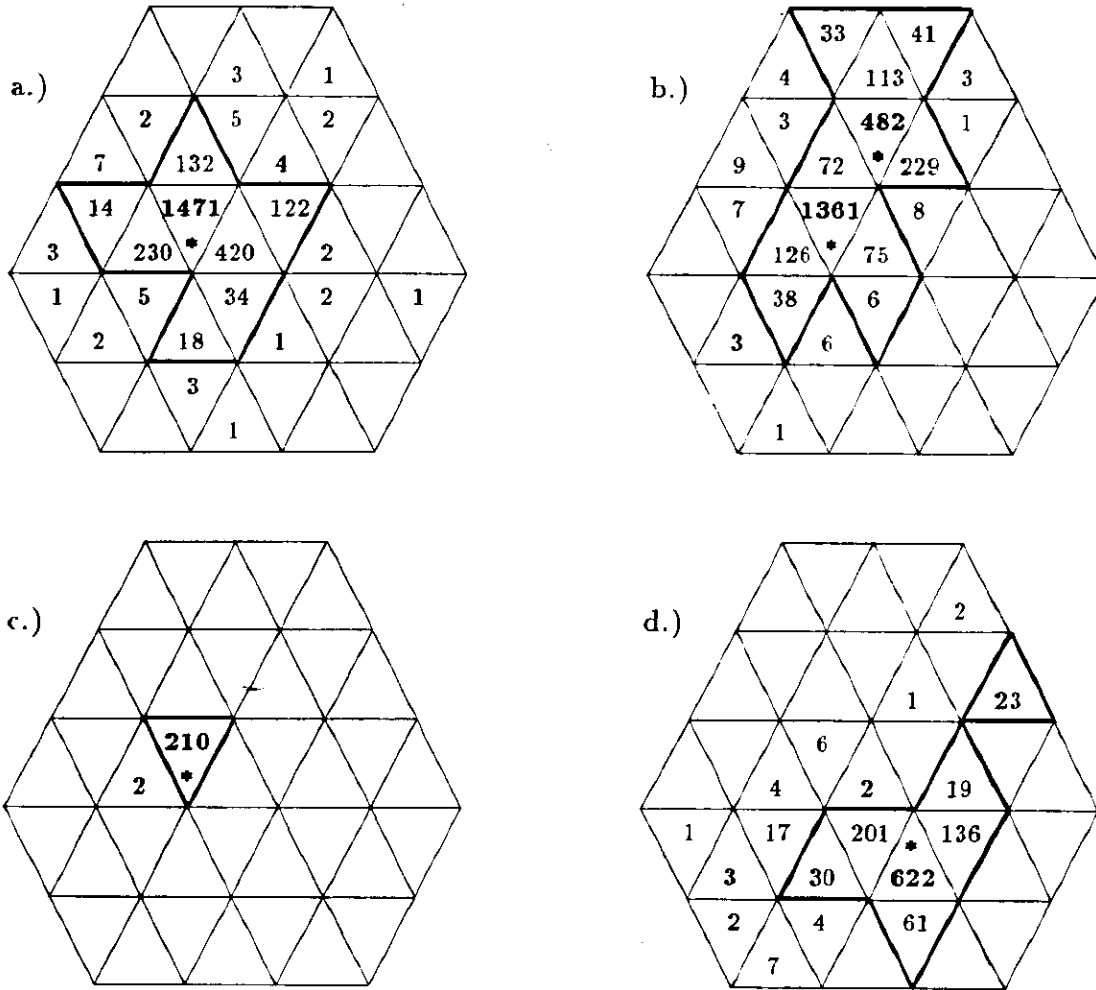
Figure C.1: Lateral shapes of energy depositions for: a) photon or electron with energy of 2.5 GeV, b) 2.5 GeV π°, c) high-energy muon and d) high-energy charged hadron interacting in the Main Ball. Borders of connected regions are shown as bold lines. The numbers are energy deposits in individual crystals in MeV. The bump modules are marked with an asterisk (*).

C.1 contains the acceptance of our pattern cuts for a single photon, π° and π^-. The errors quoted come only from the statistics of our Monte Carlo samples.

C.2 γ/π° separation

A π° is identified in the Crystal Ball detector via its decay into two photons. Below $E_{\pi^\circ} \approx 750\ MeV$ we deal with two separated neutral energy clusters with the invariant mass consistent with the π° mass. As the energy exceeds 750 MeV the mean angle between photons becomes so small that the clusters tend to overlap and form one connected region in the Main Ball (Fig C.1 b). These so-called 'merged' π°'s are difficult to be distinguished from photons. The efficiency of separation by pattern cuts is low in this case (see Fig. C.2). The identification is based on the observation that the energy deposit distribution of π° is of more oval shape than in case of photon, for which it is almost radially symmetrical (see Fig. C.1 a,b). The best quantitative measure of this effect is a second moment of the lateral energy distribution. It should be larger in case of more oval shape of merged π° distribution than for 'circular'

Table C.1: Acceptances (in %) of pattern cuts for a Monte Carlo photon, π° and π^- seen in the Main Ball with energies in the range from 2 GeV to 3 GeV.

Cut	Particle		
	γ	π°	π^-
$E_4/E_{13}^{CORR} > 0.84$	93.8 ± 2.2	66.6 ± 1.8	35.5 ± 1.9
$E_1/E_4 > 0.64$	78.6 ± 2.0	57.9 ± 1.7	39.9 ± 2.1
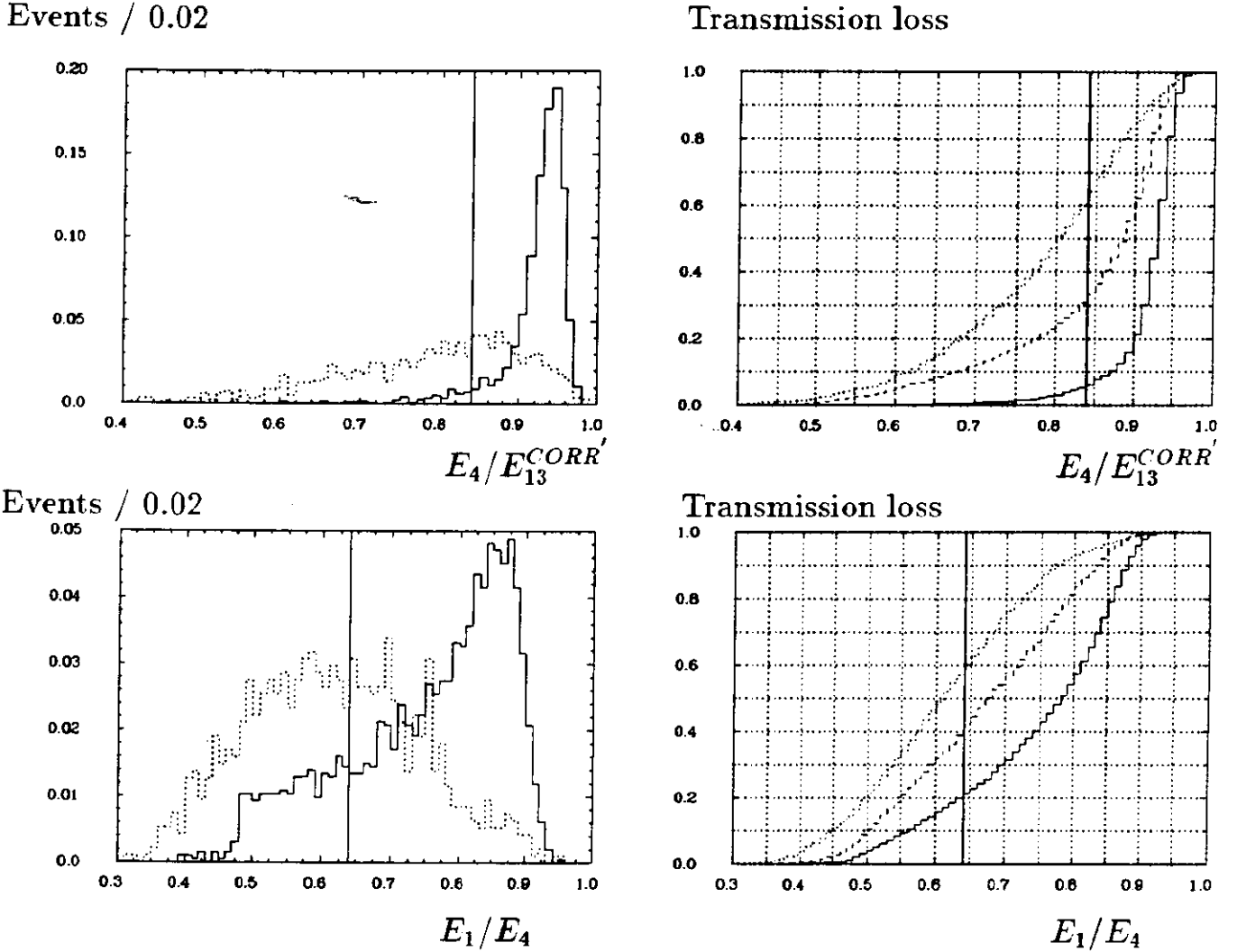
Figure C.2: The E_4/E_{13}^{CORR} (upper part) and E_1/E_4 (lower part) ratios for Monte Carlo photons (solid histogram) and π^-'s (dotted histogram) seen in the Main Ball with energies from 2 GeV to 3 GeV. The solid, dotted and dashed curves on pictures on the right side show the fraction of photons, π°'s and π^-'s, respectively, rejected by the cut: E_4/E_{13}^{CORR} (E_1/E_4) greater than the value at the horizontal axis. The cuts are shown as solid vertical lines.
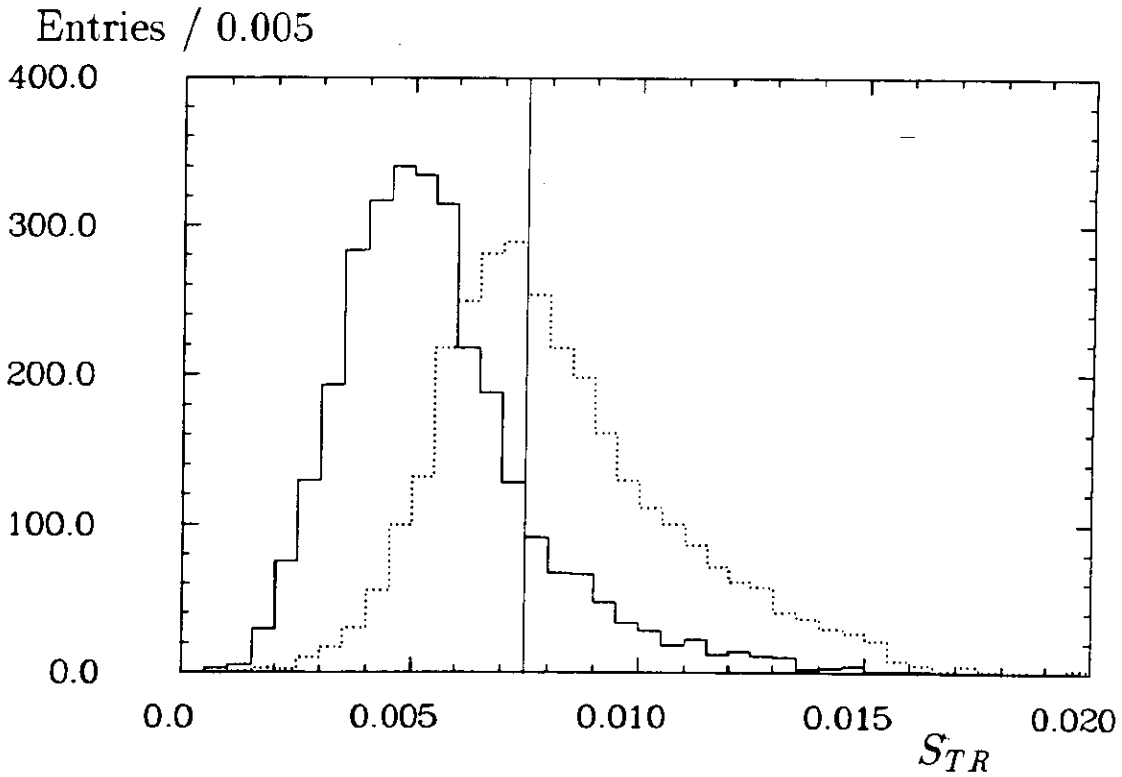
Figure C.3: The distributions of the second moment of the lateral energy S_{TR} for Monte Carlo photons (solid histogram) and π°'s (dotted histogram) with energies from 2 GeV to 3 GeV. Particles with $S_{t_r} < 0.0075$, i.e. to the left of the vertical line, have been accepted.

photon cluster. We define the zeroth degree moment as a total energy of a connected region:

$$E_{CONREG} = \sum_{i=1}^{N_{CONREG}} E_i, \qquad (C.1)$$

where N_{CONREG} is the number of crystals in a given connected region and E_i are energies of crystals. The first moment represents the centre of gravity of the energy distribution:

$$< \hat{p} > = \frac{1}{E_{CONREG}} \sum_{i=1}^{N_{CONREG}} E_i \cdot \hat{p}_i, \qquad (C.2)$$

where $\hat{p}_i$ are unit vectors starting from the centre of the Main Ball and pointing to the centre of the i-th module. Finally, the second moment of the lateral energy distribution is defined as a transverse shower width

$$S_{TR} = \frac{1}{E_{CONREG}} \sum_{i=1}^{N_{CONREG}} E_i \cdot (\hat{p}_i - < \hat{p} >)^2. \qquad (C.3)$$

From the second moment of the lateral energy distribution of a π° one has to subtract that one of the a γ slower [57]. Then it is

$$S_{TR}^{\pi^\circ} - S_{TR}^\gamma = (\frac{m_{\pi^\circ}}{E_{\pi^\circ}})^2. \qquad (C.4)$$

Fig. C.3 shows the second moment distributions for Monte Carlo events containing single photons and π°'s with energies from 2 GeV to 3 GeV as seen in the detector. By integrating plots from Fig. C.3 we obtain that as much as (85.5 ± 1.7) % of photons but only (46.1 ± 1.2) % of π°'s pass the cut: $S_{TR} < 0.0075$. The errors of these estimations come only from the statistics of both Monte Carlo samples from Fig. C.3.

D. Monte Carlo studies

In this analysis Monte Carlo techniques have been used to calculate the detection efficiency of rare B meson decays. The Monte Carlo simulation of the process under investigation proceeded in the following three steps (Fig. D.1):

STEP1 Generation of four-vectors of final state particles for the corresponding process according to a physical model. Here we used the standard LUND string fragmentation program (version 6.1) to simulate the $\Upsilon(4S)$ decay at rest into $B\overline{B}$ pair and with further rare FCNC decay of one of the B's into a K^* meson and a γ (or $K(K^*)$ and J/ψ). The decay of the second B meson is randomly chosen from Table D.1.

STEP2 Propagation of the generated particles through all parts of the detector. Electromagnetically showering particles are simulated with the EGS 3 (Electron Gamma Simulation) program [55] while hadrons are handled by the GHEISHA 6 (Gamma Hadron Electron Interaction SHower code) program [58] improved by Z. Jakubowski and M. Kobel [59].

STEP3 Reconstruction (production) and analysis of the Monte Carlo sample obtained from STEP2 exactly in the same way as for real data.
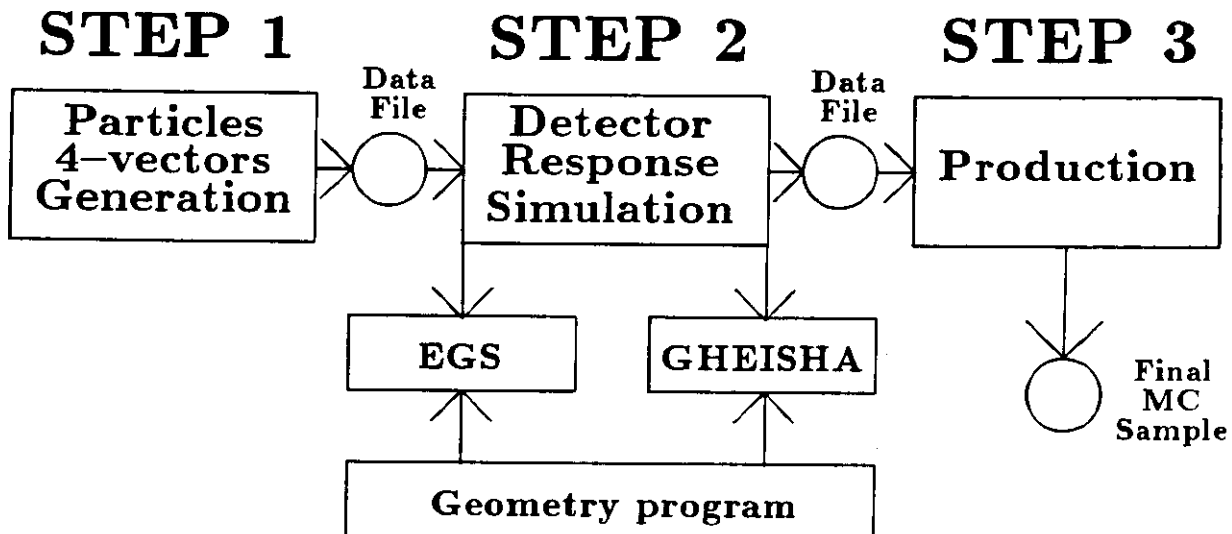
Figure D.1: Organization of the Crystal Ball Monte Carlo programs.

Table D.1: Branching fractions (in %) for the b quark decay modes taken as input to the Monte Carlo.

Decay mode	Branching fraction (%)
$b \rightarrow \bar{\nu}_e e^- c$	11.2
$b \rightarrow \bar{\nu}_\mu \mu^- c$	11.2
$b \rightarrow \bar{\nu}_\tau \tau^- c$	5.0
$b \rightarrow \bar{u}dc$	49.6
$b \rightarrow \bar{u}cd$	8.0
$b \rightarrow \bar{c}sc$	14.0
$b \rightarrow \bar{c}cs$	1.0

The masses of particles and branching fractions of their decays are taken from the Review of Particle Properties of the Particle Data Group [39]. The branching fractions for the decays of the b quark are listed in Table D.1 (we assume here the spectator model of the B meson decays) [45]. The fragmentation of quarks into hadrons is governed by the LUND model. The ratio $N(B^+ B^-)/N(B^\circ \bar{B}^\circ) = 1 : 1$ has been assumed. The time of generation of one Monte Carlo event in the STEP2 was about 3 sec on an IBM 3081K. In the STEP3 extra energy deposited in the crystals by beam-related background was taken into account by adding special background events to the Monte Carlo events. These background events were obtained by triggering on every 10^7th beam crossing with no other condition.

E. Signal parametrizations

We parametrized the shape of the signal expected in the inclusive photon spectrum by a 'bell' function or by a Gaussian function. The values of parameters of the above functions have been obtained by fitting them to the distributions of Monte Carlo samples simulating the relevant decays (after the full selection). We have checked that our results are not sensitive to the choice of the parametrization.

A 'bell' function F_B is defined as:

$$F_B(x) = \frac{C_{norm}}{1 + \exp(\frac{|x - \bar{x}| - \sigma_x/2}{z})},$$

(E.1)

where C_{norm} normalizes the function to unit area and $x = \ln E$ (E is photon energy). It approximately describes the convolution of the Doppler broaded distribution (parameter σ_x) and the energy resolution function (parameter z).

Alternatively we also use a Gaussian function for a signal parametrization:

$$F_G(x) = \frac{1}{\sqrt{2\pi}\sigma_x} e^{-(x-\bar{x})^2/2\sigma_x^2}.$$

(E.2)

Table E.1 contains the parameters of the bell and Gaussian functions used for parametrization of the signal from the exclusive decays $B \to K^*\gamma$, which was expected in the inclusive photon spectrum.

In Table E.2 we present the widths of the Gaussian function (centered at $\cos\alpha = -1$) used in the fits to the distributions of the cosine of the angle α between the photon and the 'opposite' particle.

Parameters of the bell and Gaussian function (in GeV^2) applied in the search for the decays $B \to KJ/\psi$ and $B \to K^*J/\psi$ in the spectrum of the missing mass with respect to the J/ψ are listed in Table E.3.

Table E.1: Parameters (in $\ln E$ (GeV)) of the bell and Gaussian function describing the signal expected in the inclusive photon spectrum for the decays $B \to K^*\gamma$ from Monte Carlo samples.

Mode	Bell function parameters (formula E.1)			Gaussian function parameters (formula E.2)	
	Mean ($\bar{x}$)	Width (σ_x)	Slope (z)	Mean ($\bar{x}$)	Width (σ_x)
$B \to K^*(892)\gamma$	7.843 ± 0.002	0.121 ± 0.005	0.014 ± 0.001	7.842 ± 0.001	0.044 ± 0.001
$B \to K_1(1400)\gamma$	7.802 ± 0.002	0.121 ± 0.007	0.015 ± 0.002	7.801 ± 0.002	0.045 ± 0.001
$B \to K_2(1770)\gamma$	7.756 ± 0.002	0.125 ± 0.003	0.015 ± 0.001	7.756 ± 0.002	0.046 ± 0.001
$B \to K_4^*(2075)\gamma$	7.708 ± 0.002	0.125 ± 0.005	0.013 ± 0.002	7.707 ± 0.002	0.048 ± 0.003

Table E.2: Widths (in cos α) of the Gaussian function describing the shape of the signal expected in the distribution of the cosine of the angle α between photon and the 'opposite' particle from Monte Carlo samples simulating the relevant decays $B \to K^*\gamma$.

Mode	Width
$B \to K^*(892)\gamma$	0.019 ± 0.01
$B \to K_1(1400)\gamma$	0.031 ± 0.04
$B \to K_2(1770)\gamma$	0.035 ± 0.04
$B \to K_4^*(2075)\gamma$	0.041 ± 0.05

Table E.3: Parameters (in GeV^2) of the bell and Gaussian functions describing the expected signal from decay modes $B \to K^{(*)}J/\psi$ in the missing mass spectrum with respect to the J/ψ.

Mode	Bell function parameters (formula E.1)			Gaussian function parameters (formula E.2)	
	Mean ($\bar{x}$)	Width (σ_x)	Slope (z)	Mean ($\bar{x}$)	Width (σ_x)
$B \to KJ/\psi$	0.22 ± 0.03	2.34 ± 0.07	0.17 ± 0.03	0.22 ± 0.03	0.81 ± 0.03
$B \to K^*(892)J/\psi$	0.75 ± 0.03	2.34 ± 0.08	0.19 ± 0.02	0.75 ± 0.03	0.77 ± 0.02
$B \to K_1(1400)J/\psi$	1.95 ± 0.02	1.99 ± 0.08	0.16 ± 0.02	1.95 ± 0.03	0.64 ± 0.02
$B \to K_3^*(1780)J/\psi$	3.13 ± 0.02	1.32 ± 0.09	0.18 ± 0.03	3.13 ± 0.02	0.51 ± 0.02

F.   The Crystal Ball Collaboration

D. Antreasyan[8], H.W. Bartels[4], Ch. Bieler[7], J.K. Bienlein[4], A. Bizzeti[6], E.D. Bloom[10],
K. Brockmüller[4], A. Cartacci[6], M. Cavalli-Sforza[2], R. Clare[10], A. Compagnucci[6], G. Conforto[6],
S. Cooper[10], D. Coyne[2], G. Drews[4], K. Fairfield[10], G. Folger[5], A. Fridman[11], D. Gelphman[10],
G. Glaser[5], G. Godfrey[10], K. Graaf[7], F.H. Heimlich[7], F.H. Heinsius[7], R. Hofstadter[10], J. Irion[8],
Z. Jakubowski[3], K. Karch[11], S. Keh[11], T. Kiel[7], H. Kilian[11], I. Kirkbride[10], M. Kobel[5], W. Koch[4],
A.C. König[9], K. Königsmann[11], S. Krüger[7], G. Landi[6], S. Leffler[10], R. Lekebusch[7], T. Lesiak[3],
A.M. Litke[10], S. Lowe[10], B. Lurz[5], H. Marsiske[4], W. Maschmann[7], P. McBride[8], H. Meyer[4],
B. Muryn[3], W.J. Metzger[9], B. Monteleoni[6], B. Niczyporuk[10], G. Nowak[3], C. Peck[1], C. Pegel[7],
P.G. Pelfer[6], M. Reidenbach[9], M. Scheer[11], P. Schmitt[11], J. Schotanus[9], J. Schütte[5], A. Schwarz[10],
F. Selonke[4], D. Sievers[7], T. Skwarnicki[4], V. Stock[7], K. Strauch[8], U. Strohbusch[7], J. Tompkins[10],
B. van Uitert[10], R.T. Van de Walle[9], A. Voigt[4], U. Volland[5], K. Wachs[4], K. Wacker[10], W. Walk[9],
H. Wegener[5], D. Williams[8]

[1] *California Institute of Technology, Pasadena, CA 91125, USA*
[2] *University of California at Santa Cruz, Santa Cruz, CA 95064, USA*
[3] *Cracow Institute of Nuclear Physics, PL-30055 Cracow, Poland*
[4] *Deutsches Elektronen Synchrotron DESY, D-2000 Hamburg, Germany*
[5] *Universität Erlangen-Nürnberg, D-8520 Erlangen, Germany*
[6] *INFN and University of Firenze, I-50100 Firenze, Italy*
[7] *Universität Hamburg, I. Institut für Experimentalphysik, D-2000 Hamburg, Germany*
[8] *Harvard University, Cambridge, MA 02138, USA*
[9] *University of Nijmegen and NIKHEF NL-6525 ED Nijmegen, The Netherlands*
[10] *Department of Physics, HEPL, and Stanford Linear Accelerator Center, Stanford University, Stanford, CA 94305, USA*
[11] *Universität Würzburg, D-8700 Würzburg, Germany*

Acknowledgements

List of Figures

List of Tables

Bibliography

[1] D. Cocolicchio, G. Costa, G.L. Fogli, A. Masiero, Phys. Rev. **D40** (1989) 1477.

[2] W.S. Hou, R.S. Willey, Phys. Lett. **B202** (1988) 591;
B. Grinstein and M. Wise, Phys. Lett. **B201** (1988) 274.

[3] H.P. Nilles, Phys. Rep. **110** (1984) 1;
S. Bertolini, F. Borzumati, A. Masiero, Phys. Lett **B192** (1987) 437:
A. Masiero, G. Ridolfi, Phys. Lett. **B212** (1988) 171.

[4] T. Lesiak et al., Crystal Ball collaboration, preprint DESY 91-076 (1991); submitted to Z. Phys. **C**.

[5] C. Bebek et al., CLEO collaboration. Phys. Rev. **D36**, (1987) 1289.

[6] S. Okubo. Phys. Lett. **5** (1963) 165;
G. Zweig, CERN Reports TH-401, TH-412 (1964);
J. Izuka, Prog. Theor. Phys. Suppl. **37-38** (1966) 21.

[7] G. Altarelli et al., Nucl. Phys. **B208** (1982) 365.

[8] H. Albrecht et al., ARGUS collaboration. Phys. Lett. **B232** (1989) 554;
K. R. Schubert, preprint IEKP -KA/89-6 (1989); talk at 3 rd International Symposium on Heavy Quark Physics, Ithaca, New York (1989).

[9] M. Bauer. B. Stech and M. Wirbel. Z. Phys. **C29** (1985) 637; **C34** (1987) 103.

[10] S. Glashow, J. Iliopoulos and L. Maiani, Phys. Rev. **D2**, (1970) 1285.

[11] M.A. Shifman, A.I. Vainshtein and V.I. Zakharov, Nucl. Phys. **B120** (1977) 316.
W.A. Bardeen, A.J. Buras and J.-M. Gerard, Nucl. Phys. **B293** (1987) 787.

[12] J.F. Donoghue, E. Golowich and G. Valencia, Phys. Rev. **D33** (1986) 1387.

[13] M. Kobayashi and T. Maskawa. Prog. Theor. Phys. **49** (1973) 652.

[14] L. Wolfenstein, Phys. Rev. Lett. **51** (1984) 1945.

[15] R. Fulton et al., CLEO collaboration, Phys. Rev. Lett. **62** (1989) 2436.

[16] A. de Rujula, H. Georgi, S.L. Glashow, Phys. Rev. **D12**, (1975) 147.

[17] J. Ellis, P.J. Franzini, preprint CERN-TH.4952/88 (1988);*Proceedings of the Courmayeur Workshop* (1987) 341.

[18] N.G. Deshpande and P.Lo.J. Trampetic, Z. Phys. **C40** (1988) 369.

[19] P. Avery et al., CLEO collaboration, Phys. Lett. **183B**, (1987) 429.

[20] M.K. Gaillard, X.Q. Li and S. Rudaz, Phys. Lett. **158B** (1985) 158.

[21] N.Yeh et al., Phys. Rev. **D10** (1974) 3549.

[22] N.G. Deshpande, G. Eilam, Phys. Rev. **D26** (1982) 2463.

[23] I. Inami, C.S. Lim, Progr. Theor. Phys. **65** (1981) 297; E **65** (1981) 1772.

[24] S. Bertolini. in: *Proceedings of the 8 th INFN Eloisatron Workshop on Higgs Particle(s)*, A. Ali (editor), Plenum Press, New York, 1990.

[25] S. Bertolini. F. Borzumati. A. Masiero, Phys. Rev. Lett. **59** (1987) 180.

[26] N.G. Deshpande and P.Lo.J. Trampetic, Phys. Rev. Lett. **59** (1987) 183.

[27] B. Grinstein, R. Springer, M.B. Wise, Phys. Lett. **B202** (1988) 138.

[28] R. Grigjanis, P.O'Donnell, M. Sutherland and H. Navelet, Phys. Lett. **B213** (1989) 355; **B223** (1989) 239; **B224** (1989) 209.

[29] J. Ellis and G. L. Fogli, Phys. Lett. **B232** (1989) 139.

[30] N.G. Deshpande, P.Lo.J. Trampetic, G. Eilam, P. Singer, Phys. Rev. Lett. **59** (1987) 183.

[31] T. Altomari, Phys. Rev. **D37** (1988) 677.

[32] C. A. Dominguez, N. Paver and Riazzudin, Phys. Lett. **B214** (1988) 459.

[33] N.G. Deshpande, P.Lo.J. Trampetic, K. Panose, Phys. Lett. **B214** (1988) 467.

[34] D. Decamp et al., ALEPH Collaboration, Phys. Lett. **B235** (1990) 399;
B. Adeva et al., L3 Collaboration, Phys. Lett. **249B** (1990) 341;
M.Z. Akrawy et al., OPAL Collaboration, Phys. Lett. **240B** (1990) 497;
P. Abreu et al., DELPHI Collaboration, Phys. Lett. **241B** (1990) 435.

[35] G. Beall, M. Bander and A. Soni, Phys. Rev. Lett. **48** (1982) 848.

[36] L. Wolfenstein, Phys. Rev. **D29** (1984) 2130.

[37] P. Alitti et al., UA2 Collaboration, Phys. Lett. **B235**, (1990) 363.

[38] N.G. Deshpande, P.Lo.J. Trampetic, Phys. Rev. **D41** (1990) 986.

[39] Particle Data Group: Review of Particle Properties, Phys. Lett. **B239** (1990) 1.

[40] DESY Storage Ring Group: DORIS,Proc. of the *IX th* International Conference on High Energy Accelerators, Stanford 1974;
The DORIS Storage Ring Group, report DESY 79-08 (1979);
H. Nesemann, K. Wille IEEE Trans. of Nucl. Sci. **NS-30**, 1988. DESY Internal Report DESY-M-83-09.

[41] A.A. Sokolov and I.M. Ternov, Sov. Phys. Dokl. **8** (1964) 1203.

[42] M. Oreglia et al., Phys. Rev. **D25** (1985) 2259;
D.A. Williams et al., Crystal Ball Collaboration, Phys. Rev. **D38** (1988) 1365;
K. Wachs et al., Crystal Ball Collaboration, Z. Phys. **C42** (1989) 33.

[43] H. J. Trost, Crystal Ball Internal Report (1983);
Z. Jakubowski et al., Crystal Ball Collaboration. Z. Phys. C40 (1988) 49; Ph.D. thesis, DESY F31-90-01 (1990).

[44] G.C. Fox, S. Wolfram, Phys. Rev. Lett. **41.** (1978) 1581.

[45] T. Sjøstrand, Lund report LU TP 85-10, October 1985;
H.-W. Bengtsson and T. Sjøstrand, Comp. Phys. Comm. **46** (1987) 43.

[46] L. Lyons: Statistics for nuclear and particle physicists, Cambridge University Press 1986.

[47] S. Baker, and R.D. Cousins, N.I.M. **221** (1984) 437.

[48] F. James, M. Roos, Computer Physics Communication **10** (1975) 343.

[49] P. Avery et al., CLEO colaboration, Phys. Lett. **B223** (1988) 470.

[50] H. Albrecht et al.. ARGUS Collaboration, Phys. Lett. **B229** (1989) 304.

[51] P. Mattig, preprint CERN-EP/90-71 (1990);
T. Nakada, preprint CERN-90-02 (1990);
H. Kolanoski, preprint DESY 90-124 (1990);
K. Lingel et al., preprint CLNS 91-1043 (1991);
E.D. Bloom, *La Thuile 1988. Proceedings, Supernova 1987A, one year later* (1987).

[52] H. Schröder, Talk at XXIV International Conference on High Energy Physics, (Munich 1988).

[53] D. Gelphman et.al., Crystal Ball Collaboration, Phys. Rev. **D32** (1985) 2893;
D. Gelphman, Ph. D. Thesis, Stanford University, SLAC-286 (1985).

[54] F.A. Berends and R. Kleiss, Nucl. Phys. **B228** (1983) 537; Nucl. Phys. **B186** (1981) 22.

[55] R. Ford and W. Nelson, report SLAC-210 (1978).

[56] B. Naroska, report DESY-86-113 (1986).

[57] J. Schütte, Ph.D. Thesis, University of Erlangen-Nürnberg (1989) unpublished.

[58] H. Fesefeldt, Aachen report PITHA 85/02.

[59] Z. Jakubowski, M. Kobel, Nucl. Instr. Meth. **A297** 60 (1990); report DESY 89-165 (1989).